

Direct measurements of meltwater runoff on the Greenland ice sheet surface

Laurence C. Smith^{a,1,2}, Kang Yang^{b,1}, Lincoln H Pitcher^a, Brandon T. Overstreet^c, Vena W. Chu^d, Åsa K. Rennermalm^e, Jonathan C. Ryan^{a,f}, Matthew G. Cooper^a, Colin J. Gleason^g, Marco Tedesco^h, Jeyavinoth Jeyaratnamⁱ, Dirk van As^j, Michiel R. van den Broeke^k, Willem Jan van de Berg^k, Brice Noël^k, Peter L. Langen^l, Richard I. Cullather^{m,n}, Bin Zhaoⁿ, Michael J. Willis^o, Alun Hubbard^{p,q}, Jason E. Box^j, Brittany A. Jenner^r, and Alberto E. Behar^{s,3}

^aDepartment of Geography, University of California, Los Angeles, CA 90095; ^bSchool of Geographical and Oceanographic Sciences, Nanjing University, 210093 Nanjing, China; ^cDepartment of Geography, University of Wyoming, Laramie, WY 82071; ^dDepartment of Geography, University of California, Santa Barbara, CA 93106; ^eDepartment of Geography, Rutgers, The State University of New Jersey, Piscataway, NJ 08854; ^fInstitute at Brown for Environment and Society, Brown University, Providence, RI 02912; ^gDepartment of Civil and Environmental Engineering, University of Massachusetts, Amherst, MA 01003; ^hLamont-Doherty Earth Observatory of Columbia University, Palisades, NY 10964; ⁱThe City College of New York, New York, NY 10031; ^jGeological Survey of Denmark and Greenland (GEUS), 1350 Copenhagen, Denmark; ^kInstitute for Marine and Atmospheric Research, Utrecht University, Utrecht 3508, The Netherlands; ^lClimate and Arctic Research, Danish Meteorological Institute, DK-2100 Copenhagen O, Denmark; ^mEarth System Science Interdisciplinary Center, University of Maryland at College Park, College Park, MD 20740; ⁿNASA Goddard Space Flight Center, Greenbelt, MD 20771; ^oCooperative Institute for Research in Environmental Sciences (CIRES), University of Colorado, Boulder, CO 80309; ^pCentre for Arctic Gas Hydrate, Environment, and Climate, University of Tromsø, N-9037 Tromsø, Norway; ^qCentre for Glaciology, Institute of Geography and Earth Sciences, Aberystwyth University, Aberystwyth SY23 3DB, United Kingdom; ^rSonTek, San Diego, CA 92107; and ^sNASA Jet Propulsion Laboratory, Pasadena, CA 91109

Edited by Anny Cazenave, Centre National d'Etudes Spatiales (CNES), Toulouse, France, and approved October 10, 2017 (received for review May 11, 2017)

Meltwater runoff from the Greenland ice sheet surface influences surface mass balance (SMB), ice dynamics, and global sea level rise, but is estimated with climate models and thus difficult to validate. We present a way to measure ice surface runoff directly, from hourly in situ supraglacial river discharge measurements and simultaneous high-resolution satellite/drone remote sensing of upstream fluvial catchment area. A first 72-h trial for a 63.1-km² moulin-terminating internally drained catchment (IDC) on Greenland's midelevation (1,207–1,381 m above sea level) ablation zone is compared with melt and runoff simulations from HIRHAM5, MAR3.6, RACMO2.3, MERRA-2, and SEB climate/SMB models. Current models cannot reproduce peak discharges or timing of runoff entering moulins but are improved using synthetic unit hydrograph (SUH) theory. Retroactive SUH applications to two older field studies reproduce their findings, signifying that remotely sensed IDC area, shape, and supraglacial river length are useful for predicting delays in peak runoff delivery to moulins. Applying SUH to HIRHAM5, MAR3.6, and RACMO2.3 gridded melt products for 799 surrounding IDCs suggests their terminal moulins receive lower peak discharges, less diurnal variability, and asynchronous runoff timing relative to climate/SMB model output alone. Conversely, large IDCs produce high moulin discharges, even at high elevations where melt rates are low. During this particular field experiment, models overestimated runoff by +21 to +58%, linked to overestimated surface ablation and possible meltwater retention in bare, porous, low-density ice. Direct measurements of ice surface runoff will improve climate/SMB models, and incorporating remotely sensed IDCs will aid coupling of SMB with ice dynamics and subglacial systems.

ice sheet meltwater runoff | surface mass balance | climate models | fluvial catchment | surface water hydrology

The production and transport of meltwater (runoff) is an important hydrological process operating on the surface of the Greenland ice sheet (GrIS). Total GrIS mass loss from runoff and solid ice dynamics (glacier calving) now exceeds ~260 Gt/y, contributing >0.7 mm annually to global mean sea level rise (1–3). Since 2009, approximately two-thirds of this total mass loss has been driven by negative ice sheet surface mass balance (SMB) and associated runoff increases, as calculated from climate/SMB models (3, 4). This runoff passes through supraglacial stream/river networks entering moulins (englacial conduits) and crevasses that connect to the bed (5–9), temporarily influencing basal water pressures and/or ice motion (10–13) and forming a dynamic subglacial drainage system that expels water toward the ice edge and global ocean. The new dominance of runoff as a driver of GrIS

total mass loss will likely persist into the future, because of further increases in surface melting (14), reduced meltwater storage in firm due to formation of near-surface ice layers (15), and possibly a waning importance of dynamical mass losses as ice sheets retreat from their marine-terminating margins (16). Therefore, the hydrological process of ice surface runoff warrants study, both for basic scientific understanding and to improve representation and/or parameterization of runoff processes in climate/SMB models.

A key uncertainty in climate/SMB projections of future GrIS runoff contributions to global sea level is that estimating runoff requires partitioning of SMB among some poorly constrained processes, with the modeled “runoff” (R) simply an error-sensitive residual of the sum of modeled meltwater production (M), rainfall and condensation, minus modeled retention, refreezing,

Significance

Meltwater runoff is an important hydrological process operating on the Greenland ice sheet surface that is rarely studied directly. By combining satellite and drone remote sensing with continuous field measurements of discharge in a large supraglacial river, we obtained 72 h of runoff observations suitable for comparison with climate model predictions. The field observations quantify how a large, fluvial supraglacial catchment attenuates the magnitude and timing of runoff delivered to its terminal moulin and hence the bed. The data are used to calibrate classical fluvial hydrology equations to improve meltwater runoff models and to demonstrate that broad-scale surface water drainage patterns that form on the ice surface powerfully alter the timing, magnitude, and locations of meltwater penetrating into the ice sheet.

Author contributions: L.C.S., K.Y., L.H.P., B.T.O., V.W.C., and Å.K.R. designed research; L.C.S., K.Y., L.H.P., B.T.O., V.W.C., Å.K.R., J.C.R., M.G.C., C.J.G., M.T., J.J., D.v.A., M.R.v.d.B., W.J.v.d.B., B.N., P.L.L., R.I.C., B.Z., and M.J.W. performed research; A.H., J.E.B., and B.A.J. contributed new analytic tools; J.C.R. and A.E.B. designed instrumentation; L.C.S., K.Y., L.H.P., J.C.R., and M.G.C. analyzed data; and L.C.S. and K.Y. wrote the paper.

The authors declare no conflict of interest.

This article is a PNAS Direct Submission.

This open access article is distributed under Creative Commons Attribution-NonCommercial-NoDerivatives License 4.0 (CC BY-NC-ND).

¹L.C.S. and K.Y. contributed equally to this work.

²To whom correspondence should be addressed. Email: lsmith@geog.ucla.edu.

³Deceased January 9, 2015.

This article contains supporting information online at www.pnas.org/lookup/suppl/doi:10.1073/pnas.1707743114/-DCSupplemental.

and sublimation in snow and firn. Representation of these various elements varies by model (*SI Appendix, sections 6.1–6.5*), but in all cases R is an error-sensitive residual that is not independently validated with in situ field measurements collected on the ice surface. Previous efforts to validate R have used proglacial river discharge (outflow) emerging from the ice edge (7, 17–20), but outflow fundamentally differs from R because it incorporates complex en- and subglacial processes that can delay, remove, or add water, including cavity storage/release, reservoir constrictions, conduit pressurization, subdaily variations in hydraulic potential gradient, basal melting, and subglacial aquifers (5, 10, 17, 21–23). Furthermore, basin delineations for proglacial river outlets have high uncertainty (7, 17, 24), are keenly sensitive to user choice of a hydraulic potential parameter [i.e., the k -value (25, 26)], and are vulnerable to water piracy between adjacent basins (27, 28). Proglacial river discharge measurements can suffer large uncertainty due to heavy sediment loads, braided channels, and mobile beds (29). In short, proglacial outflow does not confidently reflect the timing of SMB and runoff processes operating on the GrIS surface, especially at diurnal time scales.

At the present time, climate/SMB models contain little or no provision for retention and/or refreezing of runoff in bare ice (i.e., either on or below the ice surface), or for flow routing (lateral transport) of runoff over the ice surface to moulins. Instead, residual M converts instantly to R and is assumed to depart the ice surface. This is acceptable for estimating net SMB but not for estimating the timing and volume of runoff delivered to moulins, the dominant pathway linking supraglacial with subglacial hydrological systems (7, 21, 24). This, in turn, clouds understanding of the interplay between SMB and ice dynamics, especially at short time scales. Moulins inject surface runoff into a transient, subglacial hydrological system exerting primary control on diurnal to multi-day changes in ice sheet basal motion and water pressure (11, 12, 30–33). Subdaily delays or lags between the timing of surface melt and basal water pressures are often used to infer capacity of the subglacial drainage system, yet supraglacial routing delays receive little or simplified treatment (9, 10, 31, 34).

Finally, solar radiation supplies most energy for melting ice on the GrIS margins and bare-ice ablation zone, followed by the turbulent flux of sensible heat (35, 36). As a result, temporal scales governing energy and mass exchange between the atmosphere and ice surface range from seconds (for turbulent eddies) to daily and monthly for net radiative surface energy balance. Because solar radiation dominates melting, it is imperative to resolve the effect of diurnal cycles in the surface energy balance on surface runoff. The diurnal time scale is especially important for runoff generation in the midelevation ablation zone, where daytime melting is interrupted by nighttime freezing (37), causing heat loss from the ice surface and potential refreezing of meltwater. Diurnal variations in runoff also influence ice dynamics, because ice motion accelerations are driven by variability in meltwater input (10, 12). Meltwater alternatively flows from subglacial channels into the distributed basal system during intervals of high supply/high pressure, and from the distributed system into channels during intervals of low supply/low pressure (33, 38, 39). This diurnal pressurization of the distributed system drives diurnal variations in ice velocity. Numerical modeling shows increases in diurnal ice motion and a slight increase in annual mean velocity when diurnal variations in surface runoff input are considered (40).

In sum, climate/SMB models are essential tools for simulating SMB runoff inputs to subglacial systems and to the global ocean (41, 42), but they currently lack validating field measurements of runoff timing and quantity, especially over diurnal time scales. To address these challenges, we present a field-based approach to measure R directly on the ice sheet surface—before en- and subglacial interferences—at the scale of a supraglacial internally drained catchment (IDC). IDCs are defined by fluvial supraglacial stream/river networks, which dominate surface drainage patterns on the

southwestern GrIS (43). They have areas of order $\sim 10^1$ – 10^2 km², a geographic scale comparable to the grid cells of most regional climate/SMB models. The field procedure is demonstrated for a representative IDC having an area of 63.1 km² (our best estimate of catchment area, with upper and lower uncertainty bounds of 69.1 and 51.4 km², respectively), hereafter called the Rio Behar catchment in honor of the late Dr. Alberto E. Behar (Fig. 1). Spanning an elevation range of 1,207–1,381 m, Rio Behar catchment is located just below the long-term equilibrium line [$\sim 1,500$ m above sea level (a.s.l.) in this area (34)], experiences seasonal melting from June through August of each year, and is centrally located in one of the highest runoff-producing regions of the GrIS (3, 14). Our field trial was conducted in late July 2015, near the end of the peak runoff season when the region's supraglacial stream/river networks are fully developed, yet before the onset of reduced melting in August (Fig. 2).

Conceptually, our approach is simple, requiring only hourly measurements of discharge in an IDC main-stem supraglacial river (i.e., to measure the volume of runoff physically departing the source catchment) and high-resolution mapping of the IDC's contributing upstream catchment area. Note that “runoff” has units of depth per model time step in gridded climate model output ($L T^{-1}$, typically $\text{mm} \cdot \text{d}^{-1}$ or $\text{mm} \cdot \text{h}^{-1}$) but units of discharge when obtained from in situ measurements ($L^3 T^{-1}$, typically $\text{m}^3 \cdot \text{s}^{-1}$). Remotely sensed catchment area (L^2 , typically km^2) is required for conversion between the two units of runoff.

We measured discharge hourly in the main-stem supraglacial river of Rio Behar catchment for 72 h from 20 to 23 July 2015 by deploying an RTK GPS SonTek RiverSurveyor Acoustic Doppler Current Profiler (ADCP) from a bank-operated cableway suspended across the river immediately upstream of its descent to the catchment's terminal moulin (*SI Appendix, Fig. 1*). During the same period, we obtained high-resolution images from the DigitalGlobe WorldView-1 and WorldView-2 satellites (resolution 0.5 m panchromatic, 2.0 m multispectral) and from a custom-made fixed-wing drone [unmanned aerial vehicle (UAV); visible band, resolution 0.3 m]. These acquired images were used to map Rio Behar catchment boundaries, surface drainage pattern, and snow cover. Topographic divides of the catchment were delineated from a high-resolution digital elevation model (DEM) of the ice surface, derived stereo-photogrammetrically from a WorldView-1 image pair acquired 18 July 2015. The long-term stability of this catchment was established from older WorldView image pairs beginning in 2008 (Fig. 1). The 2015 topographic boundary was later manually adjusted for small areas lost (2.7 km²) or gained (0.8 km²) due to stream piracy (breaching) across divides, and for small internal subareas draining to minor internal moulins (1.6 km²). Intersection of this corrected catchment area (63.1 km²) and its maximum plausible extent (69.1 km², identified by mapping outer channel heads; Fig. 1) and minimum plausible extent (51.4 km², identified by mapping inner channel heads and removal of 4.1 km² of crevasse fields; see Fig. 1 and *SI Appendix, section 3.2*) with gridded outputs from the HIRHAM5, MAR3.6, RACMO2.3, MERRA-2, and Point SEB climate/SMB models enables a first direct comparison between modeled and measured on-ice R for the Rio Behar catchment (Figs. 3 and 7A).

Results

Comparison of our hourly discharge measurements (*SI Appendix, Table 1*) with hourly climate/SMB model outputs of catchment R quantifies the attenuation and delay of observed R delivered to the Rio Behar catchment terminal moulin (Fig. 3). Because evacuation of runoff requires physical passage through the IDC's fluvial drainage pattern, some duration of time must pass between the timing of peak R generated across the IDC and the timing of peak R (i.e., peak discharge) received by the moulin. This duration is called “time-to-peak” (t_p , in hours) in traditional terrestrial hydrograph analysis (44, 45). In general,

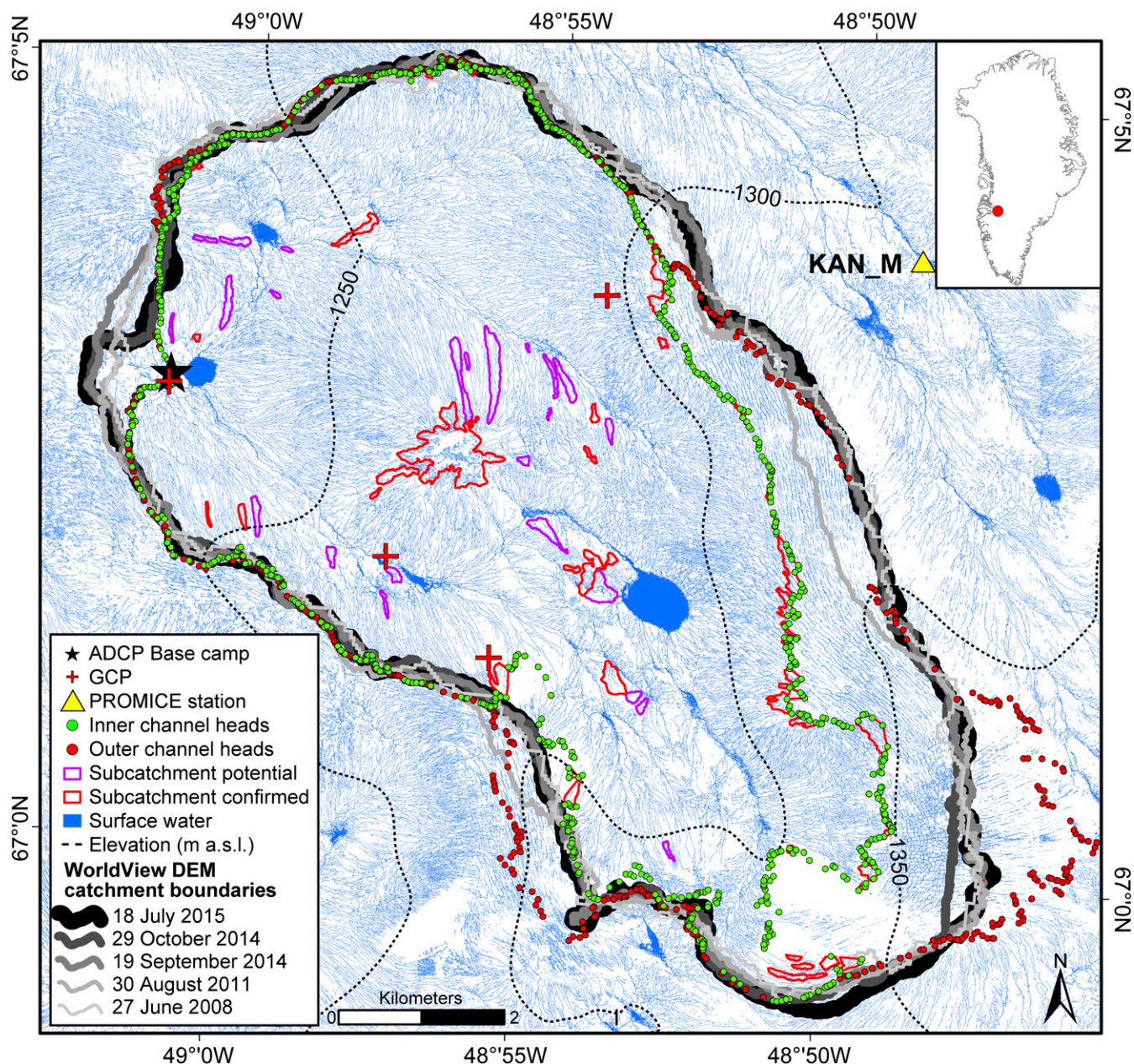


Fig. 1. WorldView-1/2 satellite-derived map of Rio Behar catchment, a moderately sized (63.1 km^2) internally drained catchment (IDC) centrally located in a melt-intensive area of the GrIS (*Inset*). From 20 to 23 July 2015, we collected 72 h of continuous in situ ADCP discharge measurements in the main-stem supraglacial river (Rio Behar) at our base camp (black star; 67.049346N , 49.025809W), $\sim 300 \text{ m}$ upstream of the catchment's terminal moulin. Measurements of ice surface ablation were collected at base camp and by the PROMICE KAN_M automated weather station. Four GPS-surveyed red tarpaulins visible in satellite and drone imagery were used as ground control points (GCP) to aid image geolocation and georectification. Eight years of topographic Rio Behar catchment boundaries, delineated from WorldView satellite stereo-photogrammetric DEMs (multishaded gray lines), establish overall catchment stability from 2008 to 2015. The 18 July 2015 DEM boundary, adjusted for small areas of stream piracy, was used for calculations presented in this study (thick black line; 63.1 km^2). Manually identified stream channel heads (headwater channel incision points) mapped in the 18 July 2015 satellite image constrain minimum (green circles, inner) and maximum (red circles, outer) plausible catchment boundaries, respectively. The minimum boundary eliminates crevasse fields in the southeast catchment headwater area. Polygons bound small confirmed (red polygons) and potential (purple polygons) internally drained subareas (i.e., internal moulins) not draining to the large terminal moulin. Four small, nondraining supraglacial lakes were fully integrated into the stream/river network with no impoundment of flow. This map was created in part using DigitalGlobe, Inc., satellite imagery.

time-to-peak delays will increase for catchments having larger and/or more elongate areas and lower stream densities, with soil porosity, topographic slope, and land cover being contributing factors (45). For a given uniform depth of R generated across the catchment, larger catchments produce greater total discharge and peak discharge (Q_{pk}) than do smaller catchments, due to their larger source areas. Applied to southwest Greenland, where most

IDCs have areas of tens of square kilometers (43), these fluvial catchment processes are thus intrinsic to the scale of a climate/SMB model grid cell.

To demonstrate how influential fluvial supraglacial catchments are to the timing (t_p) and peak discharge (Q_{pk}) of GrIS meltwater runoff delivery to moulins, we use our Rio Behar discharge measurements to calibrate a simple lumped (catchment-scale)

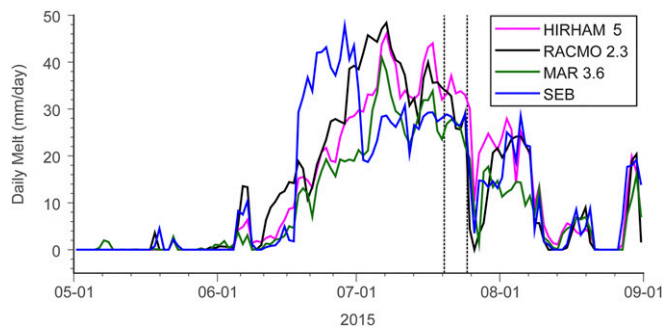


Fig. 2. The 20–23 July 2015 field experiment (dashed lines) was timed for late July near the end of the peak runoff season, when Rio Behar catchment was bare ice, its seasonal surface drainage pattern was fully developed, and before the onset of cooler temperatures and reduced melting in August. Colored lines show daily melt rates (M) from the HIRHAM5, RACMO2.3, MAR3.6, and Point SEB climate/SMB models; melt rate is not supplied by MERRA-2.

morphometric routing model for use on the ablating ice surface, the synthetic unit hydrograph (SUH; *SI Appendix, Methods 4*). Three advantages of the SUH routing model are that it isolates the impact of basic IDC properties (area, shape, and stream length) on t_p and Q_{pk} delivered to the catchment outlet (here, the terminal moulin), which can all be obtained with remote sensing; it does not require use of DEMs [which are acutely sensitive to choice of a depression-filling threshold and do not always reflect true surface drainage patterns (46)]; and it is designed to be transferable to ungauged catchments.

Extension of our field-calibrated SUH to a broad-scale (13,563 km²), remotely sensed map of 799 surrounding IDCs (43) quantifies temporal and spatial heterogeneities in runoff delivery to terminal moulin due solely to differences in IDC areas, shapes, and river lengths (Fig. 4). For a theoretical unit runoff depth

of 1 cm (i.e., a 1-cm-deep layer of water assumed to materialize uniformly across the ice sheet surface in 1 h), catchment-induced time-to-peak delays would range from as low as 0.4 h to as high as 9.5 h, due solely to varying IDC areas, shapes, and river lengths (Fig. 4A). Peak discharges entering moulin would range from as low as 0.7 m³ · s⁻¹ to as high as 53.0 m³ · s⁻¹ (Fig. 4B), again due solely to these basic fluvial catchment properties that are not currently represented in climate/SMB models.

A more realistic scenario, using climate/SMB model outputs of melt production M and a Gamma function to synthesize each IDC's unique SUH (47) (*SI Appendix, Methods 5*), yields similarly heterogeneous spatial patterns not present in gridded climate model output (Fig. 5 and *SI Appendix, Fig. 11*). These heterogeneities include large discharges (>20 m³ · s⁻¹) entering moulin at high elevations on the ice sheet (>1,500 m a.s.l.) despite low melt rates there, due to the presence of large IDCs (43, 48). Importantly, peak moulin discharges are significantly reduced if climate/SMB model output is subjected to unit hydrograph theory (Fig. 5C), rather than the practice of instantaneously aggregating model output within each IDC (33, 49) (Fig. 5B). The opposite is true at night, when modeled melt and instantaneous area-aggregated runoff shut down but SUH-routed runoff is high (*SI Appendix, Fig. 11*). Averaging across all 799 IDCs (including many small catchments) reduces Q_{pk} by 13.5 ± 10.0% if climate/SMB model output is subjected to SUH routing (Fig. 6). Diurnal variability in Q_{pk} is reduced by 15.1 ± 12.5%, and the mean timing delay between peak melt production and peak moulin discharge lengthens by 2.9 ± 2.8 h. For the larger IDCs (>30 km², $n = 122$), for which routing delays are greatest, these averages increase to 30.4 ± 9.1%, 37.0 ± 12.0%, and 5.1 ± 4.6 h, respectively.

Although these numbers should be viewed cautiously because our SUH model depends, in part, on parameters calibrated only at the Rio Behar catchment, a successful retroactive application of SUH to the IDCs of two older field studies (8, 32) is encouraging (*SI Appendix, section 5.3*). Depending on choice of input climate/SMB model, SUH-estimated peak runoff times for a 1.1-km²

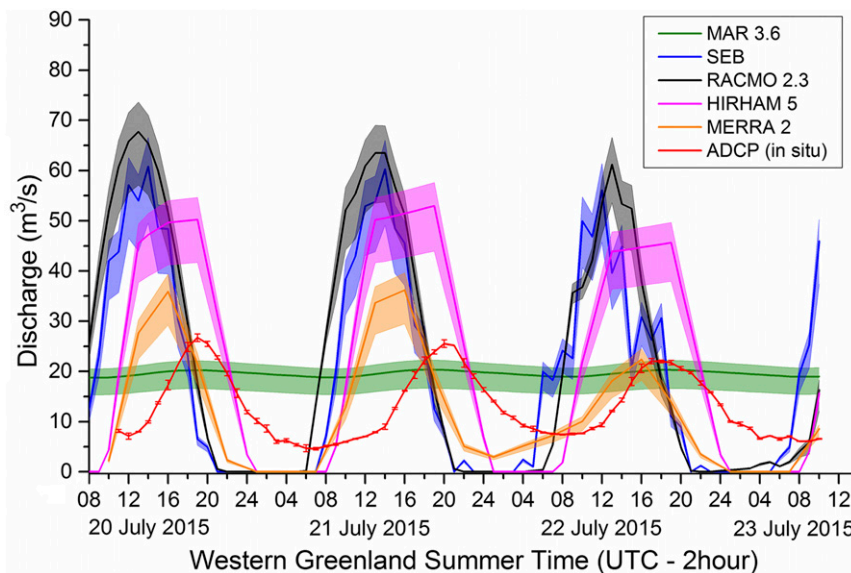


Fig. 3. Hourly supraglacial runoff R from the Rio Behar catchment obtained from in situ ADCP discharge measurements (red) and as estimated by five climate/SMB models (color-shaded envelopes) during the 20–23 July 2015 field experiment. Observed runoff is attenuated and delayed relative to modeled runoff due to nonrepresentation of fluvial transport (routing) in current models. An exception is MAR3.6 (green), which uses a simple delay-to-ice-edge assumption, thus greatly smoothing the diurnal runoff signal. Units of R in climate/SMB models (mm · h⁻¹) are converted to discharge (m³ · s⁻¹) by multiplication with remotely sensed catchment area (Fig. 1), enabling direct comparison with ADCP measurements. The uncertainty bounds shown for modeled R thus reflect Rio Behar catchment area uncertainty, with centerlines denoting the optimal catchment area estimate of 63.1 km² and upper and lower uncertainty reflecting the maximum and minimum plausible catchment area estimates of 69.1 and 51.4 km², respectively. Error bars for in situ data are SDs calculated from multiple ADCP profiles collected within each measurement hour. Local time for Rio Behar catchment is Coordinated Universal Time (UTC) minus 2 h.

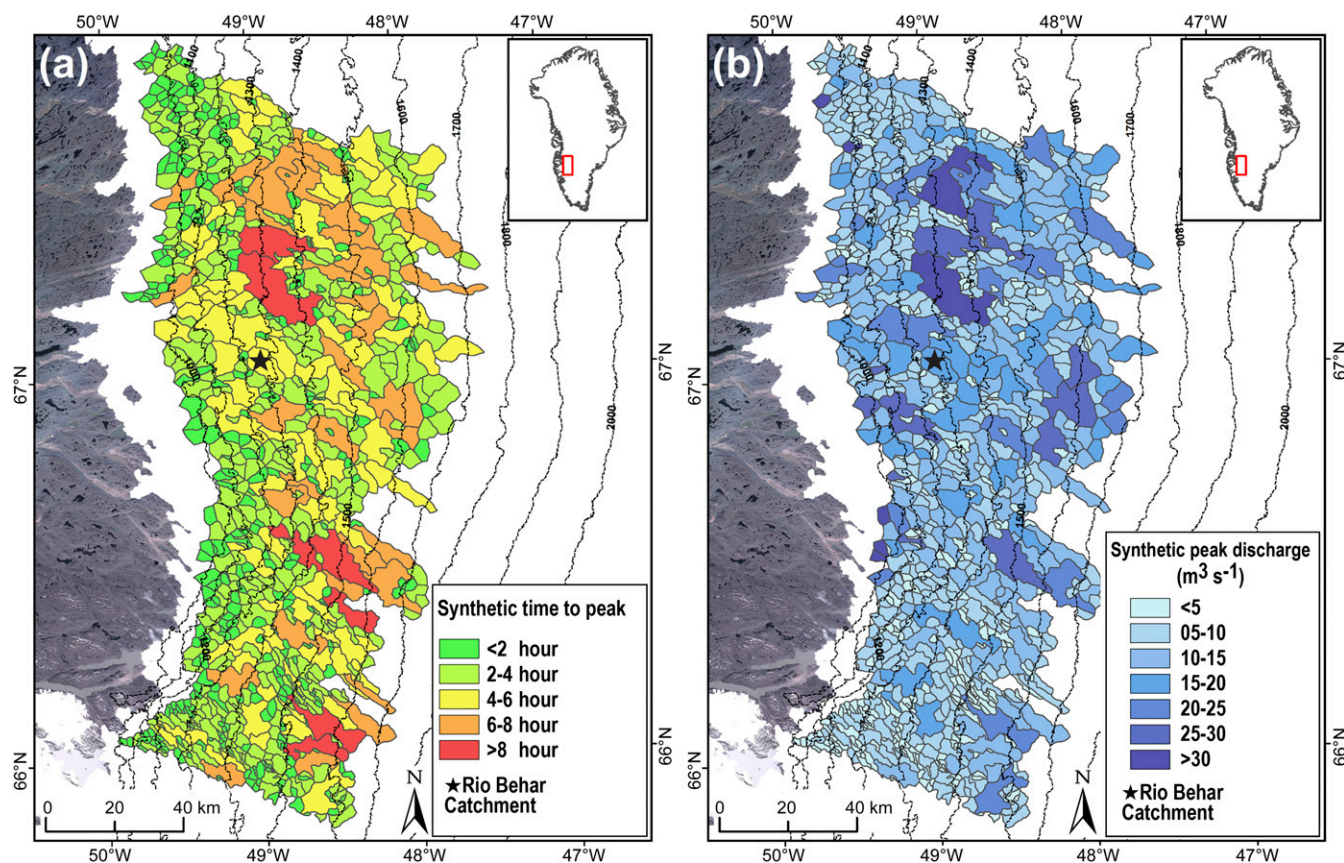


Fig. 4. Application of our field-calibrated Synthetic Unit Hydrograph (SUH) routing model to 799 remotely sensed IDCs on the southwest GrIS [gray borders; mapped previously from a 19 August 2013 panchromatic Landsat-8 image (43)] illustrate how fluvial, supraglacial IDCs impart spatially heterogeneous modifications to meltwater runoff delivered to terminal moulin and hence the bed. Each IDC contains a remotely sensed supraglacial river (not shown for visual clarity) terminating in a major, catchment-terminating moulin. These theoretical SUH maps assume a spatially uniform, 1-cm-deep layer of meltwater released over a duration of 1 h and isolate the influence of remotely sensed IDC area, shape, and river length on (A) time-to-peak delays of peak runoff arrival at each catchment's terminal moulin (t_p , in hours) and (B) magnitude of peak discharge received at each catchment's terminal moulin (Q_{pk} , $\text{m}^3 \cdot \text{s}^{-1}$). More realistic maps, forced by climate/SMB models, are shown in Fig. 5 and *SI Appendix*, Fig. 11.

IDC nearly 300 km distant from the Rio Behar catchment range from 16:00 to 20:00 (local Greenland time), comparable to 16:30–17:00 observed in field observations acquired in August 2009 (8, 32) (*SI Appendix*, Table 4). For an 18.2-km² IDC ~14 km distant from Rio Behar, SUH-estimated peak runoff times range from 17:00 to 22:00, comparable to field measurements of 18:00–20:00 acquired in late June/early July 2011 (32). Such independent reproducibility of runoff timing delays measured at other times and sites on the ice sheet suggest utility of SUH elsewhere on the southwest GrIS ablation zone. However, collection of additional supraglacial discharge datasets, especially from large IDCs and colder regions, is needed for further calibration and validation of the SUH approach.

With regard to the absolute magnitudes of measured versus modeled runoff, comparison of our cumulative ADCP discharge measurements with cumulative modeled R over our 72-h field experiment found that climate/SMB models overestimated R by +21 to +58% for this particular location and time on the ice sheet (for a five-model average, assuming lower and upper constraints on watershed extent, respectively). Taken separately, four of five models overestimated R (Fig. 7A). Similarly, four of four models (for which melt M is available) overestimated ice surface lowering (ablation), if their outputs of M are compared with in situ ice surface-lowering measurements collected from 15 ablation stakes at our base camp and sonic surface-lowering data from the nearby PROMICE KAN_M automated weather station (AWS) (Fig. 7B and *SI Appendix*, Table 5). This conclusion holds regardless

of whether the density of solid ice ($0.918 \text{ g} \cdot \text{cm}^{-3}$) is used to convert M to units of ice thickness equivalent, or a lower, near-surface ice density ($0.688 \text{ g} \cdot \text{cm}^{-3}$) averaged from 10 shallow cores drilled at our base camp (50). Point-based ablation measurements have known limitations (51), but both field datasets display less ice surface lowering than modeled M (Fig. 7B), similarly to how the models overestimate R (Fig. 7A).

One interpretation of Fig. 7 is that the models overestimated M , and hence R . However, our comparison of modeled versus in situ AWS surface energy balance (*SI Appendix*, section 6.8) reveals that modeled energy balance components closely matched in situ AWS measurements. In general, RACMO2.3 albedo, radiation, and turbulent fluxes track AWS observations too well to advance model overestimation of surface energy receipt as the leading explanation for model overestimations of ice ablation and R (*SI Appendix*, Fig. 9). For example, the radiative effects of clouds (52) may have contributed slightly to model overestimation of R during the third day of the field experiment, but not the first 2 d when the sky was clear (*SI Appendix*, Fig. 9). Importantly, the Point SEB model is driven purely by AWS measurements, yet similarly overestimates observed surface ablation and R like the other, reanalysis-driven models (Fig. 7).

All of this suggests some meltwater loss or retention process that is external to the “skin” surface energy balance allocated to the top of the ice surface by most models. We hypothesize that subsurface melting (53) and subsequent retention and/or refreezing of meltwater in porous, low-density bare ice [called “weathering crust” (6, 50, 54)] may contribute to or explain the

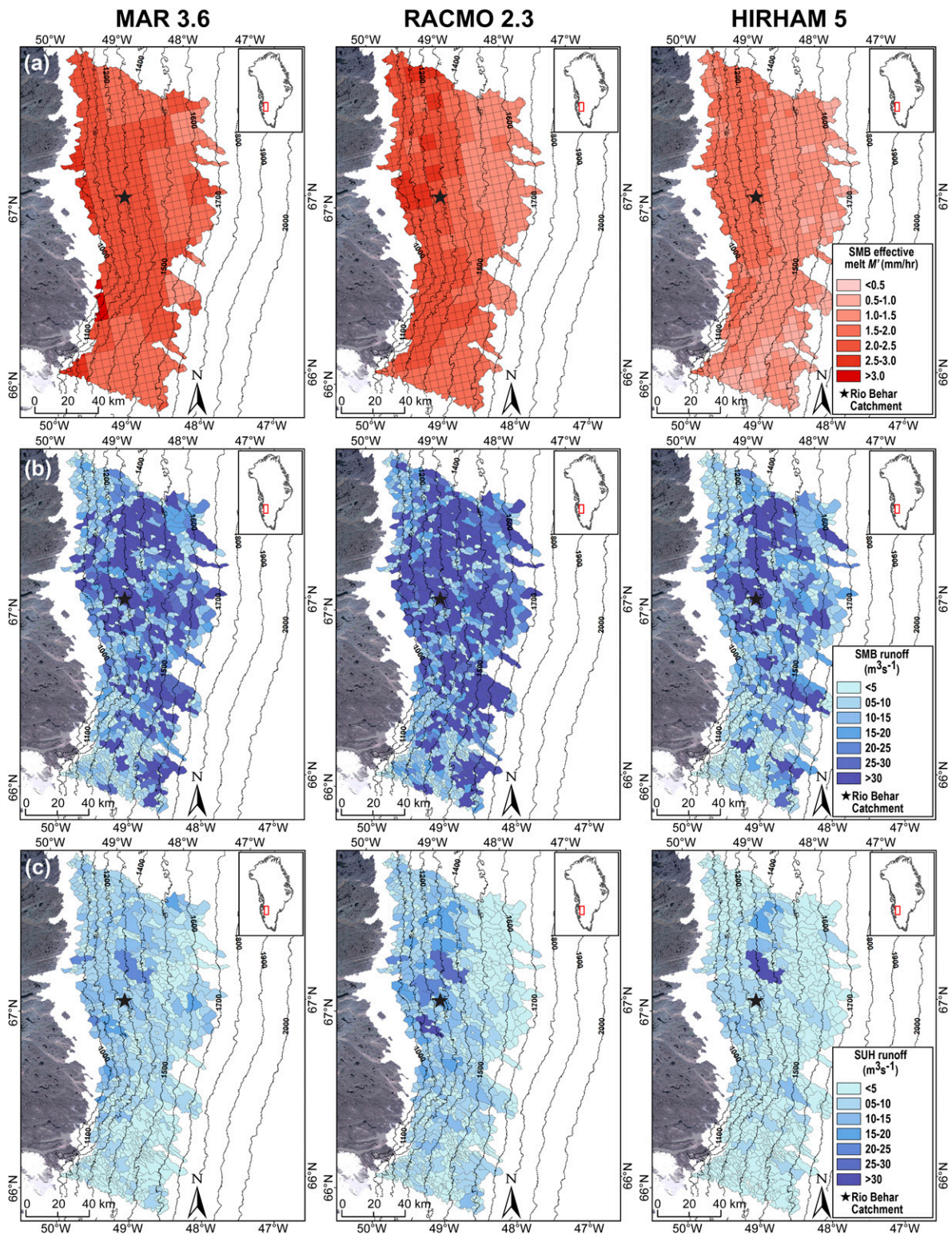


Fig. 5. Supraglacial IDCs modify the timing and magnitude of runoff delivered to terminal moulin, as demonstrated here at 1400 local western Greenland time on 21 July 2015 using (A) MAR3.6, RACMO2.3, and HIRHAM5 climate/SMB model outputs of corrected meltwater production (M' ; see *SI Appendix, section 4.3*) to estimate (B) instantaneous area-integrated runoff and (C) more realistic, SUH-routed runoff. MERRA-2 is not shown because it does supply M . Point SEB is not shown because its output is not gridded. The boundaries of 799 IDCs (gray borders) were mapped previously from a 19 August 2013 panchromatic Landsat-8 image (43). Each IDC contains a remotely sensed, moulin-terminating supraglacial river (not shown for visual clarity). Climate/SMB model output M' has units of water depth equivalent ($\text{mm} \cdot \text{h}^{-1}$), which converts to runoff in discharge units ($\text{m}^3 \cdot \text{s}^{-1}$) following multiplication with intersected IDC catchment boundaries (B and C). The black star at $\sim 67^\circ\text{N}$, 49°W denotes the Rio Behar IDC. In both B and C large IDCs enable large moulin discharges above 1,500 m a.s.l. elevation, despite lower overall melt rates. SUH routing (C) yields lower peak moulin discharges at this time of day than instantaneous area-integrated runoff (B), because SUH requires more time for runoff to travel through fluvial supraglacial stream/river networks. A companion nighttime version of this figure 10 h later (00:00 on 22 July; see *SI Appendix, Fig. 11*) shows the opposite effect, with shutdowns in A and B but high moulin discharges in C.

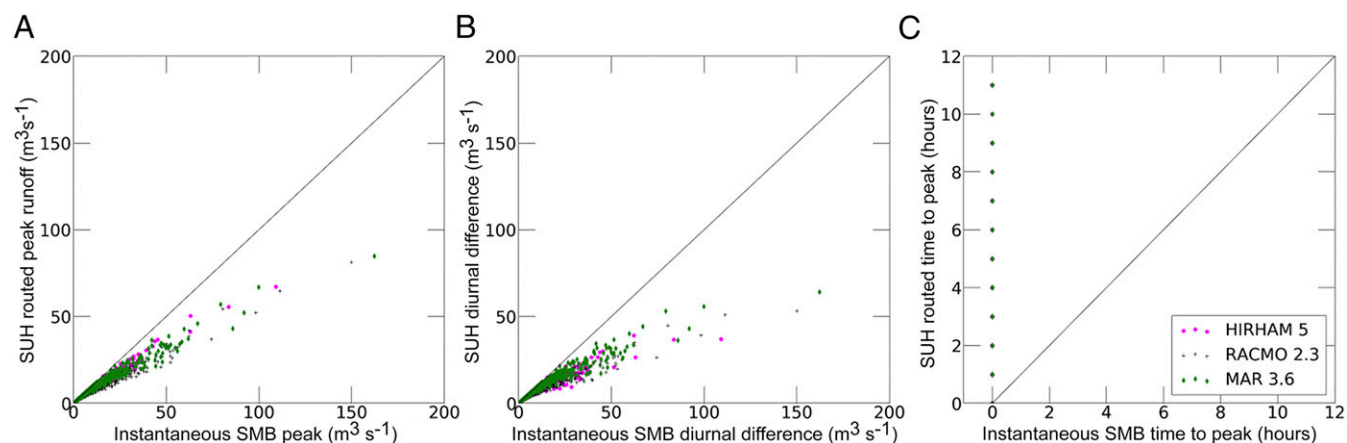


Fig. 6. Comparison of SUH-routed runoff (Fig. 5C) with instantaneous area-integrated runoff (Fig. 5B) for all 799 IDCs: (A) peak moulin discharge; (B) diurnal difference between maximum and minimum moulin discharge; and (C) time delay between peak melt production across the catchment and peak discharge received at the terminal moulin. Applying SUH routing to climate/SMB model output yields lower peak discharges, suppressed diurnal variability, and delayed, asynchronous timing of peak runoff delivered to catchment-terminating moulins.

observed discrepancies between modeled M and R and measured ice surface lowering and supraglacial river discharge, respectively. Runoff infiltration into crevasses (8) cannot explain the observed runoff deficit, because crevassed areas are eliminated from our minimum bounding catchment map (51.4 km^2) and are thus already included in the lower model uncertainty bounds of Fig. 7A (and Fig. 3). Although the possibility of additional, missed leakage cannot be fully ruled out, there is no evidence for this in our high-resolution UAV imagery (*SI Appendix, Discussion 1* and Fig. 3). Missed meltwater retention in seasonal snow also seems unlikely: the climate/SMB models indicate bare ice, and snow classifi-

cations from our UAV mapping and two WorldView-2 images confirm that Rio Behar catchment had $<6.5\%$ snow cover at the time of our field experiment, and perhaps as little as 0.9% (*SI Appendix, section 3.4* and Fig. 4). Remotely sensed retrievals of lake volume storage rule out the possibility of runoff impoundment in four supraglacial lakes contained within the Rio Behar catchment (*SI Appendix, section 3.3*). The remaining hypothesis (i.e., of water retention/refreezing in the bare-ice weathering crust) is explored further in *Discussion and Conclusions* and in the *SI Appendix*.

Regardless of mechanism, a first-order, empirical correction for any missed retention processes and/or model overestimations

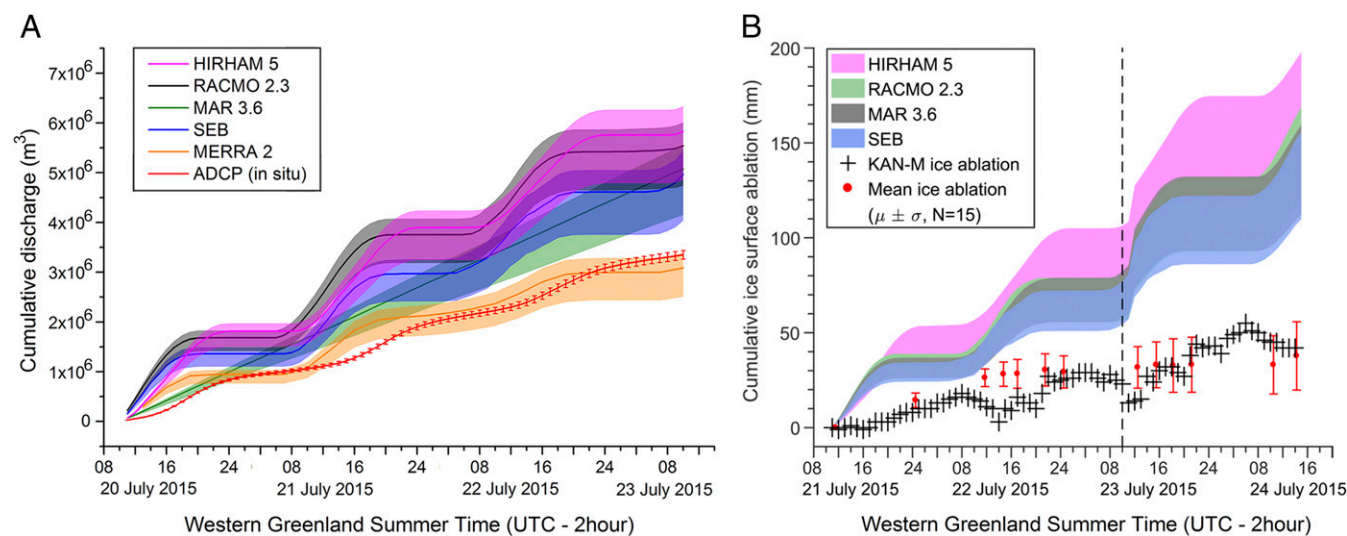


Fig. 7. Climate/SMB model simulations compared with field measurements of (A) runoff and (B) ice surface lowering (ablation) during the 20–23 July 2015 field experiment. (A) Cumulative hourly supraglacial runoff R from the Rio Behar catchment as measured from in situ ADCP measurements (in red) and as estimated by five climate/SMB models (color-shaded envelopes). Note that values of cumulative modeled R (m^3) derive from summation of hourly discharges ($\text{m}^3 \cdot \text{s}^{-1}$), which are obtained by multiplying climate/SMB model outputs with the remotely sensed catchment area(s) of Fig. 1. Upper and lower uncertainty bounds in modeled R thus reflect Rio Behar catchment area uncertainty, with centerlines denoting the optimal catchment area estimate of 63.1 km^2 and upper and lower uncertainty bounds reflecting maximum and minimum plausible catchment area estimates of 69.1 and 51.4 km^2 , respectively. Error bars (red) for in situ measurements denote the following: (A) Cumulative SDs calculated from multiple ADCP supraglacial river discharge measurements collected within each measurement hour; and (B) cumulative ice surface-lowering measurements as measured manually at 15 ablation stakes in our Rio Behar base camp (mean values also shown) and by the KAN_M AWS. Upper and lower uncertainty bounds in modeled ice ablation reflect assumptions of either solid ice ($0.918 \text{ g} \cdot \text{cm}^{-3}$) or lower observed ($0.688 \text{ g} \cdot \text{cm}^{-3}$) (50) bare-ice density to convert model outputs of M from units of liquid water equivalent to solid ice equivalent. The vertical dashed line in *B* indicates time of cessation of our ADCP discharge experiment in *A*. MERRA-2 is not shown in *B* because M is not supplied by MERRA-2. Local time for Rio Behar catchment is Coordinated Universal Time (UTC) minus 2 h.

of M for the Rio Behar catchment during our field experiment is supplied by a set of empirical, model-specific runoff coefficients relating observed runoff R to modeled melt production M for HIRHAM5, MAR3.6, RACMO2.3, and Point SEB (*SI Appendix, Table 3*). No values are supplied for MERRA-2 because M is not an output of this model. Although these coefficients are computationally identical to how runoff coefficients are calculated for terrestrial catchments (i.e., river discharge divided by catchment water input), they also include any missed model over- or underestimation of M and are more properly treated as correction factors for climate/SMB models instead of traditional runoff coefficients. For bare-ice surface conditions similar to those observed at the Rio Behar catchment during our field experiment, these correction factors may be multiplied by M to obtain alternate, lower estimates of M (here termed effective melt M') in addition to standard model output.

Discussion and Conclusions

Although the field protocol presented here is currently logistically impractical for sustained monitoring or deployment at numerous sites, it offers a useful, and perhaps only, direct way to independently measure supraglacial R for validating climate/SMB models used to simulate ice sheet runoff and associated inputs to subglacial and marine systems. Our provision of field-calibrated, model-specific runoff coefficients and SUH parameters offers an initial step in this direction, enabling generation of SUHs, peak moulin discharges (Q_{pk}), and runoff time-to-peak delays to moulins (t_p) from standard climate/SMB model outputs of melt production M (*SI Appendix, Table 3*) at a time of maximum drainage efficiency on the ice sheet surface.

Our successful retroactive testing of SUH runoff timing delays against in situ observations of two earlier field studies (8, 32) conducted in different years, locations, and elevations than Rio Behar catchment suggests plausible transferability of SUH to other areas of the GrIS ablation zone. One reason for this success may be that only three SUH parameters (C_p , C_r , and m) require in situ calibration; the others (t_p and h_p) derive purely from remotely sensed catchment characteristics and are thus adjusted individually for each IDC. That said, further field experiments are needed at other locations and times on the ice sheet to derive additional runoff coefficients and SUH parameters for differing surface conditions. Hydrological measurements from Haut Glacier d'Arolla, Switzerland, for example, suggest that earlier in the runoff season the presence of snow also suppresses diurnal contrasts and introduces delays between peak melt production and peak moulin discharge (55). Similarly, the seasonal evolution of supraglacial stream/river drainage networks may influence early-season runoff coefficients and the values of C_p , C_r , and m presented here due to lower stream density and/or temporary retention of runoff in slush and seasonal snow (43). Note that the most likely outcome of these processes would be to further delay runoff delivery to moulins (Fig. 6C), further suppress diurnal variability (Fig. 6B), and further suppress peak moulin discharges (Fig. 6A), rendering conservative our scientific conclusions about the influence of fluvial supraglacial catchments on meltwater delivery to moulins and the bed.

The field measurements and SUH calculations presented here illustrate the critical importance of IDCs in modulating the timing and magnitude of runoff evacuated off the ice surface to moulins (Figs. 4 and 5 and *SI Appendix, Fig. 11*). Previous studies have shown the importance of filling and draining supraglacial lake basins (20, 30, 56), but even in the absence of lake basins, runoff becomes unevenly redistributed over space and time due to water collection and transport through fluvial supraglacial stream/river catchments. Based on our observed values of C_p and C_r , these catchment-scale processes on ice are not unlike those on land (*SI Appendix, section 5.1*), despite known hydraulic differences between supraglacial and terrestrial channels (57).

Because IDC areas vary greatly and moulins convey meltwater quickly to the bed (32), the timing and volume of surface runoff received at the bed are thus arrhythmic in time and heterogeneous in space, unlike outputs from gridded climate/SMB models (Fig. 5 and *SI Appendix, Fig. 11*). Subdaily time lags between surface climatology and melt-induced ice motion are established first on the ice surface, which might otherwise be attributed to en- and/or subglacial delays or modes in melt-induced ice motion (8, 11, 12, 25, 30, 56), basal pressure (23), or subglacial drainage capacity (34). Diurnal variability in moulin discharge is lower than that of climate/SMB-modeled runoff fields, potentially reducing rates of inferred subglacial channelization (40). Where the diurnal variability of meltwater delivered to the bed is dampened by surface routing delays, there should be an impact on ice-sliding velocities, especially at higher elevations on the ice sheet. Using climate/SMB runoff to drive ice dynamics models in such areas could thus overestimate diurnal subglacial pressure variability, leading to small overestimations in the diurnal range of ice velocities and perhaps annual mean velocity as well. Conversely, large IDCs have the capacity to amplify moulin discharge, including at high elevations where melt rates are low but IDCs are large (43, 48), especially if moulins are first initiated through hydrofracturing and drainage of interior-advancing supraglacial lakes (21, 24, 58) then subjected to extreme and/or sustained melt events (59). In sum, the supraglacial drainage pattern on the GrIS surface influences a host of important subglacial processes, especially at short time scales.

Our finding that modeled and observed surface energy balances largely agree (*SI Appendix, Fig. 9*), yet both overestimate observed ice surface lowering and runoff (Fig. 7), leads us to hypothesize that subsurface melting and delay/retention/refreezing of meltwater in porous, low-density weathering crust may be an important bare-ice physical process not represented in the climate/SMB model simulations presented here. Shortwave radiation penetration and subsurface melting of bare ice certainly promotes the development of weathering crust (6, 53, 54) at our study site (*SI Appendix, Fig. 10*), which is characterized by abundant cryoconite holes and porous, water-saturated, low-density bare ice at least 1.1 m deep (50). Ablating weathering crust typically experiences less surface lowering than expected from skin surface energy balance calculations alone, due to internal melt within the subsurface ice matrix (50, 60, 61). Any meltwater retained within this porous medium—for example, due to deepening of the crust, enlargement of cryoconite holes, or enlargement of pore space volume—would result in model overestimation of R because current modeling schemes do not permit water retention in bare ice. Moreover, any refreezing of this meltwater (which we observed nightly during the field experiment) requires that it remelt to become true runoff, consuming additional melt energy not currently allocated in energy balance models for the bare-ice zone. Any model that correctly quantifies surface melt energy but does not simulate these processes will overestimate both ice surface lowering and runoff (*SI Appendix, Discussion I*).

Although mismatched scale and timing preclude direct comparison of our field results with GRACE (Gravity Recovery and Climate Experiment) satellite gravity data, we note in the *SI Appendix* that two previously published, sector-aggregated GRACE observations similarly show less actual mass loss than simulated by climate/SMB models (SMB-D) in some key melt-intensive sectors, including ours in southwest Greenland (62, 63) (*SI Appendix, Discussion II*). However, we are reluctant to draw general conclusions about climate/SMB model performance at other times or locations on the GrIS due to the short duration and small geographic area (relative to model domains) of our field experiment. The observed spread in modeled runoff estimates for the Rio Behar catchment (Fig. 7A) is consistent with a broader intercomparison of modeled outputs across the GrIS, including heightened model uncertainty in the ablation zone (64). New field experiments are needed to determine how to refine climate/SMB model simulations

of ice surface ablation and runoff in the bare-ice zone, as well as remote-sensing SMB estimates that use satellite/airborne altimetry measurements of ice surface lowering.

Regardless of absolute magnitudes of R , the timing and amplitude of meltwater runoff are clearly modified by fluvial geomorphology and fluvial catchment processes operating on the GrIS surface. Lateral flow routing through internally drained catchments predictably delays the arrival, reduces the peak discharge, and suppresses the diurnal variability of R entering moulins. Large catchments yield high moulin discharges, even at high elevations where overall melt rates are low. These realities, together with possible delays/retention/refreezing of runoff in bare-ice ablation zone weathering crust, signify that supraglacial drainage processes critically preconfigure the timing and flux of meltwater delivered to the bed. Incorporating fluvial catchments, hydrological theory, and field calibrations into ice sheet models should improve coupling of SMB with subglacial and marine systems.

- van den Broeke M, et al. (2009) Partitioning recent Greenland mass loss. *Science* 326: 984–986.
- Shepherd A, et al. (2012) A reconciled estimate of ice-sheet mass balance. *Science* 338: 1183–1189.
- Andersen ML, et al. (2015) Basin-scale partitioning of Greenland ice sheet mass balance components (2007–2011). *Earth Planet Sci Lett* 409:89–95.
- Enderlin EM, et al. (2014) An improved mass budget for the Greenland ice sheet. *Geophys Res Lett* 41:866–872.
- Chu VW (2014) Greenland ice sheet hydrology: A review. *Prog Phys Geogr* 38:19–54.
- Irvine-Fynn TDL, Hodson AJ, Moorman BJ, Vatne G, Hubbard AL (2011) Polythermal glacier hydrology: A review. *Rev Geophys* 49:RG4002.
- Smith LC, et al. (2015) Efficient meltwater drainage through supraglacial streams and rivers on the southwest Greenland ice sheet. *Proc Natl Acad Sci USA* 112:1001–1006.
- McGrath D, Colgan W, Steffen K, Lauffenburger P, Balog J (2011) Assessing the summer water budget of a moulin basin in the Sermeq Avannarleq ablation region, Greenland ice sheet. *J Glaciol* 57:954–964.
- Zwally HJ, et al. (2002) Surface melt-induced acceleration of Greenland ice-sheet flow. *Science* 297:218–222.
- Bartholomew TC, Anderson RS, Anderson SP (2008) Response of glacier basal motion to transient water storage. *Nat Geosci* 1:33–37.
- van de Wal RSW, et al. (2008) Large and rapid melt-induced velocity changes in the ablation zone of the Greenland ice sheet. *Science* 321:111–113.
- Schoof C (2010) Ice-sheet acceleration driven by melt supply variability. *Nature* 468: 803–806.
- Kulesa B, et al. (2017) Seismic evidence for complex sedimentary control of Greenland ice sheet flow. *Sci Adv* 3:e1603071.
- Lenaerts JTM, et al. (2015) Representing Greenland ice sheet freshwater fluxes in climate models. *Geophys Res Lett* 42:6373–6381.
- Machguth H, et al. (2016) Greenland meltwater storage in firn limited by near-surface ice formation. *Nat Clim Change* 6:390–393.
- Stokes CR, Margold M, Clark CD, Tarasov L (2016) Ice stream activity scaled to ice sheet volume during Laurentide ice sheet deglaciation. *Nature* 530:322–326.
- Rennermalm AK, et al. (2013) Evidence of meltwater retention within the Greenland ice sheet. *Cryosphere* 7:1433–1445.
- Van As D, et al. (2014) Increasing meltwater discharge from the Nuuk region of the Greenland ice sheet and implications for mass balance (1960–2012). *J Glaciol* 60: 314–322.
- Overeem I, et al. (2015) River inundation suggests ice-sheet runoff retention. *J Glaciol* 61:776–788.
- Bartholomew I, et al. (2011) Supraglacial forcing of subglacial drainage in the ablation zone of the Greenland ice sheet. *Geophys Res Lett* 38:L08502.
- Catania GA, Neumann TA (2010) Persistent englacial drainage features in the Greenland ice sheet. *Geophys Res Lett* 37:L02501.
- Covington MD, et al. (2012) Quantifying the effects of glacier conduit geometry and recharge on proglacial hydrograph form. *J Hydrol* 414–415:59–71.
- Wright PJ, Harper JT, Humphrey NF, Meierbachtol TW (2016) Measured basal water pressure variability of the western Greenland ice sheet: Implications for hydraulic potential. *J Geophys Res Earth Surf* 121:1134–1147.
- Fitzpatrick AAW, et al. (2014) A decade (2002–2012) of supraglacial lake volume estimates across Russell Glacier, West Greenland. *Cryosphere* 8:107–121.
- Banwell AF, Willis IC, Arnold NS (2013) Modeling subglacial water routing at Paakitsoq, W Greenland. *J Geophys Res Earth Surf* 118:1282–1295.
- Pitcher LH, Smith LC, Gleason CJ (2016) CryoSheds: A GIS modeling framework for delineating land-ice watersheds for the Greenland ice sheet. *Glsci Remote Sens* 53: 707–722.
- Lindbäck K, et al. (2015) Subglacial water drainage, storage, and piracy beneath the Greenland ice sheet. *Geophys Res Lett* 42:7606–7614.
- Chu W, Creyts TT, Bell RE (2016) Rerouting of subglacial water flow between neighboring glaciers in West Greenland. *J Geophys Res Earth Surf* 121:925–938.
- Gleason CJ, et al. (2015) Technical note: Semi-automated effective width extraction from time-lapse RGB imagery of a remote, braided Greenlandic river. *Hydro Earth Syst Sci* 19:2963–2969.
- Hoffman MJ, Catania GA, Neumann TA, Andrews LC, Rumlill JA (2011) Links between acceleration, melting, and supraglacial lake drainage of the western Greenland ice sheet. *J Geophys Res Earth Surf* 116:F04035.
- Bartholomew I, et al. (2012) Short-term variability in Greenland ice sheet motion forced by time-varying meltwater drainage: Implications for the relationship between subglacial drainage system behavior and ice velocity. *J Geophys Res Earth Surf* 117: F03002.
- Chandler DM, et al. (2013) Evolution of the subglacial drainage system beneath the Greenland ice sheet revealed by tracers. *Nat Geosci* 6:195–198.
- Andrews LC, et al. (2014) Direct observations of evolving subglacial drainage beneath the Greenland ice sheet. *Nature* 514:80–83.
- van de Wal RSW, et al. (2015) Self-regulation of ice flow varies across the ablation area in south-west Greenland. *Cryosphere* 9:603–611.
- Fausto RS, et al. (2016) The implication of nonradiative energy fluxes dominating Greenland ice sheet exceptional ablation area surface melt in 2012. *Geophys Res Lett* 43:2649–2658.
- van den Broeke MR, Smeets CJPP, van de Wal RSW (2011) The seasonal cycle and interannual variability of surface energy balance and melt in the ablation zone of the west Greenland ice sheet. *Cryosphere Discuss* 5:377–390.
- Nghiem SV, Steffen K, Kwok R, Tsai WY (2001) Detection of snowmelt regions on the Greenland ice sheet using diurnal backscatter change. *J Glaciol* 47:539–547.
- Hubbard BP, Sharp MJ, Willis IC, Nielsen MK, Smart CC (1995) Borehole water-level variations and the structure of the subglacial hydrological system of Haut Glacier d'Arolla, Valais, Switzerland. *J Glaciol* 41:572–583.
- Werder MA, Hewitt IJ, Schoof CG, Flowers GE (2013) Modeling channelized and distributed subglacial drainage in two dimensions. *J Geophys Res Earth Surf* 118: 2140–2158.
- Hewitt IJ (2013) Seasonal changes in ice sheet motion due to melt water lubrication. *Earth Planet Sci Lett* 371–372:16–25.
- van As D, et al. (2017) Hypsometric amplification and routing moderation of Greenland ice sheet meltwater release. *Cryosphere* 11:1371–1386.
- Steger CR, et al. (2017) Firn meltwater retention on the Greenland ice sheet: A model comparison. *Front Earth Sci* 5:16.
- Yang K, Smith LC (2016) Internally drained catchments dominate supraglacial hydrology of the southwest Greenland ice sheet. *J Geophys Res Earth Surf* 121: 1891–1910.
- Snyder FF (1938) Synthetic unit-graphs. *Trans Am Geophys Union* 19:447–454.
- Chow VT (1964) *Handbook of Applied Hydrology: A Compendium of Water-Resources Technology* (McGraw-Hill Company, New York), 1st Ed.
- Yang K, Smith LC, Chu VW, Gleason CJ, Li M (2015) A caution on the use of surface digital elevation models to simulate supraglacial hydrology of the Greenland ice sheet. *IEEE J Sel Top Appl Earth Obs Remote Sens* 8:5212–5224.
- Singh PK, Mishra SK, Jain MK (2014) A review of the synthetic unit hydrograph: From the empirical UH to advanced geomorphological methods. *Hydro Sci J* 59:239–261.
- Poinar K, et al. (2015) Limits to future expansion of surface-melt-enhanced ice flow into the interior of western Greenland. *Geophys Res Lett* 42:1800–1807.
- Wyatt FR, Sharp MJ (2015) Linking surface hydrology to flow regimes and patterns of velocity variability on Devon Ice Cap, Nunavut. *J Glaciol* 61:387–399.
- Cooper MG, et al. (2017) Near-surface meltwater storage in low density bare ice of the Greenland ice sheet ablation zone. *Cryosphere Discuss* 1–25.
- Braithwaite RJ, Konzelmann T, Marty C, Olesen OB (1998) Errors in daily ablation measurements in northern Greenland, 1993–94, and their implications for glacier climate studies. *J Glaciol* 44:583–588.
- Bennartz R, et al. (2013) July 2012 Greenland melt extent enhanced by low-level liquid clouds. *Nature* 496:83–86.
- van den Broeke M, et al. (2008) Partitioning of melt energy and meltwater fluxes in the ablation zone of the west Greenland ice sheet. *Cryosphere* 2:179–189.

54. Cook JM, Hodson AJ, Irvine-Fynn TDL (2016) Supraglacial weathering crust dynamics inferred from cryoconite hole hydrology. *Hydrol Processes* 30:433–446.
55. Willis IC, Arnold NS, Brock BW (2002) Effect of snowpack removal on energy balance, melt and runoff in a small supraglacial catchment. *Hydrol Processes* 16: 2721–2749.
56. Shepherd A, et al. (2009) Greenland ice sheet motion coupled with daily melting in late summer. *Geophys Res Lett* 36:L01501.
57. Gleason CJ, et al. (2016) Characterizing supraglacial meltwater channel hydraulics on the Greenland ice sheet from in situ observations. *Earth Surf Processes Landforms* 41: 2111–2122.
58. Leeson AA, Shepherd A, Palmer S, Sundal A, Fettweis X (2012) Simulating the growth of supraglacial lakes at the western margin of the Greenland ice sheet. *Cryosphere* 6: 1077–1086.
59. Tedesco M, et al. (2013) Evidence and analysis of 2012 Greenland records from spaceborne observations, a regional climate model and reanalysis data. *Cryosphere* 7:615–630.
60. Hoffman MJ, Fountain AG, Liston GE (2014) Near-surface internal melting: A substantial mass loss on Antarctic Dry Valley glaciers. *J Glaciol* 60:361–374.
61. Müller F, Keeler C (1969) Errors in short-term ablation measurements on melting ice surfaces. *J Glaciol* 8:91–105.
62. Sasgen I, et al. (2012) Timing and origin of recent regional ice-mass loss in Greenland. *Earth Planet Sci Lett* 333–334:293–303.
63. Xu Z, Schrama EJO, van der Wal W, van den Broeke M, Enderlin EM (2016) Improved GRACE regional mass balance estimates of the Greenland ice sheet cross-validated with the input–output method. *Cryosphere* 10:895–912.
64. Vernon CL, et al. (2013) Surface mass balance model intercomparison for the Greenland ice sheet. *Cryosphere* 7:599–614.

1 **Supporting Information (SI)**

2 (Smith et al., “Direct measurements of meltwater runoff on the Greenland ice sheet surface”)

3

4 **Table of Contents**

5

6 **Methods 1. Field measurements and data processing**

7 1.1 Field measurements of discharge from Acoustic Doppler Current Profiler (ADCP)

8 *Figure S1: Acoustic Doppler Current Profiler (ADCP) supraglacial river gauging site*

9 1.2 ADCP data collection and processing (GET FROM OLD SI)

10 *Table S1: Rio Behar discharge data*

11 1.3 Field measurements of ice surface lowering (ablation)

12 *Figure S2: Photographs of base camp and KAN_M ice ablation measurement sites*

13 **Methods 2. Remote sensing data**

14 2.1 Satellite image and digital elevation model (DEM) products

15 *Table S2: Remotely sensed datasets used in this study*

16 2.2. Unmanned Aerial Vehicle (UAV)

17 *Figure S3: WorldView-1 and UAV discrimination of small supraglacial streams*

18 **Methods 3. Remote sensing data processing**

19 3.1 Image processing of stereo-photogrammetric DEMs from WorldView satellite imagery

20 3.2 Image processing of WorldView satellite imagery

21 3.3 Remote sensing of supraglacial lake volumes

22 3.4 Snow classifications

23 *Figure S4: WorldView-2 and UAV snow cover classifications*

24 **Methods 4. Supraglacial hydrograph analysis**

25 4.1 Recession flow

26 4.2 Hydrograph separation

27 *Figure S5: Rio Behar hydrograph separation and model-specific unit hydrographs*

28 4.3 Runoff coefficients (correction factors) relating modeled M to observed R

29 *Table S3: Rio Behar catchment runoff coefficients/correction factors and SUH*

30 *parameters*

31 4.4 Unit Hydrograph (UH) derivation

32 **Methods 5. Application of Synthetic Unit Hydrograph (SUH) routing to 799 IDCs**

33 5.1 Derivation of Synthetic Unit Hydrograph (SUH) model parameters for 799 IDCs

34 *Figure S6: Determination of Gamma function shape factor*

35 5.2 Generation of model-driven synthetic hydrographs for 799 IDCs

36 5.3 Retroactive validation of SUH using field data of McGrath *et al.* and Chandler *et al.*

37 *Table S4: Retroactive validation of SUH using field data of McGrath et al. and*

38 *Chandler et al.*

39 **Methods 6: Regional climate/SMB model descriptions and data analysis**

40 6.1 HIRHAM5

41 6.2 MAR3.6

42 6.3 RACMO2.3

43 6.4 MERRA-2

44 6.5 Point SEB

45 6.6 Reprojection of all model outputs to a common resolution and grid

46 6.7 Comparison of model outputs with field observations from Rio Behar catchment

47 *Table S5: Climate/SMB model and field measurements of M and R*

48 *Figure S7: Decomposed SMB variables for MAR3.6*

49 *Figure S8: Comparison of ERA-Interim and MERRA-2 climate reanalysis during the*
50 *field experiment*

51 6.8 Comparison of RACMO2.3 albedo and surface energy balance with AWS measurements

52 *Figure S9: Comparison of RACMO2.3 and KAN_M AWS surface radiation and energy*
53 *balance components during the Rio Behar field experiment*

54

55 **Supplementary Discussion I: Weathering crust hypothesis for model overestimation of runoff**
56 **ice surface lowering and supraglacial river runoff**

57 *Figure S10: Photographs of weathering crust and solid ice*

58 **Supplementary Discussion II: Scale issue and compatibility with GRACE studies**

59 **Supplementary Figure S11: Companion figure to Figure 5 (nighttime runoff)**

60 **Supplementary Figure S12: Recolored version of Figure 4 for color-blind readers**

61 **Supplementary References**

62

63 * * *

64

65 **Methods 1. Field measurements and data processing**

66 Rio Behar catchment is a moderate sized supraglacial IDC (internally drained catchment)
67 located on the southwestern GrIS surface (**Figure 1**; see also small black star, **Figure 4**, **Figure 5**,
68 **Figure S11**). Owing to rapidly melting conditions on the ablation zone, permanent gauging
69 installations are infeasible. From July 17-24, 2015 we established a temporary base camp and
70 supraglacial river discharge gauging installation in the main-stem supraglacial river (termed “Rio
71 Behar”) at 67.049598N, -49.0201453W, immediately downstream of the confluence of Rio
72 Behar catchment’s two largest tributaries and lake spillway, approximately 300 m upstream of
73 the catchment’s terminal moulin.

74 1.1. Acoustic Doppler Current Profiler (ADCP) field experiment:

75 For 72 continuous hours on July 20-23, 2015 we collected in situ Acoustic Doppler Current
76 Profiler (ADCP) measurements of supraglacial river discharge (Q) in Rio Behar, using a bank-
77 operated cableway system anchored to the ice surface (**Figure S1**). The cableway was used to

87 repeatedly tow a SonTek® M9 ADCP mounted on a Hydroboard II back and forth across the
88 river channel, thus obtaining hydrographic profiles of changing channel cross-section, wetted
89 perimeter, and velocity 3-6 times per hour beginning 1:16:34 PM (UTC) July 20, 2015 and
90 ending 12:12:11 PM (UTC) July 23, 2015 (local western Greenland time was UTC-2:00). ADCP
91 measurements were acquired hourly to capture a wide range of discharge values and to avoid
92 reliance on a stage-discharge rating curve (from field observations in 2015 and previously,
93 ongoing thermal erosion of large GrIS supraglacial river channels quickly renders rating curves
94 obsolete). This requirement of around-the-clock in situ ADCP measurements, rather than
95 simply a water level recorder, is the reason for the 72-hour duration of the field experiment.



87
88 **Figure S1. Measurements of supraglacial river discharge were collected continuously for 72 hours**
89 **approximately 300 m upstream of the Rio Behar catchment terminal moulin, using an Acoustic**
90 **Doppler Current Profiler (ADCP) operated by rotating shifts of technicians safely tethered to the ice. A**
91 **bank operated cableway system was used to repeatedly tow the ADCP back and forth across the**
92 **channel (photo by Åsa Rennermalm).**

93

94 1.2 Acoustic Doppler Current Profiler (ADCP) data collection and processing:

95 Given that the ADCP discharges represent the core dataset of this study, the measurements are
96 described in detail. The Sontek® M9 ADCP uses real-time-kinematic (RTK) GPS precision and
97 Doppler technology to measure channel cross sectional area and velocity. The Doppler principle
98 assumes that suspended particles in the water column travel at the same speed as water and
99 the change in frequency detected by each acoustic transducer is translated into a velocity using
100 the speed of sound, calculated from temperature and salinity.

101 While in transect, the ADCP determines its position using (1) bottom tracking, (2) GPS GGA and
102 (3) GPS VTG. Note that GGA and VTG refer to NMEA-0183 protocols for outputting GPS
103 instrument position, quality and velocity information(1). GPS data are acquired at up to 10 Hz
104 and read directly by the ADCP using the NMEA-0183 standard protocol. All three track
105 references are logged for each transect, with the most accurate one selected during post-
106 processing. The ADCP uses the East, North, Up (ENU) coordinate system because it allows for
107 free movement and rotation of the ADCP with respect to the cableway orientation. Orientation
108 of the ADCP is measured using a magnetic compass which was regularly calibrated on site.

109 The ADCP data were collected and post-processed using SonTek® RiverSurveyor Live software.
110 The post-processing consisted of verifying proper settings, including applying a site specific -
111 29.4 magnetic declination compensation to align to magnetic north, a constant 0.06 m
112 transducer depth offset, choosing the appropriate track reference, depth reference, and
113 screening for poor quality data. When GPS Quality = 4, indicating RTK positioning, GPS GGA
114 was selected as the track reference. GPS GGA was selected over bottom tracking due to
115 occasional anomalous samples and the unknown effects of bottom tracking on ice. For GPS
116 quality below Quality = 4, the GPS parameters were evaluated further and the track reference
117 was chosen per GPS quality, HDOP, and the number of logged satellites. Next, width and
118 velocity were evaluated with the selected track reference. Transects were removed if width was
119 an outlier or if a significant number of velocity profiles were missing. Velocity vectors were
120 analyzed visually for uniform and homogenous flow. If velocity vectors indicated significant
121 non-uniform flow, the measurement was excluded (**Table S1**).

122 The ADCP assumes homogenous flow therefore all beams must measure the same velocity
123 field. If one or more beams separate from the others, velocity and tracking ability of the system
124 is compromised. Under uniform flow conditions the signal-to-noise-ratios (SNR) of all 4 beams
125 converge and trend together, showing the same signal decay throughout the water column.
126 Divergence of the SNR from one or more of the beams is an indication of beam separation. SNR
127 vs. depth plots were visually reviewed for each measurement to inspect for beam separation.
128 Occasional beam separation is to be expected in turbulent flow environments and was
129 considered acceptable; however, transects with consistent, significant beam separation were
130 excluded.

131 The ADCP collects depth using an independent vertically-oriented sensor, as well as an average
132 depth recorded by four angled velocity beam sensors used for bottom tracking. The vertical
133 beam depth was used as the primary depth reference in this study because: (1) it is oriented
134 flush with M9 face; (2) The four velocity beams are oriented slanted relative to the face of the
135 ADCP and thus also the channel bed; (3) Depth from the velocity beams is calculated as the
136 average depth from the 4 beams, which can sometimes overly smooth bathymetry; (4) The

137 cableway-tethered Hydroboard provides a stable platform which helps minimize the effect of
138 vertical beam sensor tilt, which is not otherwise compensated for by RiverSurveyor Live
139 software; (5) The ADCP's vertical beam is wider than the velocity beams, signifying there would
140 be no significant change in measured depth given that sensor tilt angles were small. For these
141 five reasons, the vertical beam depth was chosen as the primary depth reference. When data
142 are missing from one depth reference the ADCP fills in missing data using the previous depth
143 reference. If the vertical beam reports an anomalous value while in transect, the bottom track
144 was chosen for the depth reference. For each profile, cross sectional area was evaluated and
145 transects with outliers were excluded.

146 The ADCP has a minimum depth range of approximately 30 cm, therefore the shallow margins
147 of the channel cannot be directly measured. The RiverSurveyor Live software uses stationary
148 edge measurements collected on each bank to estimate the discharge of the unmeasured
149 portion of the channel. The stationary edge measurements included manually estimating the
150 distance from the edge of the water to the ADCP on site, and collecting a minimum of 10
151 velocity profiles at the minimum readable depth. While post processing, transects with no edge
152 data on both banks were removed. Transects with reliable edge data on only one bank were
153 removed when other transects within a measurement hour contain accurate edge data. In this
154 reach of the Rio Behar, most of the flow was carried through the central portion of the channel
155 where reliable depth and velocity data were collected – thus we deem uncertainty due to
156 limited velocity cells at the edge of each profile to be minimal.

157 Each measurement time was manually copied from a Matlab file generated by River Surveyor
158 Live. The time is stored in the GPS.Utc structure array formatted as hhmmss.s. No data
159 GPS.Utc values were ignored and the minimum recorded time from the first profile collected in
160 each hour was assigned as the measurement start time, and the maximum recorded time from
161 the last profile collected in each measurement hour was assigned as the measurement end
162 time. After manual quality control checks and removal of anomalous transects, the mean
163 discharge and standard deviation were calculated for remaining transects in each measurement
164 hour to yield a final, averaged discharge measurement and associated measurement standard
165 deviation (**Table S1**).

166

167

168

169

170 **Supplementary Data Table S1:** Quality-controlled Acoustic Doppler Current Profiler (ADCP)
 171 measurements of supraglacial river discharge and associated standard deviations collected in
 172 the Rio Behar (67.049598N, -49.0201453W).

| Hour | Date | Start Time (UTC) | End Time (UTC) | Mean Discharge (Q) m ³ s ⁻¹ | Standard Deviation (Q) m ³ s ⁻¹ | Number ADCP Profiles Used | Number ADCP Profiles Collected |
|------|-----------|------------------|----------------|---|---|---------------------------|--------------------------------|
| 1 | 7/20/2015 | 1:16:34 PM | 1:24:59 PM | 8.17 | 0.33 | 2 | 4 |
| 2 | 7/20/2015 | 1:58:58 PM | 2:22:51 PM | 7.14 | 0.61 | 2 | 6 |
| 3 | 7/20/2015 | 3:09:28 PM | 3:22:43 PM | 7.98 | 0.08 | 4 | 4 |
| 4 | 7/20/2015 | 4:10:00 PM | 4:21:30 PM | 9.96 | 0.22 | 4 | 4 |
| 5 | 7/20/2015 | 5:29:44 PM | 5:39:04 PM | 13.77 | 0.21 | 4 | 4 |
| 6 | 7/20/2015 | 6:24:16 PM | 6:27:28 PM | 17.31 | 0.95 | 3 | 4 |
| 7 | 7/20/2015 | 7:34:21 PM | 7:45:52 PM | 21.33 | * | 1 | 4 |
| 8 | 7/20/2015 | 8:41:43 PM | 8:55:11 PM | 24.87 | 0.89 | 3 | 4 |
| 9 | 7/20/2015 | 9:43:09 PM | 9:54:51 PM | 26.73 | 0.76 | 4 | 4 |
| 10 | 7/20/2015 | 10:41:51 PM | 11:03:06 PM | 25.50 | 0.50 | 3 | 6 |
| 11 | 7/20/2015 | 11:42:26 PM | 11:54:32 PM | 22.80 | 0.34 | 4 | 4 |
| 12 | 7/20/2015 | 12:45:08 AM | 12:54:42 AM | 19.60 | 0.45 | 5 | 5 |
| 13 | 7/20/2015 | 1:48:29 AM | 1:56:33 AM | 15.66 | 0.86 | 2 | 3 |
| 14 | 7/21/2015 | 2:41:31 AM | 2:49:30 AM | 11.92 | 0.34 | 4 | 4 |
| 15 | 7/21/2015 | 3:06:19 AM | 3:13:42 AM | 10.15 | 0.51 | 3 | 4 |
| 16 | 7/21/2015 | 4:00:02 AM | 4:06:54 AM | 8.63 | 0.71 | 3 | 4 |
| 17 | 7/21/2015 | 5:06:27 AM | 5:14:59 AM | 6.01 | 0.36 | 3 | 4 |
| 18 | 7/21/2015 | 5:53:43 AM | 6:05:30 AM | 6.25 | 0.35 | 2 | 4 |
| 19 | 7/21/2015 | 6:55:17 AM | 7:13:10 AM | 5.38 | 0.23 | 4 | 4 |
| 20 | 7/21/2015 | 7:48:33 AM | 8:10:16 AM | 4.72 | 0.69 | 3 | 6 |
| 21 | 7/21/2015 | 9:15:21 AM | 9:26:41 AM | 4.61 | 0.23 | 3 | 4 |
| 22 | 7/21/2015 | 10:11:00 AM | 10:18:30 AM | 5.10 | 0.18 | 3 | 4 |
| 23 | 7/21/2015 | 11:10:00 AM | 11:16:30 AM | 5.46 | 0.19 | 4 | 4 |
| 24 | 7/21/2015 | 12:11:40 PM | 12:21:00 PM | 6.00 | 0.10 | 4 | 4 |
| 25 | 7/21/2015 | 12:59:20 PM | 1:08:20 PM | 6.59 | 0.08 | 4 | 4 |
| 26 | 7/21/2015 | 2:06:50 PM | 2:16:20 PM | 7.05 | 0.06 | 3 | 4 |
| 27 | 7/21/2015 | 3:10:30 PM | 3:19:30 PM | 7.89 | 0.13 | 4 | 4 |
| 28 | 7/21/2015 | 4:09:20 PM | 4:21:30 PM | 9.00 | 0.54 | 5 | 6 |
| 29 | 7/21/2015 | 5:10:50 PM | 5:22:30 PM | 12.65 | 0.19 | 4 | 4 |
| 30 | 7/21/2015 | 6:05:40 PM | 6:15:40 PM | 16.15 | 0.091 | 3 | 4 |
| 31 | 7/21/2015 | 6:57:10 PM | 7:07:20 PM | 19.28 | 0.70 | 3 | 4 |
| 32 | 7/21/2015 | 8:04:20 PM | 8:14:20 PM | 22.16 | 0.693 | 4 | 4 |
| 33 | 7/21/2015 | 8:59:30 PM | 9:07:10 PM | 23.9 | 0.404 | 2 | 4 |
| 34 | 7/21/2015 | 10:00:20 PM | 10:08:30 PM | 25.54 | 0.771 | 4 | 4 |
| 35 | 7/21/2015 | 10:55:10 PM | 11:03:30 PM | 25.2 | * | 1 | 4 |
| 36 | 7/22/2015 | 12:01:58 AM | 12:11:09 AM | 21.7 | 0.857 | 3 | 4 |
| 37 | 7/22/2015 | 12:58:15 AM | 1:05:30 AM | 19.06 | 0.452 | 4 | 4 |

| | | | | | | | |
|--|-----------|-------------|-------------|-------|-------|---|---|
| 38 | 7/22/2015 | 2:03:15 AM | 2:12:15 AM | 16.38 | 0.398 | 4 | 4 |
| 39 | 7/22/2015 | 3:15:19 AM | 3:23:24 AM | 14.1 | 0.173 | 4 | 4 |
| 40 | 7/22/2015 | 4:06:03 AM | 4:12:43 PM | 11.82 | 0.252 | 4 | 4 |
| 41 | 7/22/2015 | 5:01:09 AM | 5:06:20 AM | 10.78 | 0.292 | 3 | 4 |
| 42 | 7/22/2015 | 6:09:16 AM | 6:19:04 AM | 9.208 | 0.269 | 4 | 4 |
| 43 | 7/22/2015 | 7:08:18 AM | 7:16:08 AM | 8.585 | 0.488 | 4 | 4 |
| 44 | 7/22/2015 | 8:32:49 AM | 8:39:51 AM | 7.856 | 0.108 | 4 | 4 |
| 45 | 7/22/2015 | 8:53:01 AM | 8:59:09 AM | 7.578 | 0.092 | 4 | 4 |
| 46 | 7/22/2015 | 10:42:50 AM | 10:50:58 AM | 7.434 | 0.119 | 4 | 4 |
| 47 | 7/22/2015 | 11:09:01 AM | 11:16:03 AM | 7.566 | 0.155 | 4 | 4 |
| 48 | 7/22/2015 | 12:06:39 PM | 12:13:32 PM | 7.698 | 0.087 | 4 | 4 |
| 49 | 7/22/2015 | 1:42:29 PM | 1:52:14 PM | 8.647 | 0.211 | 4 | 5 |
| 50 | 7/22/2015 | 2:10:39 PM | 2:18:07 PM | 9.352 | 0.349 | 4 | 4 |
| 51 | 7/22/2015 | 3:09:29 PM | 3:18:30 PM | 12.11 | 0.144 | 4 | 4 |
| 52 | 7/22/2015 | 4:00:17 PM | 4:10:12 PM | 14.3 | 0.384 | 4 | 4 |
| 53 | 7/22/2015 | 5:06:23 PM | 5:13:14 PM | 17.99 | 0.798 | 4 | 4 |
| 54 | 7/22/2015 | 6:05:37 PM | 6:13:15 PM | 20.63 | 0.849 | 4 | 4 |
| 55 | 7/22/2015 | 7:00:30 PM | 7:07:41 PM | 22.06 | 0.539 | 4 | 4 |
| 56 | 7/22/2015 | 8:00:10 PM | 8:06:52 PM | 21.99 | 0.275 | 4 | 4 |
| 57 | 7/22/2015 | 9:05:02 PM | 9:12:32 PM | 21.75 | 0.442 | 4 | 4 |
| 58 | 7/22/2015 | 9:59:52 PM | 10:09:40 PM | 20.58 | 0.393 | 4 | 4 |
| 59 | 7/22/2015 | 11:01:57 PM | 11:09:26 PM | 19.76 | 0.209 | 4 | 4 |
| 60 | 7/23/2015 | 12:03:02 AM | 12:09:31 AM | 17.68 | 0.401 | 4 | 4 |
| 61 | 7/23/2015 | 1:04:40 AM | 1:10:59 AM | 15.88 | 0.147 | 4 | 4 |
| 62 | 7/23/2015 | 1:59:57 AM | 2:05:26 AM | 13.36 | 0.19 | 4 | 4 |
| 63 | 7/23/2015 | 3:02:19 AM | 3:08:15 AM | 10.01 | 0.147 | 4 | 4 |
| 64 | 7/23/2015 | 3:59:34 AM | 4:05:21 AM | 9.525 | 0.386 | 4 | 4 |
| 65 | 7/23/2015 | 5:00:03 AM | 5:13:52 AM | 8.672 | 0.222 | 2 | 6 |
| 66 | 7/23/2015 | 6:19:54 AM | 6:28:09 AM | 6.65 | 0.147 | 3 | 4 |
| 67 | 7/23/2015 | 7:00:43 AM | 7:08:35 AM | 7.198 | 0.007 | 3 | 4 |
| 68 | 7/23/2015 | 8:15:43 AM | 8:23:19 AM | 6.545 | 0.264 | 2 | 4 |
| 69 | 7/23/2015 | 9:00:05 AM | 9:09:22 AM | 7.044 | 0.159 | 4 | 4 |
| 70 | 7/23/2015 | 10:08:58 AM | 10:16:04 AM | 6.104 | 0.053 | 3 | 4 |
| 71 | 7/23/2015 | 11:00:27 AM | 11:07:41 AM | 6.128 | 0.08 | 4 | 4 |
| 72 | 7/23/2015 | 12:05:03 PM | 12:12:11 PM | 6.586 | 0.082 | 4 | 4 |
| * standard deviation is not calculated because only one ADCP profile remained after quality control and data filtering | | | | | | | |

173

174

175

176

177 1.3 Field measurements of ice surface lowering (ablation):

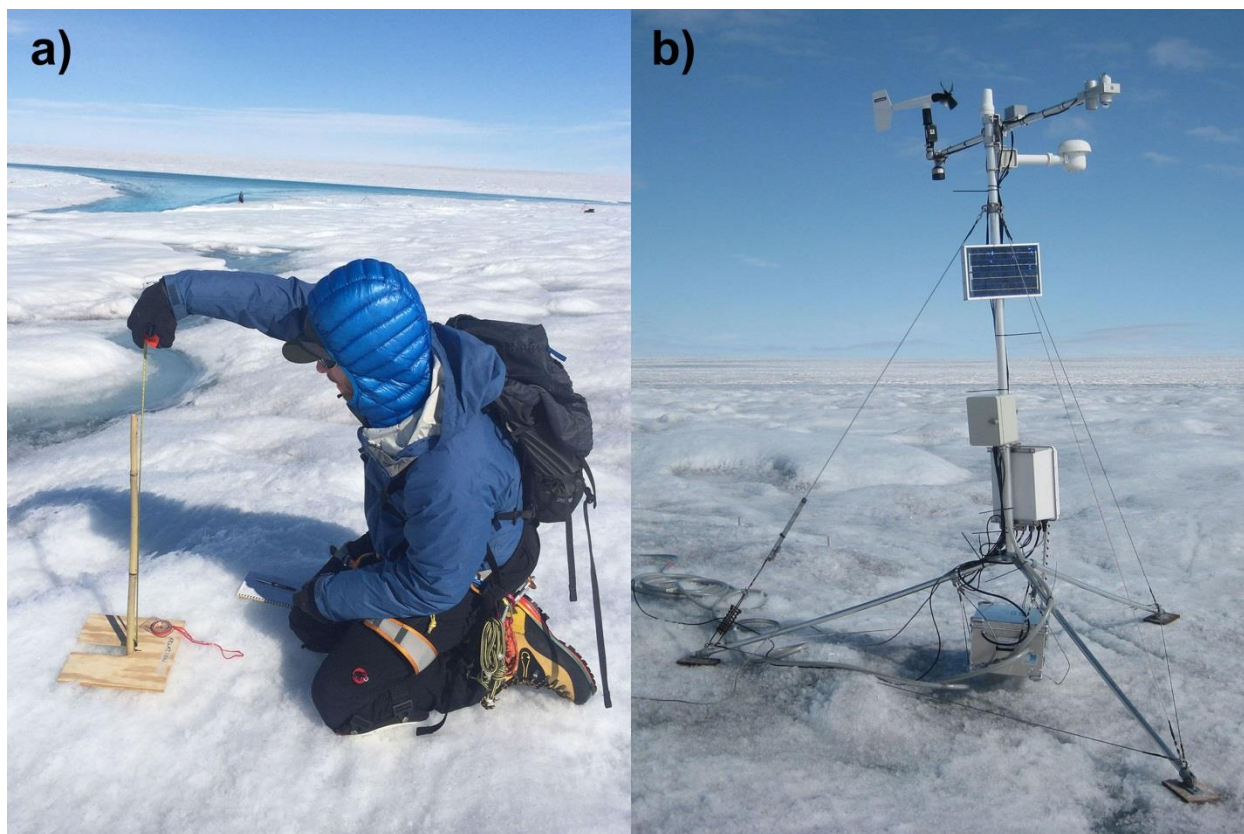
178 Ice surface ablation measurements:

179 Repeated ice surface lowering measurements were collected at fifteen bamboo ablation stakes
180 distributed around our ADCP ice camp (black star, **Figure 1**). Fifteen stakes were placed at
181 random distance/direction pairs from a common center to capture spatial variation in ablation.
182 Thirteen stakes were in weathering crust which was the typical ice surface at the site. One
183 stake was placed in a remnant patch of seasonal snow underlain by solid ice, and one in a patch
184 of solid bare ice covered in dispersed cryoconite debris. Stakes were drilled at least 1 m deep
185 into the surface and left to freeze in for 24 hours before initiating measurements. Prior to each
186 measurement, a 24 x 24 cm wooden “ablation board” was placed at the foot of each stake
187 (**Figure S2a**). The board was oriented to true north and measurements were made from a
188 marked point on the base of the board to a marked point at the top of the stake. This protocol
189 minimized errors due to local variations in ice sheet surface micro-topography or shifts in
190 measurement datum. Careful inspection of each stake was made prior to each measurement.
191 To ensure accurate surface lowering measurements, all stakes were pressed firmly downward
192 prior to measurement to ensure that any loosening stakes were properly seated in the bottom
193 of their drill holes. Changes in ice sheet surface height were measured at sub-daily intervals (~3
194 to 12 hours). A total of thirteen, sub-daily surveys of the heights of each stake above the ice
195 surface were conducted between 1100 July 21 and 1415 July 24, 2015. Data from all 15 stakes
196 were averaged together and their standard deviations computed to mitigate for known spatial
197 variability in ablation stake courses (2).

198 Approximately 9.1 km east of our base camp, hourly changes in ice surface height were
199 obtained from a downward-looking Campbell Scientific SR50A sonic ranger fitted on the
200 KAN_M Automatic Weather Station (AWS), located just outside the 2015 Rio Behar catchment
201 boundary (67.0667N, -48.8327W, 1270 m a.s.l., see **Figure 1**). These data have at least ~1 cm
202 vertical uncertainty owing to pressure-transducer correction and sensor noise. Use of raw
203 surface lowering data from this sensor and our ablation stakes is appropriate for estimation of
204 M during our field experiment in late July, as there was no new snow accumulation and
205 negligible refreezing or sublimation in above-zero air temperatures. Meteorological data from
206 the KAN_M AWS were also used to supply the necessary inputs to run the point SEB model.
207 The KAN_M AWS is maintained by the Geological Survey of Denmark and Greenland (GEUS), as
208 part of the Greenland Analogue Project and the Programme for Monitoring of the Greenland
209 Ice Sheet (www.PROMICE.dk).

210 To compare climate/SMB model outputs of melt M (mm liquid water) directly with the
211 described surface lowering data, model outputs of M were converted to units of solid ice
212 equivalent (mm). To provide associated uncertainty ranges on these conversions, two different

213 ice densities were assumed: 0.688 g cm^{-3} (the average near-surface ice density from ten
214 shallow cores obtained at the Rio Behar base camp site, from Cooper, *et al.* (3)) and 0.918 g cm^{-3}
215 3 (density of pure solid ice) to provide an upper and lower bound of ice surface lowering,
216 respectively. The resultant ranges of modeled ice surface lowering due to M are presented
217 alongside field measurements in **Figure 7b**.



218
219 **Figure S2: Surface lowering data were collected from (a) manual steel tape measurements at fifteen**
220 **bamboo ablation stakes distributed around Rio Behar base camp; and (b) sonic ranging data from the**
221 **PROMICE KAN_M automated weathering station maintained by the Geological Survey of Denmark**
222 **and Greenland (GEUS). Base camp and KAN_M station locations are shown in Figure 1. Photos by (a)**
223 **Åsa K. Rennermalm and (b) Dirk van As.**

224
225 **2. Remote sensing data**

226 Remotely sensed datasets consisted mainly of high resolution WorldView-1/2 satellite imagery
227 and associated digital elevation models (DEMs) derived from stereo-photogrammetry, and RGB
228 camera images acquired from a custom built fixed-wing UAV (4) (drone). Archived WorldView
229 satellite data were also used to test our Synthetic Unit Hydrograph (SUH) model against two
230 previous field studies (5, 6). A previously published map (7) of supraglacial internally drained

231 catchments (IDCs) derived from a 19 August 2013 panchromatic Landsat-8 image supplied the
 232 799 IDC boundaries used in this study, and daily MODIS albedo retrievals (MYD10A1 product)
 233 used to validate (RACMO2.3) or drive (HIRHAM5) climate/SMB albedo. A summary table of
 234 these data, including product ID numbers, acquisition dates, and what they were used for is
 235 presented in **Table S2**.

236 **Table S2: Remotely sensed datasets used in this study**

| Dataset type | ID | Spatial resolution | Acquisition date | Purpose |
|-------------------------------|------------------------|--------------------|-------------------|--|
| WorldView-1 satellite imagery | 102001004202CD00 | 0.5 m | 18 July 2015 | Detailed mapping of supraglacial hydrologic features (rivers, lakes, moulins, channel heads), and stereo-photogrammetric DEM generation |
| | 1020010043165100 | 0.5 m | 18 July 2015 | Stereo-photogrammetric DEM generation and catchment boundary extraction |
| | 10200100354A5700 | 0.5 m | 29 October 2014 | |
| | 1020010034334B00 | 0.5 m | 29 October 2014 | |
| | 102001003376CE00 | 0.5 m | 19 September 2014 | |
| | 10200100318C0D00 | 0.5 m | 19 September 2014 | |
| | 1020010008AB4800 | 0.5 m | 15 July 2009 | McGrath <i>et al.</i> (6) SUH case study |
| | 103001000CB46800 | 0.5 m | 12 July 2011 | Chandler <i>et al.</i> (5) SUH case study |
| WorldView-2 satellite imagery | 1030010046354000 | 2.0 m | 17 July 2015 | Mapping snow covered area; Calculating supraglacial lake depth; Comparing small streams in concurrent WV and UAV images; Supporting and validating supraglacial hydrologic feature mapping |
| | 1030010045092500 | 2.0 m | 18 July 2015 | |
| | 1030010047C39F00 | 2.0 m | 18 July 2015 | |
| | 1030010046A5F200 | 0.5 m & 2.0 m | 24 July 2015 | |
| | 10300100470EB600 | 0.5 m & 2.0 m | 24 July 2015 | |
| WorldView-3 satellite imagery | 104001000EB35500 | 0.5 m & 2.0 m | 21 July 2015 | |
| UAV imagery | - | 0.25 m | 20-22 July 2015 | |
| MODIS albedo | MYD10A1 daily product | 500 m | 20-21 July 2015 | Validate or drive climate/SMB models |
| SETSM DEM | ArcticDEM_15_39_5_2 | 2.0 m | 30 August 2011 | Assist catchment boundary delineation |
| SPIRIT DEM | DRONNING_INGRID_080627 | 40.0 m | 27 June 2008 | |

237

238

239 2.1 Satellite image and digital elevation model (DEM) products:

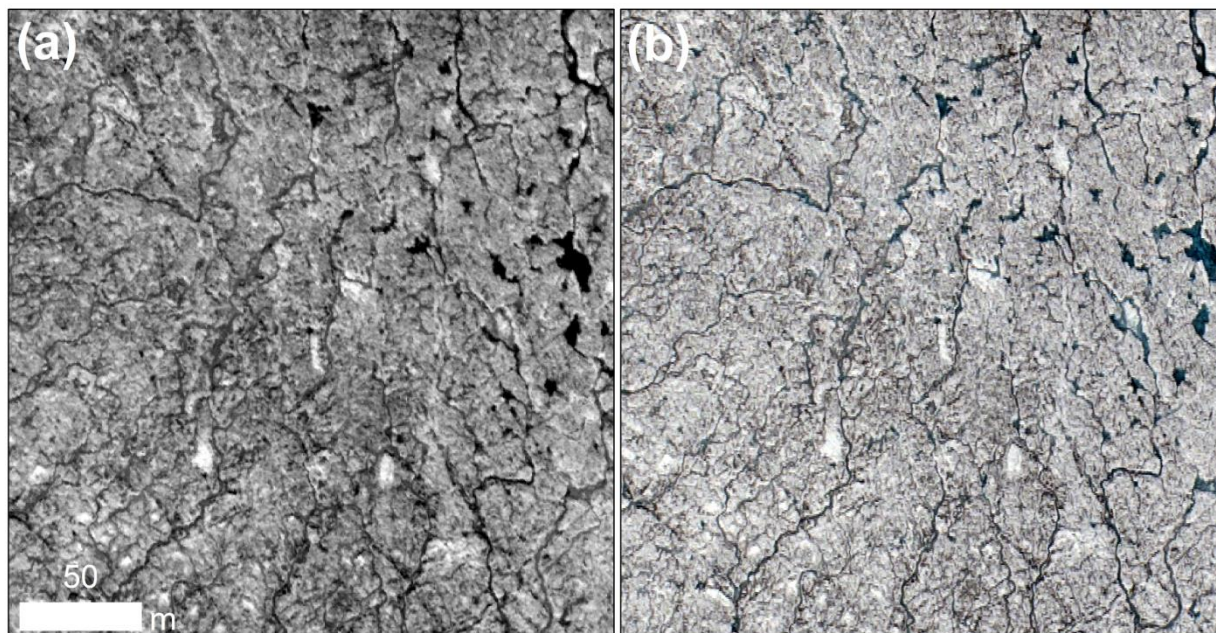
240 A total of eight 0.5 m panchromatic images from the WorldView-1 and WorldView-2 satellites
241 were used to construct stereo-photogrammetric DEMs and map supraglacial streams, rivers,
242 moulins, and channel heads (initiation of incision) within the Rio Behar catchment. Three 2.0 m
243 multispectral images from WorldView-2 were used to map snow areas. Archived WorldView-1
244 images were used to map the IDCs of two previously published field studies (5, 6). All
245 WorldView satellite images were acquired through the Polar Geospatial Center (PGC) and were
246 orthorectified using the satellite positioning model (also known as the rational function model)
247 and projected into a polar stereographic coordinate system using PGC scripts
248 (https://github.com/PolarGeospatialCenter/imagery_utils). One scene of Stereo-
249 Photogrammetric Digital Elevation/Surface Models (SETSM, spatial resolution 2.0 m) released
250 by the PGC and the Byrd Polar Research Center Glacier Dynamics Group
251 (<http://www.pgc.umn.edu/elevation/stereo>) and one scene of SPOT 5 stereoscopic survey of
252 Polar Ice: Reference Images and Topographies (SPIRIT, spatial resolution 40 m) DEM released by
253 the International Polar Year (IPY) project
254 (<https://theia.cnes.fr/rocket/#/search?collection=spirit>) were also used to aid extraction and
255 evaluation of the Rio Behar catchment boundary.

256

257 2.2. Unmanned Aerial Vehicle (UAV):

258 To supplement and verify the WorldView satellite data acquired during the field experiment, a
259 fixed-wing UAV as described by Ryan *et al.* (4) acquired aerial RGB camera imagery over Rio
260 Behar catchment from 20-22 July as part of three successive surveys beginning at 12:04 UTC on
261 20 July 2015 and finishing at 18:45 UTC on 22 July 2015. This UAV has a wingspan of 2.12 m and
262 is powered by eight custom-made (14.4V) lithium-ion battery packs. Propulsion is provided by a
263 715W brushless electric motor which turns a 12 x 8 inch foldable propeller. Autonomous
264 control is provided by a Pixhawk autopilot designed by the PX4 open-hardware project and
265 manufactured by 3D Robotics (<https://pixhawk.org/modules/pixhawk>). The Pixhawk utilizes a
266 single-frequency GPS, gyroscope, accelerometer, magnetometer and barometer for flight
267 control. With this configuration, the UAV has a cruising speed of 60 km/hour and endurance of
268 1.5 hours, allowing the UAV to comfortably fly survey missions of up to 80 km. A total of 3,795
269 overlapping images at an altitude of 1,000 m above the ice surface were obtained over a 102
270 km² area extending beyond the Rio Behar catchment boundaries. These camera images were
271 processed with Agisoft PhotoScan Pro (8) and an ortho-mosaic with a 30 cm ground sampling
272 distance (GSD). A digital elevation model with a 1 m GSD was also generated but not used in
273 the study. Georeferencing accuracy of orthorectified products was aided by installation of four
274 GPS surveyed (single-frequency, accurate to 3 m horizontally and up to 15 m vertically) red

275 tarpaulins at four distributed locations around Rio Behar catchment (position 1: 67.0486°N,
276 -49.0208°W, 1207.5 m; position 2: 67.0610°N, -48.9025°W, 1289.5 m; position 3: 67.0315°N,
277 -48.9582°W, 1248.1 m; position 4: 67.0214°N, -48.9281°W, 1271.7 m) for use as ground control
278 points (GCP, red plus symbols, **Figure 1**). The primary utility of these higher-resolution data was
279 to supplement WorldView satellite data for the purpose of visually identifying small areas of
280 confirmed and potential catchment leakage (i.e. internal subcatchments) draining to small
281 internal moulins, and crevasse fields. Comparison of 0.25 m UAV imagery with panchromatic
282 WorldView-1 imagery confirms good detection of supraglacial streams, even down to sub-meter
283 widths (**Figure S3**).



284
285 **Figure S3. WV1 and UAV discrimination of small supraglacial streams. Concurrent (a) 0.5 m**
286 **panchromatic WorldView-3 (WV3) image (catalog ID: 104001000EB35500) and (b) 0.25 m UAV image**
287 **acquired on 21 July 2015 for a headwater area of the Rio Behar catchment, showing that the same**
288 **small streams can be discerned in both WV3 and UAV imagery. Image center locations are 67.079 N,**
289 **48.916 W and image sizes are 250 × 250 m. WV3 imagery Copyright 2015 DigitalGlobe, Inc.**

290

291 **3. Remote sensing data processing**

292 High resolution satellite and UAV mappings of Rio Behar catchment bookend and overlap with
293 the ADCP river discharge and ice ablation measurements. These remotely sensed geospatial
294 data were post-processed to produce precise maps of Rio Behar catchment boundaries,
295 supraglacial drainage patterns, small internal moulins (signifying leakage), and snow cover as
296 follows:

297 3.1 processing of stereo-photogrammetric DEMs from WorldView satellite imagery:

298 High resolution stereo-photogrammetric DEMs were derived from along-track stereo
299 WorldView panchromatic satellite imagery using the open source Ames Stereo Pipeline (ASP)
300 toolkit methods (9, 10). Images were resampled to 1 m resolution before processing to reduce
301 computational time needed for DEM production. The output of ASP consists of point clouds
302 that are spatially filtered to produce 3 m posting DEMs. Horizontal positioning accuracy is
303 typically better than 5 m. In this study, the derived DEMs were used to extract Rio Behar
304 catchment boundaries (**Figure 1**) following hydrologic analysis as follows: 1) only the
305 topographic depression at the catchment outlet was used as meltwater sink and a partially
306 filled DEM raster was created (11); 2) flow direction was identified by using this partially filled
307 DEM; 3) the catchment boundary was extracted using the Basin function in ArcGIS software. A
308 total of five digital elevation models (DEMs) constructed for Rio Behar catchment over the
309 period 2008-2015 confirm overall long-term stability of the topographic boundaries of this
310 particular IDC with interannual area variations of just 1.9 – 3.3 % (**Figure 1**).

311 3.2 Image processing of WorldView satellite imagery:

312 Supraglacial stream/river networks were delineated from the 0.5 m panchromatic 18 July 2015
313 WorldView-1 image, following the method of *Yang et al.* (12). Variable ice surface backgrounds
314 were first eliminated by spectral analysis and non-local means denoising; small supraglacial
315 rivers were enhanced by Gabor filtering; and continuous supraglacial river networks were
316 obtained by path opening (12). Next, a global threshold of 120 was used to classify the original
317 WorldView-1 image (gray value ranges from 0 to 503) to extract supraglacial lakes. Finally, a
318 meltwater mask raster was generated by combining the described river and lake binary masks.

319 In total, some 3380.6 km of supraglacial stream/river lengths were mapped in the optimal Rio
320 Behar catchment boundary, yielding a drainage density of 53.6 km/km². The mean channel
321 width was 2.4 ± 1.5 m and surface meltwater covered 8.2 % of the ice surface. Two WorldView-
322 1 panchromatic images (18 July 2015 and 24 July 2015) and repeated UAV sorties (20-22 July
323 2015) confirmed that the supraglacial river network and four small, interconnected supraglacial
324 lakes (**Figure 1**) remained intact and actively flowing throughout the 20-23 July 2015 field
325 experiment.

326 Uppermost headwater channel heads (initiation points) of first-order tributaries were mapped
327 visually from the 0.5 m panchromatic 18 July 2015 WorldView-1 image (catalog ID:
328 102001004202CD00, see **Table S2**), for both Rio Behar catchment headwaters (total 839
329 mapped, termed “inner” channel heads, **Figure 1**) and adjacent catchments (total 780 mapped,
330 termed “outer” channel heads, **Figure 1**). Connecting these inner and outer channel heads
331 yields minimum and maximum plausible extents of the Rio Behar catchment, respectively. In

332 addition, 49 confirmed and 24 possible internal moulins and/or moulin complexes were
333 manually identified from the 18 July WorldView-1 image cross-checked by the 20-22 July 2015
334 UAV camera images and the 24 July 2015 WorldView-1 panchromatic image.

335 Connecting the 780 outer channel heads for the adjacent catchment provides the maximum
336 plausible catchment extent (area 69.1 km^2 , all pixels lying outside this boundary confidently do
337 not flow to the Rio Behar terminal moulin), whereas connecting the 839 inner channel heads
338 for the Rio Behar catchment provides a conservative minimum plausible extent (51.4 km^2 , with
339 all pixels inside this boundary and lying outside of the small internally drained subareas
340 confidently flowing to the terminal moulin) for the Rio Behar IDC during the field experiment.
341 An intermediate, “optimal” catchment boundary was derived using the 18 July 2015
342 WorldView-1 stereo-photogrammetric DEM, adjusted for small areas of stream “breaching”
343 (piracy) across topographic ice divides (12, 13) and small areas subareas of internal moulin
344 drainage (**Figure 1**). Visual inspection of WorldView and UAV imagery along this topographic
345 boundary, revealed small areas undoubtedly draining away from Rio Behar catchment (but
346 included inside its topographic divide) owing to stream channel breaching of the topographic
347 divide. These small areas (totaling 2.7 km^2) were manually eliminated from the 18 July 2015
348 DEM boundary. Similarly, small areas undoubtedly draining into the Rio Behar catchment (but
349 outside the topographic divide) were manually added (totaling 0.8 km^2). Finally, small
350 subcatchments flowing to internal moulins (total area 1.6 km^2) and crevasse fields (4.1 km^2)
351 were eliminated. Crevasse areas were determined visually in WorldView and UAV imagery
352 and eliminated from our lower-bound estimate of watershed area, so their potential storage
353 falls within the central and lower bound of modeled runoff uncertainty in **Figure 3** and **Figure**
354 **7a**. We submit that the resultant optimal catchment delineation (area 63.1 km^2) combines the
355 strengths of high-resolution remote sensing of the supraglacial stream/river drainage pattern
356 with topographic divides from a simultaneous WorldView stereo-photogrammetric DEM.

357 Small subcatchments draining to the “confirmed” and “possible” internal moulins were
358 identified in the WorldView and UAV imagery and also removed to demarcate the conservative
359 Rio Behar catchment area estimate (**Figure 1**). To do this, subcatchments draining into
360 confirmed and potential internal moulins were labeled with unique IDs in ArcGIS. These labeled
361 river networks were then used as seed regions for region expansion, by applying the path
362 distance allocation function in ArcGIS to calculate the nearest source for each seed river
363 network based on the minimum cumulative cost over the cost surface as per Yang and Smith
364 (7). The resultant allocation map partitioned Rio Behar catchment into three different
365 categories, with two categories, subcatchments draining into confirmed (total area 1.6 km^2)
366 and potential (area 0.7 km^2) internal moulins eliminated to yield the conservative catchment
367 boundary (area 51.4 km^2).

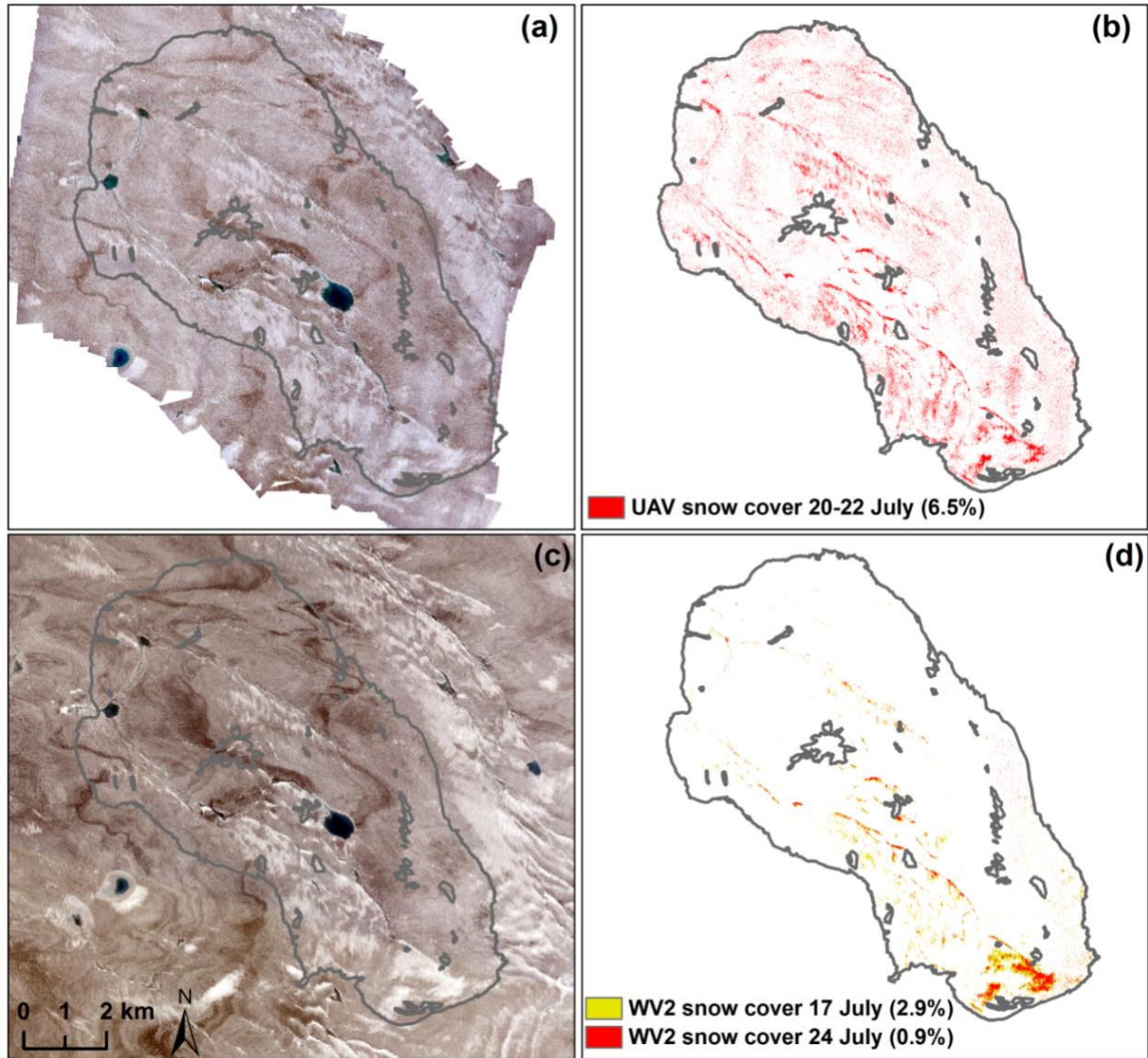
368 3.3 Estimation of supraglacial lake volumes:

369 Four supraglacial lakes are integrated into the stream/river network of Rio Behar catchment
370 (**Figure 1**). To investigate whether water impoundment in these lakes could explain the
371 observed deficit between ADCP and climate/SMB model estimates of R , we used multi-spectral
372 WorldView-2 images acquired on 18 July 2015 (catalog ID: 1030010045092500 and
373 1030010047C39F00) and 24 July 2015 (catalog ID: 1030010046A5F200) to calculate their
374 respective volume changes over the time of our ADCP field experiment. We used the method
375 of Pope *et al.* (14), which entails building a DEM of the supraglacial lake basins when they are
376 empty, then intersecting the DEM with a remotely sensed lake mask when the basin is occupied
377 with water. DEM elevations within the shorelines of the lake mask are then summed to obtain
378 lake volume. In the 18 July 2015 WV DEM, all four depressions are partially occupied by lakes
379 and therefore could not be used as the base DEM. We built a new DEM from the preceding fall,
380 using a stereo WorldView-1 image pair acquired on 29 October 2014 (catalog ID:
381 1020010034334B00 and 10200100354A5700). In this post-melt stereo image pair, all four lake
382 depressions are empty and were used to estimate supraglacial lake volumes the following year
383 (topographic depressions are largely controlled by bedrock (11) and are therefore deemed
384 stable over the period October 2014 to July 2015). We extracted lake masks using a band ratio
385 of Band 2 (blue, 450-510 nm) to Band 8 (near infrared, 860-1040 nm), with a global ratio
386 threshold set to 1.25 following the method of Smith *et al.* (13). The two resultant lake masks
387 were used to clip DEM-modeled topographic depressions and the topographic depression
388 volumes located in the lake masks were calculated as the lake volumes.

389 During 18-24 July 2015, all four supraglacial lakes shrank, for a total volume reduction of $2.2 \pm$
390 $4.3 \times 10^{-4} \text{ km}^3$. Divided over by our optimal catchment area, this lake volume change equals to
391 $3.5 \pm 6.8 \text{ mm}$ runoff in the entire Rio Behar catchment, with the uncertainty estimate computed
392 as one standard deviation from the mean in lake elevation along the shoreline as per Pope *et al.*
393 (14). Interpolating linearly between the two satellite acquisition dates, this corresponds to a
394 water release of $0.02 \pm 0.05 \text{ mm/hour}$, which is $3.2 \pm 6.3 \%$ of the average ADCP hourly
395 discharge (0.75 mm/hour). We therefore conclude that water impoundment in these four
396 supraglacial lakes cannot explain the observed runoff deficit between ADCP measurements and
397 climate/SMB models. Instead, they released a minor amount ($<10 \%$) of meltwater to the
398 observed ADCP river discharge, lending further conservatism to our finding of climate/SMB
399 model overestimation of R .

400 3.4 Snow classification:

401 The images acquired during our field experiment were classified to determine the fractional
402 area of snow cover during the time of our ADCP measurements. These images consisted of our
403 UAV camera image mosaic (20-22 July 2015, RGB bands, spatial resolution 0.3 m) and three



404

405 **Figure S4: Snow cover classifications derived from a UAV image mosaic acquired 20-22 July 2015,**
 406 **(RGB bands, spatial resolution 0.3 m) and two WorldView-2 multi-spectral images acquired 17 and 24**
 407 **July 2015 (catalog IDs: 1030010046354000 and 1030010046A5F200, 8 bands, 2.0 m): (a) UAV image**
 408 **mosaic, (b) UAV snow classification, (c) 24 July WorldView-2 multi-spectral image, (d) snow**
 409 **classifications of 17 July and 24 July WorldView-2 images. Viewed collectively, these maps confirm**
 410 **that Rio Behar catchment was largely snow-free during the field experiment, confirming climate/SMB**
 411 **model assumptions of bare-ice conditions and ruling out temporary meltwater retention in seasonal**
 412 **snow/firn as an explanation for the observed overestimation of modeled runoff R . WorldView-2**
 413 **imagery Copyright 2015 DigitalGlobe, Inc.**

414 WorldView-2 multi-spectral images (one from 17 July 2015 and two from 24 July 2015, 8 bands,
 415 2.0 m resolution). First, a supervised k-Nearest Neighbors (k-NN) algorithm from the scikit-
 416 learn Python module (15) was used to classify the UAV image. Next, a supervised maximum

417 likelihood algorithm from the ArcGIS software was used to classify both the UAV and WV2
418 images. The two classification algorithms were trained by manually digitizing areas of snow,
419 bare ice and surface water. Once trained, pixels were classified into one of the three classes
420 (snow, ice or water) and three snow classification maps were obtained (**Figure S4**). The
421 resultant snow cover fractions are 6.5% in the 20-22 July UAV mosaic, and 2.9% and 0.9% in the
422 17 and 24 July WV2 images, respectively. This difference between the two sensors is attributed
423 to the higher spatial resolution of the UAV data (0.25 m, versus 2.0 m for multi-spectral WV2)
424 allowing better mapping of small snow patches, the use of near-infrared channels on WV2 (UAV
425 is visible-spectrum only), or both. For the purpose of this study, both UAV and WorldView-2
426 snow classifications indicate that snow cover was largely absent from the Rio Behar catchment
427 during the time of our field experiment. This confirms the climate/SMB model assumptions of
428 bare-ice conditions at the time of our field experiment, and largely rules out meltwater
429 retention in seasonal snow as a significant physical mechanism for the observed discrepancy
430 between observed and climate/SMB modeled runoff R .

431

432

433 **4. Supraglacial hydrograph analysis**

434 The 72-hour ADCP time series of supraglacial river discharge Q comprises the core field dataset
435 of this study and was processed using traditional hydrograph analysis methods for terrestrial
436 watershed hydrology. These steps include quantification of hydrograph recession flow,
437 hydrograph separation, derivation of runoff coefficients/correction factors, derivation of the
438 Unit Hydrograph (UH) for Rio Behar catchment, and using the UH to calibrate a Synthetic Unit
439 Hydrograph (SUH) for broader extension across the southwest GrIS ablation zone, as follows:

440 4.1 Recession flow:

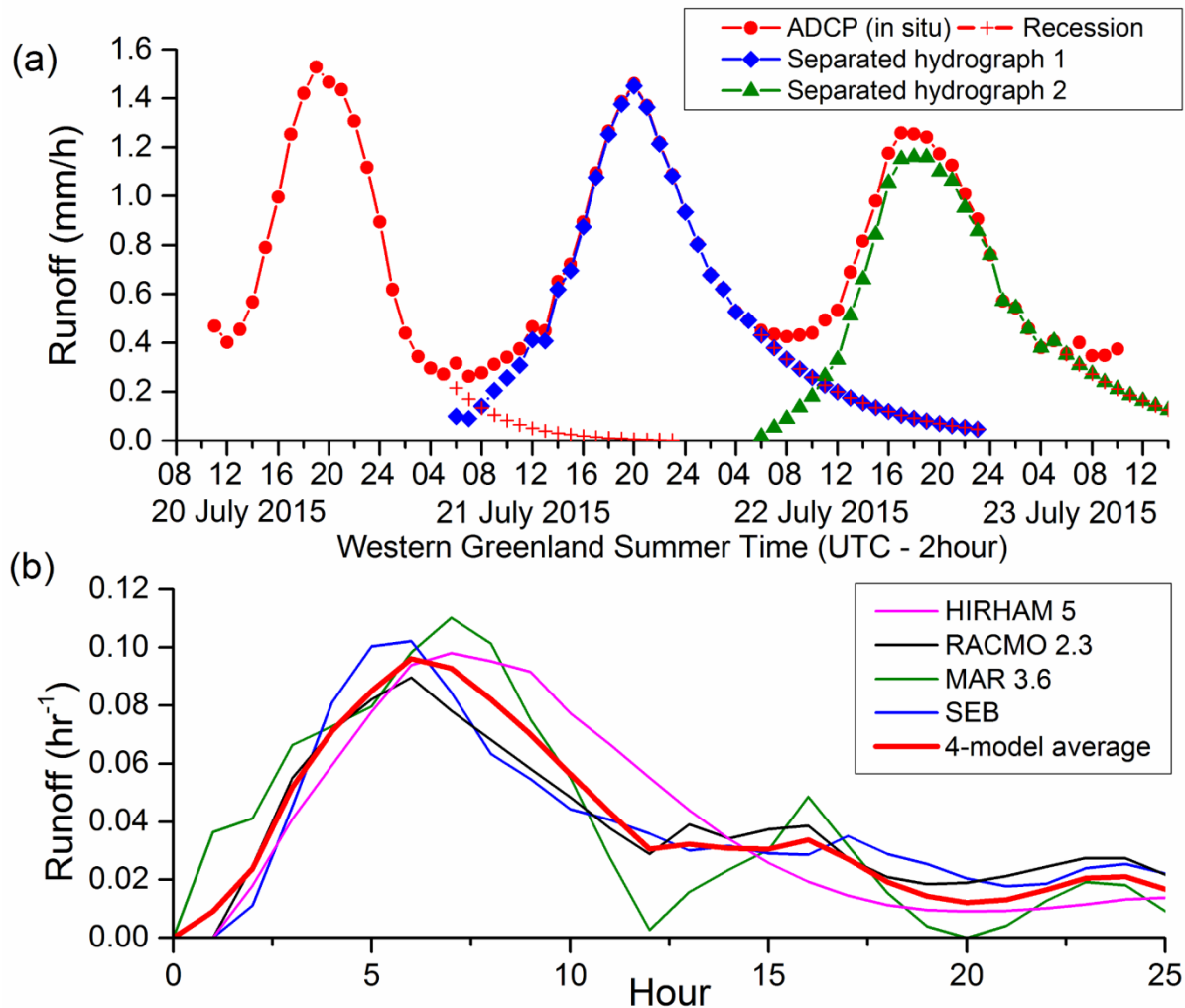
441 Of particular benefit to our hydrograph analysis was a nightly cessation of melt production from
442 approximately midnight (0000) to 0600 local time each day, and a lack of any precipitation
443 during the field experiment. The first yielded an unambiguous nightly period of hydrograph
444 recession (i.e. an interval of receding runoff from the catchment during which no new
445 climatological meltwater production occurred in the catchment). The second allowed all
446 variations in the discharge hydrograph Q to be attributed solely to the diurnal cycle in
447 climate/SMB modeled melt production M , without the added complication of rain-on-snow
448 events. Hydrograph recessions were observed nightly from approximately 0000 to 0600,
449 enabling quantification of exponential-decay hydrograph recession constants (k) and separation
450 of recession flow from falling limbs of the direct (observed) hydrograph. For the four models
451 supplying melt simulations M (i.e. all models except MERRA-2) we observed positive M values

452 (i.e. a “melt hyetograph”) persisting for approximately 18 hours each day (from 0600 to 0000),
453 with cessation of melt production for approximately 6 hours each night (from 0000 to 0600).
454 During this nightly melt shutdown, supraglacial discharge (i.e. the direct hydrograph Q) receded
455 but did not terminate throughout the night. This signifies that 18 hours of melting on Rio Behar
456 catchment yields measurable runoff for at least 24 hours, and that hydrograph recession
457 constants must be obtained and used to separate direct vs. recession flow from each diurnal
458 cycle. We defined a 6 hour flow recession period from 0000 to 0600 nightly, for fitting with the
459 customary (16) exponential decay recession equation, $Q = Q_0 k^t$ (with Q_0 being the discharge at
460 recession initiation, Q the discharge at t hours later, and k the exponential-decay recession
461 constant). This fitting yielded k values of 0.79, 0.88, and 0.88 for July 21, 22, and 23,
462 respectively, then averaged to yield $k=0.85$ (averaging over multiple recessions is suitable for
463 characterizing mean recession behavior (17, 18)) for Rio Behar catchment over the period 21-23
464 July 2015. This is slightly lower than typical terrestrial catchment k values (>0.90) implying a
465 somewhat slower, “flatter” recession process but one not dissimilar from terrestrial catchments
466 (16, 19).

467 4.2 Hydrograph separation:

468 For each diurnal cycle, the described recession fitting equations were used to separate
469 recession flow from direct flow. A starting assumption is that for a single hour of melt
470 production, that hour may contribute to observed supraglacial river discharge for up to 24
471 hours. As such, residual meltwater produced during a typical 18 hour “melt-production day”
472 (i.e. from hour 0600 to 0000 local time) may arrive at the catchment’s terminal moulin up to 42
473 hours later (i.e. from 0600 to 0000 of the following day). It is possible that recession flow
474 persists longer than 42 hours, but will likely be very small (<0.05 mm/h or $<0.2\%$ of the total
475 melt in one day) so a further time extension is not performed in this study. Because recession
476 flow extends into each following day, we derive two complete diurnal cycles of separated
477 hydrographs from the 72 hour record (**Figure S5**). The final outcome is thus two independent,
478 separated 42 hour hydrographs, obtained by subtracting recession discharge from the previous
479 day and retaining recession discharge into the following day. These two complete diurnal cycles
480 of separated hydrograph flow extend from 0600 July 21 to 0000 July 23 (termed July 21
481 hydrograph), and from 0600 July 22 to 0000 on July 24 (termed July 22 hydrograph), as derived
482 from hydrograph separation over the period 0000 July 21 to 0600 July 23 (**Figure S5**).

483



484

485 **Figure S5: Rio Behar hydrograph separation and model-tuned unit hydrographs (UH) relating**
 486 **climate/SMB modeled melt to runoff delivered to the Rio Behar terminal moulin. (a)**
 487 **Hydrograph separation, yielding two separated diurnal hydrographs on 21/22 July and 22/23**
 488 **July 2015. (b) Unit Hydrograph (UH) routing models calibrated to corrected climate/SMB melt**
 489 **outputs (M' , see SI section 4.3) of the HIRHAM 5, RACMO 2.3, MAR 3.6, and SEB climate/SMB**
 490 **models. No UH is available for the MERRA-2 model because melt M is not an output of**
 491 **MERRA-2. The 4-model average (thick red line in Figure S5b) is used to generate theoretical 1**
 492 **cm peak discharges in Figure 4b.**

493

494 4.3 Runoff coefficients (correction factors) relating modeled M to observed R : Following
 495 derivation of these two separated hydrographs, runoff coefficients (c) may be calculated for
 496 each climate/SMB model as $c = Q/M$, where M is total “daily” (i.e. total 18 hour) catchment
 497 surface melt M as simulated by models, and Q the corresponding separated (i.e. total 42 hour)

498 associated catchment discharge. Note that in this particular study the derived coefficients
 499 reflect inferred model over-prediction of R , so are more appropriately treated as empirical
 500 correction factors for model output rather than quantification of physical runoff losses (e.g. to
 501 infiltration, retention, missed crevasses etc.). The resultant c values range from 0.53 to 0.78,
 502 indicating that 53-78% of the surface meltwater M simulated by models was measured as
 503 physical runoff departing the ice surface to the Rio Behar catchment terminal moulin. As a
 504 practical step, these model-specific coefficients may be multiplied with model outputs of M to
 505 yield a lower, empirically corrected estimate of runoff departing the ice surface. To
 506 differentiate this derived quantity from the modeled variable runoff R we propose the term
 507 “effective melt” (M') for this adjusted value of M , that is $M' = c * M$. These model-tuned runoff
 508 coefficients / correction factors are supplied in **Table S3** and used as forcing data for the
 509 instantaneous area-integrated runoff and SUH-routed computations of **Figure 5** and **Figure S11**.
 510 Generation of runoff coefficients / correction factors and SUH parameters is not possible for
 511 MERRA-2 because meltwater production M is not an output of this model. For ablation
 512 surfaces possessing physical conditions like those sampled at Rio Behar catchment, these
 513 coefficients may be multiplied by M to yield alternate, lower estimates of R in addition to
 514 standard model output. Pending further study, they cannot be confidently extended to non-
 515 similar surfaces or other times of the year. Future collection of supraglacial discharge
 516 measurements across a range of ice surface type is needed to develop runoff coefficients /
 517 correction factors and SUH parameters for other surfaces (in particular catchments containing
 518 firn) and earlier/later times of year.

519 **Table S3: Rio Behar catchment runoff coefficients/correction factors and SUH parameters**

| | Runoff coefficients / correction factors | | | Synthetic unit hydrograph (SUH) parameters* | | | | |
|-----------|--|---------|---------|---|---------------------------|-------|-------|-----------|
| | July 21 | July 22 | Average | t_p (hr) | h_p (hr ⁻¹) | C_p | C_t | Gamma m |
| MAR 3.6 | 0.73 | 0.64 | 0.69 | 6.5 | 0.11 | 0.72 | 1.61 | 4.6 |
| SEB | 0.78 | 0.72 | 0.75 | 5.5 | 0.10 | 0.56 | 1.36 | 3.1 |
| RACMO 2.3 | 0.62 | 0.67 | 0.65 | 5.5 | 0.09 | 0.49 | 1.36 | 2.1 |
| HIRHAM 5 | 0.55 | 0.53 | 0.54 | 6.5 | 0.10 | 0.64 | 1.61 | 3.3 |
| MERRA-2 | n/a | n/a | n/a | n/a | n/a | n/a | n/a | n/a |

520

521 * To apply SUH routing to a larger area of the ablating Greenland ice sheet surface, the above
 522 values for C_p , C_t and m calibrated for Rio Behar catchment were applied to 799 surrounding IDCs
 523 during the study period. Their catchment parameters t_p and h_p , however, were remotely sensed
 524 for each individual IDC. For description of runoff coefficients / correction factors see Section
 525 4.3. For descriptions of SUH parameters see Sections 5.1 and 5.2.

526 4.4 Unit Hydrograph (UH) derivation:

527 The unit hydrograph (UH) is a transfer function that is widely used for modeling catchment
528 runoff response to rainfall events for some unit duration and unit depth of effective water input
529 (i.e. the “excess” precipitation remaining and available to run-off following interception and
530 infiltration, analogous to our M') applied uniformly across the catchment(19). A “one hour UH”,
531 for example, represents the characteristic response of a given catchment to a unit depth of
532 effective water input applied at a constant rate for one hour. To derive the one hour UH for Rio
533 Behar catchment for each climate/SMB model, we used effective melt (M') and observed runoff
534 (Q) as input/output to derive the one hour UH transfer function (i.e., $Q = M' * UH$) using the
535 traditional optimization (20) as follows:

$$Q_{N \times 1} = M'_{N \times J} U_{J \times 1}$$

536 where $Q_n = \sum_{k=1}^K M'_k U_{n-k+1}$, N is total number of discharge measurements ($N = 42$), K is the
537 total number of hours of effective melt ($K = 18$), J is the number of hours in unit hydrograph (J
538 $= N - M + 1$). Therefore, the duration of the derived one hour UH is 25 hours. Examination of
539 the resultant one hour UH's shows that for one hour of M' across the Rio Behar catchment, the
540 associated time to peak (t_p) for that hour is 5.5-6.5 hours, depending on the model (**Table S3**).
541 The corresponding peak discharge (h_p) is 0.09 to 0.11 hr^{-1} , signifying that 9-11% of the input of
542 one hour of M' contributes to peak discharge. Because recession flow extends into the
543 following day, we used the aforementioned two complete diurnal cycles of separated
544 hydrographs to calculate these UH parameters t_p and h_p for both days for each model, and also
545 average them for presentation in **Table S3**.

546

547 **5. Extension of Synthetic Unit Hydrograph (SUH) model to 799 internally drained catchments** 548 **(IDCs)**

549 To isolate the influence of surface drainage pattern (i.e. IDCs) upon the timing and volume of
550 surface meltwater delivery to moulins across a larger area of the GrIS ablation zone, we apply a
551 simple “lumped” morphometric routing scheme, the Snyder Synthetic Unit Hydrograph (SUH)
552 model (21) and a Gamma function (22) to a previously published (7) broad-scale (13,563 km^2)
553 map of 799 remotely sensed IDCs (including Rio Behar catchment) have confirmed stream/river
554 networks. This requires fitting the observed UH calibrated at Rio Behar to other IDCs, taking
555 into account their differing shapes and areas. Note that this extension assumes that ice surface
556 properties were similar for all 799 IDCs as Rio Behar during the time of our field experiment. To
557 help justify this, we limit the time of our broader SUH application to the time of our field
558 experiment (21 July 2015).

559 5.1 Derivation of Synthetic Unit Hydrograph (SUH) model parameters for 799 IDCs:

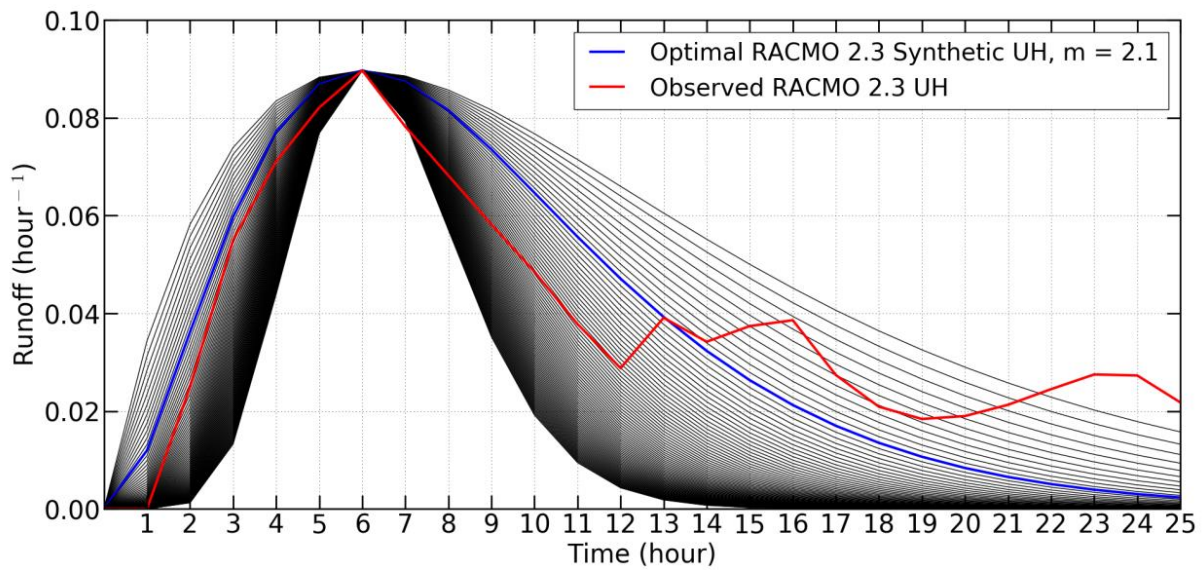
560 A distinct advantage of the SUH method is its non-reliance on digital elevation models, thus
561 avoiding known challenges with the use of DEMs for modeling supraglacial hydrology, notably
562 selection of a user-specified parameter used to fill noise and/or true topographic depressions in
563 the ice surface DEM (23, 24), as well as breaching of headwater stream channels across
564 topographic ice divides (13). Rather than using DEMs, the SUH approach reduces the influence
565 of IDC morphometry to just three simple parameters, the total catchment area (A , in km^2), the
566 catchment main-stem stream length (L , in km), and an elongation proxy, calculated as the
567 distance from the catchment outlet (here, the terminal moulin) to the point on the main
568 channel nearest to the catchment centroid (L_c , in km). The Snyder SUH uses these watershed
569 metrics to estimate the aforementioned UH summary parameters t_p (time-to-peak, in hours)
570 and h_p (peak discharge, in hr^{-1}) for ungauged watersheds as $t_p = C_t(L_c)^{0.3}$, and $h_p = C_p/t_p$. Peak
571 discharge (Q_{pk}) at the catchment outlet (i.e. moulin) is $Q_{pk} = A * M' * h_p$. With unit conversion the
572 formula becomes $Q_{pk} = 0.28 * M' * h_p$, with Q_{pk} in $\text{m}^3 \text{s}^{-1}$, A in km^2 , and M' in hr^{-1} . We used
573 ArcGIS to extract A , L , and L_c for 799 internally drained catchments previously mapped across
574 the southwest GrIS from a high-contrast 19 August 2013 panchromatic Landsat-8 image (7).
575 Note that C_p and C_t are dimensionless coefficients which we calibrate at Rio Behar catchment
576 using the field-calibrated UH, and $L=13.8$ km, and $L_c=7.6$ km from the Yang and Smith dataset.
577 A complete set of model-tuned estimates for C_p and C_t are presented in **Table S3**, with an
578 average value of $C_p = 0.60$ and $C_t = 1.49$. These ice-calibrated values fall within the normal
579 range of terrestrial values (0.56-0.69) for C_p and are lower than terrestrial values (1.8-2.2) for C_t
580 (21), however, at least two other studies report lower values of C_t in terrestrial watersheds, e.g.
581 0.3 to 0.7 (25), 0.4-2.4 (26), signifying that our low on-ice values do have precedent on land.
582 This lower value of C_t reduces t_p and increases h_p , indicating that Rio Behar catchment has a
583 flashy response to meltwater input relative to most terrestrial catchments.

584 The SUH coefficients C_p and C_t calibrated at Rio Behar catchment characterize the overall bulk
585 properties of water drainage efficiency off the ablating ice surface, and are held constant in the
586 present study. To examine the role of IDC-specific morphometry differences (i.e. A , L , and L_c)
587 on the timing and volume of runoff departing each of the 799 IDCs, we apply the SUH to them
588 using the simplest theoretical case (assuming a spatially uniform depth of 1 cm meltwater
589 runoff over a duration of 1 hour is allowed to drain from each IDC), and using climate/SMB
590 model output (M') to drive the SUH. For the simple case, we map the theoretical time to peak
591 (t_p) and peak moulin discharge (Q_{pk}) responses of a 1 hour uniform release of 1 cm of M' for all
592 799 IDCs (**Figure 4**). Note considerable uncertainties in small catchment boundaries at low
593 elevations (7) causing L_c values to be underestimated, making h_p values incorrectly large. This
594 explains why some small catchments at low elevations yield anomalously large peak discharge
595 (**Figure 4b**, also **Figure 5** and **Figure S11**). Because a uniform melt depth is assumed

596 everywhere, **Figure 4** isolates the pure effect of catchment morphometry on t_p and Q_{pk}
 597 independent of spatial and/or elevational gradients in meltwater production (i.e. surface mass
 598 balance).

599 5.2 Generation of model-driven synthetic hydrographs for 799 IDCs:

600 To incorporate the impact of elevational and spatially varying gradients in melt production and
 601 surface mass balance, we used climate/SMB model outputs of M' from MAR3.6, RACMO2.3,
 602 and HIRHAM5 to drive the SUH model (**Figure 5, Figure S11**). Because point-SEB is a non-
 603 gridded model driven by the KAN_M AWS, and MERRA-2 does not supply M), only MAR,
 604 RACMO, and HIRHAM could be deployed in this way.



605 **Figure S6. Optimal model-specific synthetic unit hydrographs (SUHs) for Rio Behar catchment**
 606 **may be approximated using Gamma functions, by varying the Gamma shape coefficient m to**
 607 **optimally fit each climate/SMB model using Nash-Sutcliffe model efficiency (see Equation 2).**
 608 **For illustration, the observed RACMO 2.3 UH appears in red and its corresponding**
 609 **approximated SUH in blue (shape coefficient $m=2.1$).**

611 To produce **Figure 4, Figure 5, and Figure S11** We built a SUH curve for each IDC based on
 612 Snyder time-to-peak (t_p), peak discharge (h_p), and a Gamma function:

613
$$\frac{q}{h_p} = e^m \left[\frac{t}{t_p} \right] \left[e^{\left(-m \left(\frac{t}{t_p} \right) \right)} \right] \quad (1)$$

614 where q is the SUH discharge at time t , and m is the Gamma equation shape factor (22). The
 615 parameter m controls the shape of Gamma function and must be determined empirically.
 616 Recall that the SUH parameters t_p and h_p are different for each IDC, whereas C_p , C_t and m are

617 empirically calibrated from our Rio Behar field experiment and assumed to be constant in this
 618 study. To determine model specific m values, we tested different m values using Nash-Sutcliffe
 619 model efficiency (Equation (2)) for our model-specific Rio Behar Unit Hydrographs (**Figure S5b**),
 620 to obtain the optimal value of m (e.g. for RACMO2.3, **Figure S6**). These model-optimized m
 621 values are supplied in **Table S3**. To compute the theoretical peak moulin discharges presented
 622 in **Figure 4b**, an optimal value of m of 2.5 was obtained from the 4-model average UH
 623 (including SEB, thick red line **Figure S5b**).

$$624 \quad E = 1 - \frac{\sum_{t=1}^T (Q_o^t - Q_m^t)^2}{\sum_{t=1}^T (Q_o^t - \bar{Q}_o)^2} \quad (2)$$

625 The SUH curve derived for each IDC estimates how meltwater production (more specifically, the
 626 corrected meltwater production M') across each IDC is released to its terminal moulin over
 627 time. Unlike the instantaneous area-integration method, climate/SMB model output is
 628 distributed over time. For each IDC, convolution of SUH with hourly model outputs of M' yields
 629 a discharge hydrograph at the terminal moulin.

630 We used the function $Q = M' * \text{SUH}$ to calculate discharges at IDC outlets, where M' is effective
 631 melt, SUH is the Synthetic UH curve obtained above, and $*$ is the convolution operator. As
 632 such, input melt for each IDC is temporally distributed over time and the discharge hydrograph
 633 computed for the IDC terminal moulin. Note that this approach assumes all runoff is routed to
 634 the terminal moulin with no further losses of water (beyond any losses already captured by the
 635 calculation $c \times M = M'$).

636 To compare the difference between SUH-routed runoff and instantaneous (non-routed)
 637 approaches, we used the above procedure to model moulin discharges for all 799 IDCs at 1400
 638 local western Greenland time on 21 July 2015 (a peak melt production time, **Figure 5**) and 10
 639 hours later at 2400 local time on 21 July 2015 (**Figure S11**). The top row in each figure shows
 640 climate/SMB output of M' , the middle row instantaneous area-integrated runoff, and the
 641 bottom row SUH-routed runoff. The timing of t_p (i.e. **Figure 4a**) remains unchanged so is not
 642 repeated in these figures. Row (a) in each figure shows presents the expected gradually
 643 varying, ramped elevational gradient in M' . Row (b) of each figure shows instantaneous area-
 644 integrated runoff (which assumes instant arrival of climatologically produced runoff at the
 645 terminal moulin) for each IDC, as previously used to simulate meltwater injection into the ice
 646 sheet (27, 28). Row (c) of each figure shows dramatic differences from the top two rows, with
 647 **Figure 5c** (time 1400) moulin discharges lower than model output and nighttime moulin
 648 discharges (time 2400 on 21 July 2015, **Figure S11c**) considerably higher. Heterogeneous IDC
 649 areas and shapes yield different t_p and Q_{pk} . For each IDC, time series of M' , instantaneous area-
 650 integrated R , and SUH-routed R was computed over the time period of 0000 to 2400 on 21 July
 651 2015. From these time series the maximum (Q_{pk}) and minimum hourly runoff values were

652 extracted in ArcGIS software with Arcpy scripts, and difference to obtain daily diurnal difference
 653 data (in units of discharge, $\text{m}^3 \text{s}^{-1}$). The time lag between peak climatological melt production
 654 M' and Q_{pk} was also computed, and equaled zero for instantaneous area-integrated R , but up to
 655 12 hours for SUH-routed R . Summary scatterplots of these Q_{pk} , diurnal difference, and time-lag
 656 data show lower peak discharges, less diurnal contrast, and non-trivial timing delays in SUH-
 657 routed runoff and are presented in **Figure 6**.

658

659 5.3 Retroactive validation of SUH using field data of McGrath *et al.* and Chandler *et al.*

660 To validate our SUH routing model for other times and locations on the ice sheet, we applied it
 661 retroactively to the previous field sites of McGrath *et al.* (6) and Chandler *et al.* (5) to determine
 662 the ability of SUH to independently reproduce peak runoff time and lag time to peak t_p (i.e.,
 663 time lag between peak melt generation across the catchment and peak discharge at the
 664 terminal moulin) observed in their field measurements of supraglacial stream level. Owing to
 665 known water leakage at these sites (e.g. $\sim 48\%$ runoff infiltration to crevasses (6)) and absence
 666 of hourly climate/SMB model output prior to 2015, we did not assess Q_{pk} at these sites.
 667 Hydrograph lag time to peak, however, is dominated by catchment morphometry (not absolute
 668 magnitudes of melting and runoff), and so offers a useful independent test of the SUH approach
 669 even in supraglacial catchments where runoff leakage to crevasses is known to occur.

670 **Table S4: Validation of SUH model with field data of McGrath *et al.* (6) and Chandler *et al.* (5)**

| | | Synthetic Unit Hydrograph (SUH) | | | Field-measured |
|---------------------------|------------------------|---------------------------------|-----------|----------|------------------------|
| | | MAR 3.6 | RACMO 2.3 | HIRHAM 5 | |
| McGrath et al. (2011) | Date | 10 August 2015 | | | 3-17 August 2009 |
| | Peak melt time | 15:00 | 14:00 | 19:00 | 14:00 \pm 231 min |
| | Peak runoff time | 17:00 | 16:00 | 20:00 | 16:30-17:00 |
| | Lag time to peak t_p | 2 hours | 2 hours | 1 hour | 2.8 \pm 4.2 hours |
| Chandler et al. (2013) | Date | 3 July 2015 | | | 29 June to 7 July 2011 |
| | Peak melt time | 13:00 | 13:00 | 19:00 | - |
| | Peak runoff time | 18:00 | 17:00 | 22:00 | 18:00-20:00 |
| | Lag time to peak t_p | 5 hours | 4 hours | 3 hours | - |

671 The catchment studied by McGrath *et al.* (6) is in the Swiss Camp area, approximately 284 km
 672 north of our field site. We obtained the same WorldView-1 image used by McGrath *et al.* (6)
 673 (acquired on 15 July 2009, catalog ID: 1020010008AB4800) and followed McGrath *et al.* (6) to
 674 map the catchment boundary. We then created the catchment centroid and manually
 675 measured the main-stem stream length. The resultant catchment area (A_{dc}) is 1.1 km^2 , main-
 676 stem length (L) is 2.1 km, and the distance from the catchment outlet (i.e. terminal moulin) to
 677 the point on the main channel nearest to the catchment centroid (L_c) is 1.2 km. We then

678 generated a SUH for this catchment as per Methods **Section 5.2**. Finally, the peak climate/SMB
679 melt time, peak runoff (discharge) time, and lag time-to-peak t_p were calculated. Depending on
680 choice of input climate/SMB model, the resultant SUH-derived t_p values range from 1 – 2 hours
681 (**Table S4**), which is smaller but comparable to the field-based 2.8 ± 4.2 hours (6). Depending
682 on input model, peak runoff times ranged from 16:00 to 20:00, comparable to 16:30-17:00 in
683 the field measurements of McGrath et al.

684 Chandler *et al.* (5) also reported the peak river discharge time for an IDC (moulin site L41)
685 during 29 June to 7 July 2011. We used a WorldView-1 image acquired on 12 July 2011 (catalog
686 ID: 103001000CB46800) to delineate the IDC catchment boundary and mainstream as per
687 above. The resultant A_{idc} is 18.2 km^2 , L is 6.9 km, and L_c is 3.6 km. The resultant SUH-derived
688 peak runoff time is 17:00-22:00, which matches well with the peak of 18:00-20:00 observed in
689 the field measurements of Chandler et al. (**Table S4**). In sum, despite using hourly climate
690 model output from 2015 to drive the SUH model, values of C_p , C_t and m calibrated at Rio Behar
691 catchment, and application to different locations and years, we find comparable values in the
692 timing of peak moulin runoff between these two previously published field studies and their
693 respective SUH-routed values as determined retroactively using their remotely sensed fluvial
694 catchments.

695

696 **Methods 6. Regional climate/SMB model descriptions and data analysis**

697 Hourly simulations of GrIS meltwater production M and runoff R over the study period were
698 generated using the HIRHAM5, MAR3.6, RACMO2.3, MERRA-2, and point SEB models with
699 descriptions as follows. Note that there is no overland surface catchment routing scheme
700 present in any of the model simulations in this study. MAR has a built-in routing delay intended
701 to represent meltwater passage through the ice sheet to its edge; this delay is left in place for
702 **Figure 3** and **Figure 7a** but is eliminated in **Table S5**. HIRHAM5 does introduce a delay for
703 runoff from snow (slush), but melting over bare ice converts to immediate runoff. Most
704 current models do not consider penetration of shortwave radiation and associated subsurface
705 melting (29), so this option was turned off in point SEB, to maintain consistency across models.

706 6.1 HIRHAM5:

707 The HIRHAM5 regional climate model (30) is developed by the Danish Meteorological Institute
708 and the Potsdam Research Unit of the Alfred Wegener Institute Foundation for Polar and
709 Marine Research. It has a native horizontal spatial resolution of $5.5 \times 5.5 \text{ km}$ ($0.05^\circ \times 0.05^\circ$ on a
710 rotated pole grid (31)) with 8 native-resolution grid cells intersecting Rio Behar catchment. It
711 combines the dynamics of the HIRLAM weather forecast model (32, 33) with the physical

712 parameterization schemes of the ECHAM climate model (34). Six hourly inputs of horizontal
713 wind vectors, temperature, and specific humidity from the ERA-Interim reanalysis dataset (35)
714 are supplied at the domain boundaries at all atmospheric levels to compute the atmospheric
715 circulation within the domain at 90 s time steps. The resulting surface fluxes of energy
716 (turbulent and downward radiative) and mass (snow, rain, evaporation, and sublimation) are
717 used to drive an offline snow/ice subsurface scheme which provides SMB, runoff and refreezing
718 rates (36). A number of updates have been made to the subsurface scheme compared to the
719 version used by Langen *et al.* (36). The surface energy budget calculation incorporates daily
720 observed MODIS MOD10A1 surface albedo de-noised after Box *et al.* (37). Snow undergoes
721 temperature and pressure dependent densification (38).

722 As illustrated by Lucas-Picher *et al.* (31), ice sheet accumulation is quite accurately represented
723 with biases in the south generally smaller than 10% compared to ice core-derived accumulation
724 rates (31). In the Nuuk area, runoff was found to be underestimated by 10-20%, mainly due to
725 too high albedo in the lower ablation zone (36). With the MODIS-derived albedos employed
726 here, this effect is expected to be limited. HIRHAM5 is run at higher vertical resolution than in
727 Langen *et al.* (36), thus employing 25 layers with a total water equivalent depth of 70 m.
728 HIRHAM5 does not employ any nudging inside the model domain, and the driving atmospheric
729 fields from ERA-Interim are thus only felt on the domain's lateral boundaries. The aerodynamic
730 roughness length for momentum (z_0) is set to a constant value of $z_0 = 1$ mm for both snow and
731 bare glacier ice.

732 When snow/firn is present and a layer bulk density exceeds the pore close off density, water
733 percolating from above is treated as a slush layer that runs off with a time scale depending on
734 surface slope (39, 40). During bare ice conditions, however, any melt that occurs is
735 immediately converted to runoff with no delay. For this particular study, hourly output was
736 supplied from January 1 to August 31 2015, following a spin-up period of 70 years. Rain is
737 parameterized in the model but did not occur at the study site during the study period.
738 HIRHAM5 assumes all energy fluxes to balance at the surface skin layer with no allowance of
739 shortwave radiation penetration and associated subsurface melting.

740 6.2 MAR3.6:

741 The Modèle Atmosphérique Régionale (MAR) is a modular atmospheric model that uses the
742 sigma-vertical coordinate to simulate airflow over complex terrain (41, 42) and the Soil Ice
743 Snow Vegetation Atmosphere Transfer scheme (SISVAT) (43, 44) as the surface model. It has a
744 native horizontal spatial resolution of 20×20 km with 2 native-resolution grid cells intersecting
745 Rio Behar catchment. The snow-ice part of SISVAT, based on the CEN (Centre d'Etudes de la
746 Neige) snow model called CROCUS (45), which calculates albedo for snow and ice as a function
747 of snow grain properties, which in turn are dependent on energy and mass fluxes within the

748 snowpack. CROCUS is a one dimensional multilayered energy balance model that determines
749 the exchanges between the sea ice, the ice sheet surface, the snow-covered tundra, and the
750 atmosphere. It allows meltwater refreezing and snow metamorphosis, influencing the
751 transformation of snow to ice and the surface albedo using the CROCUS formulations(45, 46).
752 For snowpack having surface density $> 550 \text{ kg m}^{-3}$ (representing the maximum density of pure
753 snow), the minimum allowed albedo is calculated linearly as a smooth function between pure
754 snow albedo (0.7) and clean ice (0.55) (47).

755 The lateral and lower boundary conditions are prescribed from meteorological fields modelled
756 by the global European Centre for Medium-Range Weather Forecasts (ECMWF) Interim
757 Reanalysis (ERA-Interim, [http://www.ecmwf.int/en/research/ climate-reanalysis/era-interim](http://www.ecmwf.int/en/research/climate-reanalysis/era-interim)).
758 Sea-surface temperature and sea-ice cover are also prescribed in the model using the same
759 reanalysis data. The atmospheric model within MAR interacts with the CROCUS model, which
760 provides the state of the snowpack and associated quantities (e.g. albedo, grain size). No
761 nudging (assimilation of AWS meteorological data to improve model performance) or
762 interactive nesting was used in any of the experiments. This is not done with MAR, which uses
763 only reanalysis data as input to its atmospheric model. The aerodynamic roughness length for
764 momentum is set to a constant value of $z_0 = 0.1 \text{ mm}$ for dry snow. For melting snow or ice z_0 is a
765 function of density and varies between 1 and 3 mm for both snow and bare glacier ice. An
766 optional MAR representation for shortwave radiation penetration and associated subsurface
767 melting into bare ice has been developed but to maintain consistency with other models was
768 not used here.

769 The Greenland topography used for our simulations was derived from the high-resolution (5
770 km) digital elevation model from radar altimetry (48, 49), and the ice sheet mask is based on
771 the Greenland land surface classification mask from Jason Box ([http://bprc.osu.edu/wiki/Jason
772 Box Datasets](http://bprc.osu.edu/wiki/Jason_Box_Datasets)) using MODIS calibrated radiances imagery.

773 MAR is the only climate/SMB model integrating a runoff delay function to retard bare-ice
774 surface runoff over time. This delay function was proposed by Zuo and Oerlemans (40) based
775 on the idea that surface meltwater probably reaches the supraglacial rivers quicker when the
776 general surface slope is larger. Lefebre *et al.* (39) updated the coefficients of this delay function
777 to route meltwater more quickly. This MAR delay function describes the time lag from surface
778 meltwater production to its drainage through the ice sheet to its edge.

779 6.3 RACMO2.3:

780 The RACMO2 regional climate model uses the atmospheric dynamics module from the High
781 Resolution Limited Area Model (HIRLAM) and adopts the physics package of the European
782 Centre for Medium-range Weather Forecasts Integrated Forecast System (ECMWF-IFS)(32, 33).

783 It has a native horizontal spatial resolution of 11×11 km with 3 native-resolution grid cells
784 intersecting Rio Behar catchment. For a detailed description of the basic version of Regional
785 Atmospheric Climate Model (RACMO2) the reader is referred to Van Meijgaard *et al.*(50). A
786 polar version of RACMO2 has been developed by the Institute for Marine and
787 Atmospheric Research (IMAU), Utrecht University, and is especially adapted for use over
788 ice sheets and glaciated regions. It is interactively coupled to a multilayer ($N_{\max} = 100$), 1-
789 dimensional snow model, accounting for meltwater percolation, refreezing and runoff (51); a
790 snow albedo scheme with prognostic snow grain size (52, 53) and a drifting snow module,
791 simulating snow erosion and drifting snow contribution to sublimation (54). For ice albedo an
792 11 km version of the 500 m Moderate-resolution Imaging Spectroradiometer (MODIS) 16-days
793 Albedo product (MCD43A3) is used. Bare ice albedo is estimated as the averaged 5% lowest
794 surface albedo measurements for the period 2001- 2010 (55). The firn layer is initialized using
795 3D temperature and density fields from previous runs with a dedicated firn model (52, 53).
796 Every six hours, RACMO2 is forced at the lateral boundaries by ERA-Interim reanalysis data
797 (1958-2015). Recently, RACMO2 has been updated to version 2.3 (56) and leading to
798 improved representation of GrIS SMB (55). The present study uses this latest version
799 RACMO2.3. The model has proven to realistically simulate SMB and climate of the GrIS, as well
800 as the extent of the perennial firn aquifer in southeast Greenland (57). SMB gradients are
801 well captured, but accumulation in the interior ice sheet appears underestimated by 5-10%
802 (integrated value). Other perceived weaknesses of the model are the assumptions of
803 temporally constant ice albedo, and instantaneous runoff. RACMO2.3 does not employ any
804 nudging inside the model domain, and the driving atmospheric fields from ERA-Interim are thus
805 only felt on the domain's lateral boundaries. The model assumes fixed values for roughness
806 length of $z_0 = 1$ mm over snow and 5 mm over bare ice.

807 RACMO2.3 assumes all energy fluxes to balance at the surface skin layer with no allowance of
808 shortwave radiation penetration and associated subsurface melting. No time delay is
809 introduced between melt generation and runoff.

810 6.4 MERRA-2:

811 MERRA-2 is a global atmospheric reanalysis produced by the NASA Global Modeling and
812 Assimilation Office (GMAO) for the satellite observing era from 1980 until the present at a grid
813 spacing of $\frac{1}{2}^\circ$ latitude by $\frac{1}{3}^\circ$ longitude and 72 hybrid-eta levels from the surface to 0.01 hPa
814 (58). Over our field area it therefore has a native horizontal spatial resolution of 56×28 km
815 with 1 native-resolution grid cell intersecting Rio Behar catchment. MERRA-2 serves as an
816 update on the previous MERRA product (59) by incorporating radiance data from more recent
817 satellites including NOAA-19, MetOp-A and -B, and the Suomi National Polar-orbiting
818 Partnership (Suomi-NPP). The background model is the Goddard Earth Observing System

819 model, version 5 (GEOS-5). The model uses a finite-volume dynamical core (60) that is
820 integrated with various physics packages. These physical packages incorporate several
821 improvements, which are described in Molod *et al.* (61). Additionally, MERRA-2 incorporates
822 several new features including an interactive aerosol analysis, a scheme to conserve globally-
823 averaged atmospheric mass and moisture (62), and the use of a cubed sphere grid for
824 computations. The representation of glaciated land surfaces has been updated as described
825 and evaluated (63). The model represents energy conduction properties of the upper 15 m of
826 glacial ice, and energy and hydrologic properties of an overlying, variable snow cover.

827 Snow hydrology follows a modified version of the Stieglitz model, which provides an explicit
828 representation of snow densification, meltwater runoff, percolation, refreezing, and surface
829 albedo (64, 65). Over land ice, the snow pack is vertically discretized into fifteen layers, which
830 are demarcated by fractions of the total snow depth. Firn of density greater than 500 kg m^{-2} is
831 not explicitly represented; this provides an approximate upper limit on the total depth of the
832 snow pack. Snow cover is also allowed to be fractional. A prognostic surface albedo is based on
833 Greuell and Konzelmann (66). Bare ice albedo is set to 0.58. As described in Lynch-Stieglitz (65),
834 meltwater is generated when the heat content of a snow layer exceeds the minimum necessary
835 for the layer to remain entirely frozen (65). A liquid water holding capacity is defined for each
836 snow layer (67). Meltwater exceeding the layer holding capacity is transferred to the next
837 lowest layer. Liquid water leaving the lowest model layer is instantaneously designated as
838 runoff. The fractional bare ice cover may also generate runoff based on the excess melt energy
839 from the surface energy budget. No delay is introduced between melt production and runoff.

840 For efficiency, MERRA-2 was integrated in four processing streams: 1980-1991, 1992-2000,
841 2001-2010, and 2011 to the present. A one-year overlap for each stream was incorporated to
842 avoid temporal discontinuities in the transitions, particularly in land surface variables. It was
843 recognized that the annual temperature wave would not reach lower levels of the surface
844 representation over glaciated land. As a result, glaciated land variables are restricted to those
845 describing albedo, fractional snow cover, and runoff. Like RACMO2.3, MERRA-2 assumes fixed
846 values for roughness length of $z_0 = 1 \text{ mm}$ over snow and 5 mm over bare ice. RACMO2.3
847 assumes all energy fluxes to balance at the surface skin layer with no allowance of shortwave
848 radiation penetration and associated subsurface melting. Meltwater production M is not
849 supplied by MERRA-2, thus precluding consideration of MERRA-2 from many parts of this
850 analysis.

851 6.5 Point SEB:

852 The point-based SEB model (68) calculates SMB using in-situ measurements from the KAN_M
853 automatic weather station (67.0667 N, 48.8327 W, 1270 m a.s.l.; **Figure 1**). Being a point-based
854 model, the outputs driven by the KAN_M station were simply extrapolated to the rest of Rio

855 Behar catchment. The model's inability to calculate spatial variability within the domain is a
856 trade-off for accurate, local forcing at hourly time steps. Measurements of absorbed shortwave
857 (solar) radiation and downward longwave (terrestrial) radiation feed into the model. The
858 turbulent heat fluxes are calculated similarly to those produced by the RCMs, using near-
859 surface gradients in temperature, wind speed and specific humidity to approximate vertical
860 transport of sensible and latent heat. The sub-surface thermal calculations are performed to a
861 depth of 20 m with 0.2 m spacing, which is initialized using thermistor string measurements of
862 ice temperature, and assuming a constant ice density and thermal conductivity for this ablation
863 area site in summer. The energy flux calculations of upward longwave radiation, sensible heat,
864 latent heat and sub-surface heat make use of surface temperature; the model iteratively
865 determines the surface temperature for which all surface energy fluxes are in balance. If
866 surface temperature is capped by a 0°C melting surface, the surplus energy determines the
867 melt rate. The calculated meltwater at the ice sheet surface can theoretically refreeze in sub-
868 surface model firn layers, yet for this study's location and observational period no snow or firn
869 was present at the AWS. Therefore modeled surface meltwater runoff equals the meltwater
870 production, with minor compensation for condensation and evaporation. Rain is
871 parameterized in the model but did not occur at the study site during the study period. For the
872 study region and season the 1-dimensional SEB model assumes an aerodynamic roughness
873 length of 0.1 mm following Smeets and van den Broeke (69).

874 We used KAN_M measurements of incoming and outgoing shortwave radiation to determine
875 how much energy was absorbed at the surface, so did not assume a pre-defined albedo. The
876 SEB model does provide the possibility to allow shortwave radiation to penetrate the surface
877 following Beer's law and generate subsurface melting. However, we did not use that option in
878 our model calculations for several reasons: 1) to enable consistency with the other models that
879 don't allow penetration; 2) a necessary extinction coefficient for the high dust/high algae
880 content ice at KAN_M is currently unknown; 3) a necessary runoff threshold for meltwater
881 generated within the ice matrix is currently unknown. In sum, the SEB radiation penetration
882 scheme requires further research and development before implementation.

883 6.6 Reprojection of all model outputs to a common resolution and grid:

884 To improve comparison among these models, their outputs of meltwater production M and
885 runoff R were reprojected to a common 5 km posting and map projection (i.e. to that of MAR)
886 using a 'drop in a box' (nearest neighbor) resampling. This method was chosen over use of an
887 interpolation scheme, to preserve the native model output with in situ field measurements.
888 Thus the native grid cell resolutions remain visible in **Figure 5a** and **Figure S11** despite finer-
889 scale resampling to 5 km.

890 The common projection chosen is Polar Stereographic (70) based on the WGS84 ellipsoid, with
 891 true scale at 71° S and posting of 5 km. The map reference latitude was set at 90° N and
 892 reference longitude at 39° W. Map origins were adjusted per MAR outputs. For area and
 893 volume calculations, the Lambert Azimuthal Equal Area projection was used (70). Latitude and
 894 longitude values for the different datasets were converted to map co-ordinates. Finally, the
 895 reprojected variables were interpolated onto the 5 km grid (48, 49), using nearest-neighbor
 896 interpolation. Note that this sampling is generally finer than the native resolutions of most
 897 models, allowing smoother interpolation across the watershed.

898 Two exceptions to the above processing stream are the MERRA-2 and point SEB models.
 899 Because MERRA-2 does not provide *M* as a model output, assessments of melt production,
 900 runoff ratios, and SUH parameters are not possible for this model. Because SEB is a point-
 901 based, non-gridded model driven by an AWS, outputs of *M* and *R* were applied uniformly across
 902 the Behar catchment surface area without adjustment, owing to identical elevation and close
 903 proximity of the KAN_M AWS station to Behar catchment.

904 6.7 Comparison of model outputs with field observations from Rio Behar catchment:

905 **Table S5: Climate/SMB model and field measurements of *M* and *R***

| | Melt (mm) | Runoff (mm) | Difference (mm) |
|---|-------------------|-----------------|-----------------|
| MAR 3.6* | 51.1 | 41.7 | 9.4** (-0.4) |
| Point SEB | 46.7 | 47.8 | -1.1 |
| RACMO 2.3 | 51.1 | 51.7 | -0.6 |
| HIRHAM 5 | 67.6 | 61.0 | 6.6 |
| MERRA 2 | N/A | 30.4 | N/A |
| Observation (ablation stakes, ADCP)* | 19.0-26.9 | 31.4 | -12.4 - -4.5 |
| Observation (KAN-M, ADCP) | 16.2-23.0 | | -15.2 - 8.4 |
| Overestimation/underestimation by models | +73.6% to +317.3% | -3.4% to +94.2% | 75.6% - 246.7% |

906 *MAR runoff *R* and observed ADCP discharge are lagged by 5 hours to secure peak-to-peak matching

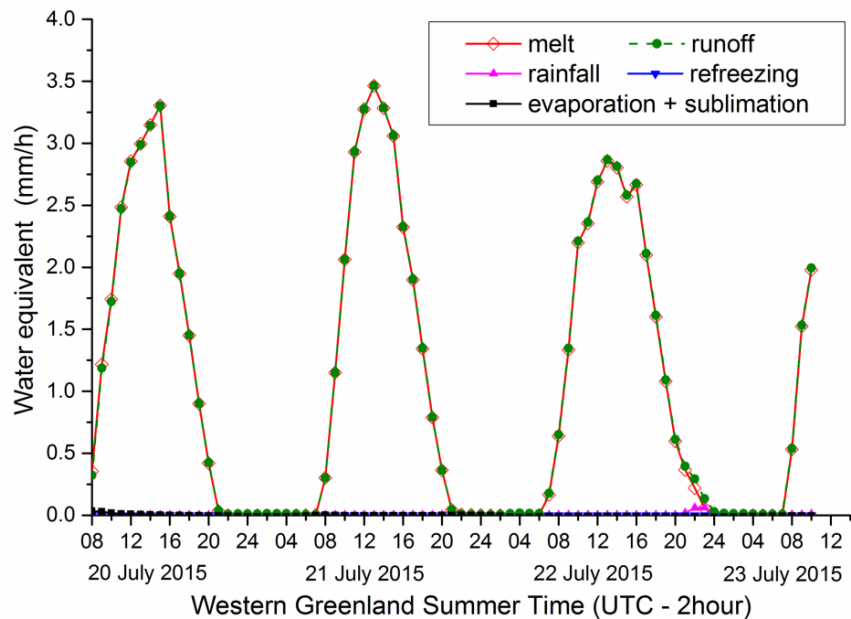
907 **Value 9.4 is unrealistic due to delay-to-edge *R* smoothing unique to MAR. The more appropriate
 908 value, calculated directly from raw MAR SMB variables is -0.4 mm.

909 For the four gridded climate/SMB models (HIRHAM5, RACMO2.3, MAR3.6, MERRA-2) hourly
 910 model outputs of melt *M* and runoff *R* were computed within Behar catchment using Python
 911 and ArcGIS (13, 71). This procedure entails clipping the 5 km × 5 km model grid cells with the
 912 catchment polygon boundary, weighting the runoff/melt values of each grid cell by the percent
 913 area contained within the catchment, and summing their corresponding runoff/melt values to
 914 compute the total runoff/melt ($m^3 s^{-1}$) inside the catchment (13). Note that for presentation of

915 climate/SMB model output of R , there is no physical difference between use of units of
916 discharge Q ($\text{m}^3 \text{s}^{-1}$) and runoff depth (mm/hour) they are interchangeable via unit conversion
917 using the mapped catchment area (km^2). Presentation of modeled runoff R in units of
918 discharge ($\text{m}^3 \text{s}^{-1}$) is derived by multiplying model output of R (in units of mm hr^{-1}) times our
919 minimum, mid- and upper catchment areas (km^2), to obtain units of discharge ($\text{m}^3 \text{s}^{-1}$) suitable
920 for direct comparison with in situ ADCP measurements. The upper and lower uncertainty
921 bounds on modeled runoff (in units of Q) of **Figure 3** and **Figure 7a** thus reflect model
922 uncertainty due solely to catchment area uncertainty.

923 For a 37.5 hour melt-production period with overlapping ADCP discharge and ablation stake
924 measurements (over the overlapping period July 21, 11:00 am to July 23, 00:30 am local
925 Greenland time, see **Table S5**) the various models overestimated runoff by -3% to +94%, due to
926 the combined effects of overestimated melt production (~8% to 57% overestimation) and
927 underestimated water retention/refreezing processes (~44% to 109% underestimation). For
928 these runs, the difference between M and R in the models is driven by modeled meltwater
929 retention and/or refreezing processes, except for a brief, minor rainfall event modelled by SEB,
930 MAR 3.6, and RACMO 2.3 at approximately 22:00 on 22 July, which added to the runoff
931 calculation thus increasing it slightly over R and small negative differences in **Table S5**. Note
932 that runoff = melt - refreezing + rain + condensation - evaporation, so melt and runoff are not
933 expected to be identical. In particular, runoff may exceed melt due to rain and/or
934 condensation.

935 The seemingly large $M - R$ difference for MAR3.6 (9.4 mm in **Table S5**) is in fact an artifact of
936 this particular model's aforementioned delay-to-edge smoothing of standard model output of R
937 (this feature also greatly smooths the MAR temporal runoff signal as seen in **Figure 3** and
938 **Figure 7a**). A clearer view of how MAR really works is provided by calculating R directly from
939 the raw model data ($R = \text{melt} + \text{rain} - \text{refreezing} - \text{evaporation} - \text{sublimation}$) as per **Figure S7**.
940 This figure clearly confirms that $M \sim R$ in the MAR3.6 simulations for Behar catchment (and
941 indeed are virtually identical), with negligible retention/refreezing of runoff. The slightly
942 negative $M - R$ difference (-0.4 mm, **Table S5**) results from a modelled trace rainfall event.

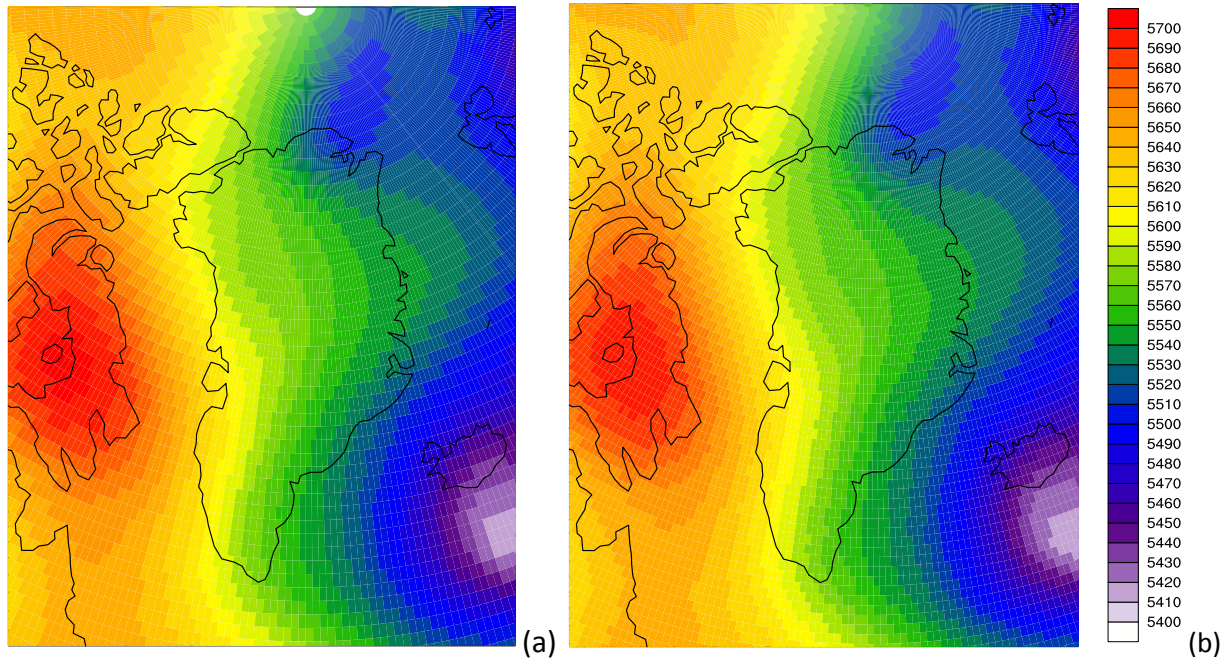


943

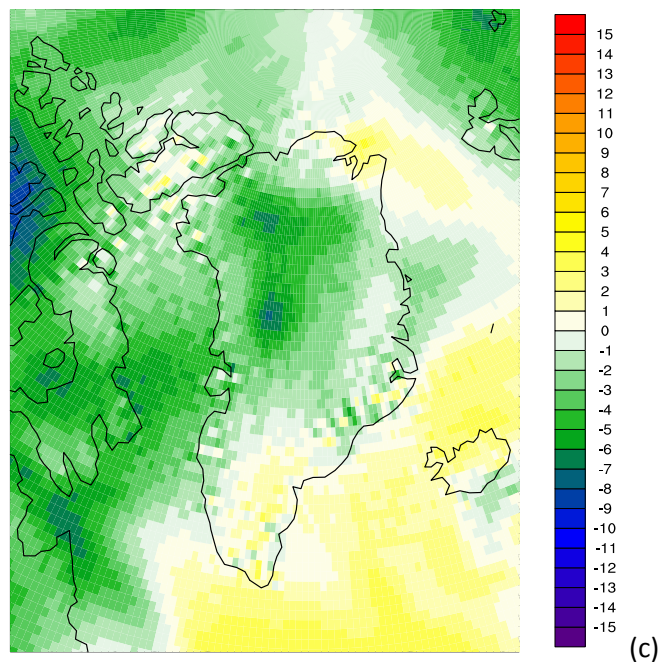
944 **Figure S7: Raw SMB components from the MAR 3.6 model over the experiment period show zero or**
 945 **minimal refreezing, sublimation, evaporation, and rainfall, hence $R \sim M$ with negligible meltwater**
 946 **retention simulated for the ice sheet surface. Note that direct calculation of runoff R from these raw**
 947 **MAR variables (i.e. runoff = melt + rain - refreezing - evaporation - sublimation) eliminates the delay-**
 948 **to-edge smoothing applied to MAR R standard output, providing the more realistic $M-R$ difference (-**
 949 **0.4 mm, with negative value due to a trace rainfall event) shown in Table S5.**

950 Because MERRA-2 does not supply outputs of melt M , we cannot directly confirm that its lower
 951 estimates of runoff R are due to better approximation of M or some other driver. The three
 952 regional climate models HIRHAM 5, RACMO 2.3, MAR 3.6 are forced with ERA-Interim
 953 reanalysis data, for example, whereas MERRA-2 performs its own reanalysis. However, our
 954 comparison of ERA-Interim and MERRA-2 geopotential height fields over the 20-23 July 2015
 955 study period shows that two reanalysis datasets are virtually identical, with little difference
 956 between them during our field experiment (**Figure S8**). Furthermore, Point SEB was driven by
 957 in situ meteorological observation from the KAN_M AWS, not reanalysis, yet shows similar
 958 overestimation in ice surface lowering and runoff as the other models (Figure 3, Figure 7).
 959 Another possible difference with MERRA-2 regards snow availability: In the MERRA-2
 960 configuration, a strong delineation occurs between fresh snow and bare ice, as opposed to the
 961 other models that have explicit representation of firn. Finally, because MERRA-2 computes a
 962 prognostic surface albedo (66) yielding a bare ice albedo of 0.58, its albedo is higher than the
 963 other models, thus reducing the amount incoming shortwave radiation converted to melting
 964 and runoff.

965



966



967 **Figure S8. Instantaneous 500 hPa geopotential height fields (values in meters) averaged for 0, 6, 12,**
968 **and 18Z during 20-23 July 2015 for: (a) ERA-Interim; (b) MERRA-2; the difference (c) of MERRA-2 minus**
969 **ERA-Interim. To generate (c) ERA-Interim data were interpolated to the MERRA-2 grid using spherical**
970 **harmonics. Representations of atmospheric dynamics during the study period are virtually identical in**
971 **both reanalysis datasets, with near-zero differences over southwestern Greenland.**

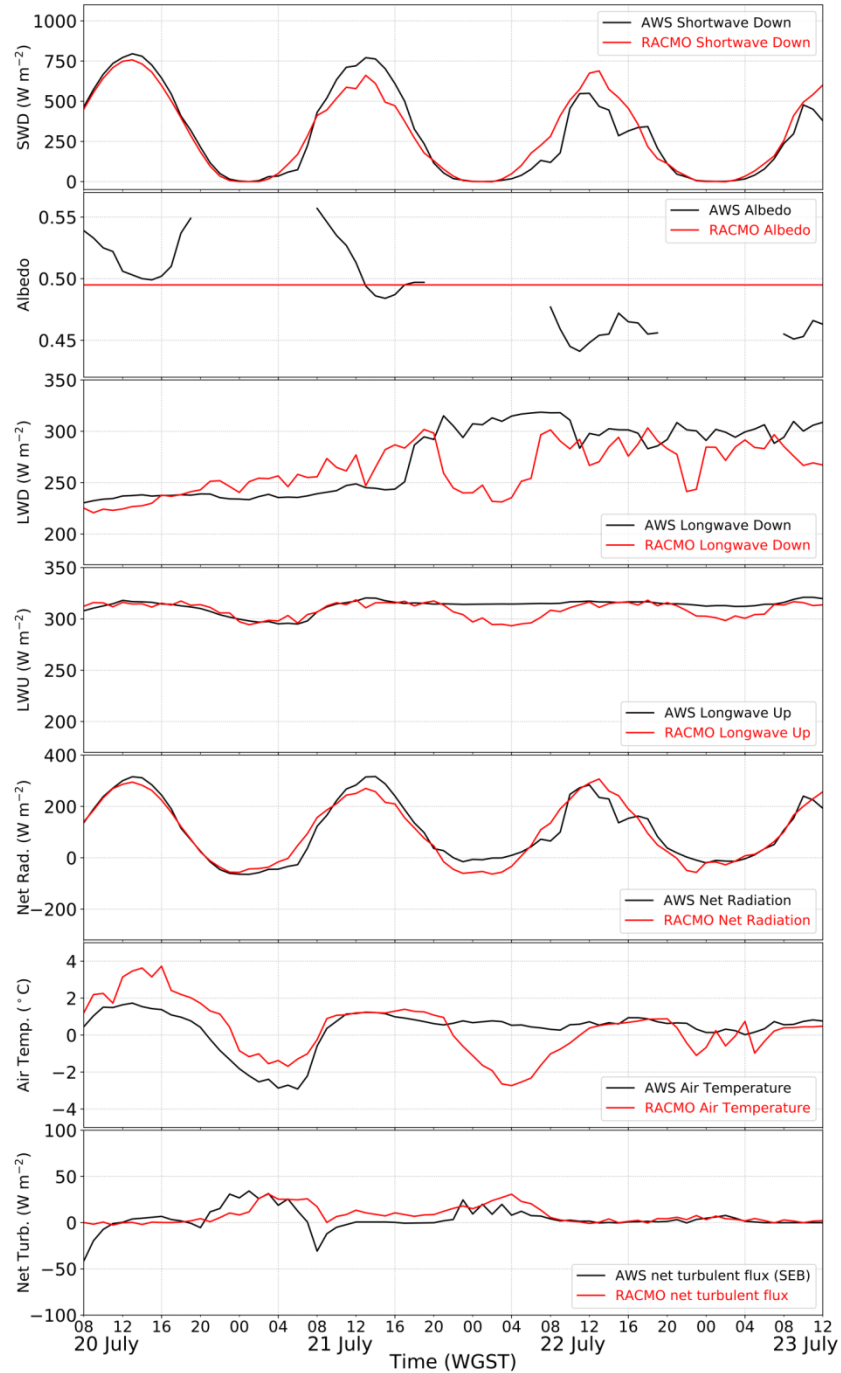
972

973 6.8 Comparison of RACMO2.3 albedo and surface energy balance with AWS measurements

974 To determine if discrepancies in modeled versus observed surface energy balance might explain
975 the observed discrepancies between modeled versus observed ablation and runoff, we
976 obtained hourly measurements of energy balance components collected by the KAN_M AWS
977 during our field experiment. These data were compared with hourly surface energy balance
978 outputs from RACMO2.3, as a representative of the four climate/SMB models that
979 overestimated surface runoff during the field experiment and for which detailed surface energy
980 balance outputs are available (**Figure S9**).

981 The RACMO2.3 albedo of 0.49 during the study period was close to AWS measurements (~0.45
982 to 0.55 over the entire period; ~0.46-0.50 during peak radiation hours, **Figure S9, panel 2**). We
983 also obtained MODIS satellite albedo retrievals (MYD10A1 daily product) and found that the
984 mean remotely sensed albedo across Rio Behar catchment was 0.43 on 20 July and 0.41 on 21
985 July - again, not far off from the modeled assumption of 0.49. This somewhat lower albedo
986 from MODIS may help to explain the higher melt and runoff estimates from HIRHAM5 relative
987 to the other models (recall HIRHAM is the only model to use MODIS satellite albedo retrievals),
988 but is of the wrong sign to explain the observed RACMO2.3 runoff overestimation. Together
989 with the good agreement between in situ and RACMO2.3 albedo, we therefore conclude that
990 underestimation of albedo cannot explain the observed overestimation of runoff.

991 To determine if discrepancies in modeled versus observed radiation effects of clouds might
992 explain the observed discrepancies between modeled versus observed ablation and runoff, we
993 compared RACMO2.3 shortwave and longwave radiation with measurements from the KAN_M
994 AWS. From the AWS longwave data and our own field notes, clouds moved into the study area
995 around 20:00 of Day 2 of the field experiment and persisted throughout Day 3. The arrival of
996 these clouds is missed for approximately 12 hours by RACMO2.3, as evidenced by a sustained
997 increase in longwave down (LWD) observed at KAN_M that is not immediately simulated by the
998 model (**Figure S9, panel 3**). The delayed detection of these clouds yields a small model
999 overestimation of shortwave down radiation (SWD), underestimation of LWD, and a small
1000 overestimation of net SW radiation and net total radiation on Day 3 of the field experiment only
1001 (**Figure S9, panel 5**). This small model overestimation of net radiation did not occur on sunny
1002 Days 1 and 2, when climate/SMB models also overestimated observed ice surface lowering and
1003 runoff despite good simulation of net LW radiation and slight *underestimation* of net SW and
1004 net radiation. We therefore conclude that the delayed detection of clouds may have
1005 contributed slightly to the observed model overestimation of ice sheet ablation and runoff on
1006 Day 3, but not during the other two days of our field experiment when model overestimations
1007 also occurred.



1008

1009 **Figure S9: Comparison of RACMO2.3 and KAN_M AWS surface radiation and energy balance**
 1010 **components during the 20-23 July 2015 Rio Behar field experiment. From top to bottom, black lines**
 1011 **show in situ measurements (shortwave down, albedo, longwave down, longwave up, net radiation,**
 1012 **surface air temperature) and net turbulent heat flux (calculated by the SEB model forced by KAN_M**
 1013 **AWS measurements). In general, RACMO2.3 reproduces the in situ surface energy balance quite well,**
 1014 **with small discrepancies in longwave down and net radiation insufficient to explain RACMO2.3**
 1015 **overestimation of observed ice surface lowering and runoff.**

1016 Similarly, a generally good agreement between RACMO2.3 and AWS-derived net turbulent heat
1017 flux (**Figure S9, panel 7**), together with the small magnitude of this flux (less than $\sim 25 \text{ W/m}^2$)
1018 suggest sensible and latent heat fluxes cannot explain the observed phenomena.

1019

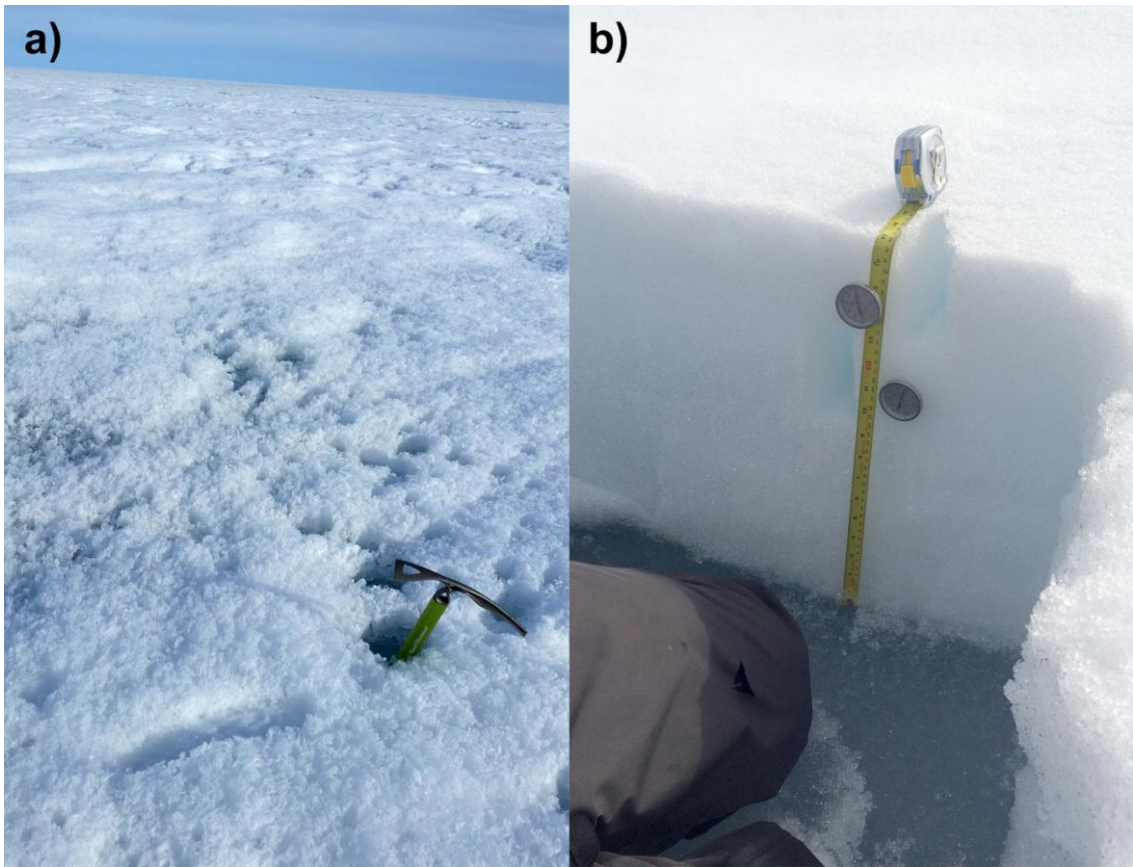
1020 **Supplementary Discussion I: Weathering crust hypothesis for model overestimation of runoff** 1021 **ice surface lowering and supraglacial river runoff**

1022 For this particular field experiment, HIRHAM 5, MAR 3.6, RACMO 2.3, and SEB outputs of Rio
1023 Behar catchment R substantially overestimated our ADCP field measurements of catchment
1024 discharge (**Figure 7a**). If these models' outputs of M are converted to units of equivalent ice
1025 thickness they also substantially overestimated ice surface ablation (**Figure 7b**), even if a low
1026 near-surface ice density measured at our site (0.688 g cm^{-3}) (3) is used for unit conversion
1027 instead of the density of solid ice (0.918 g cm^{-3}) (both density assumptions are presented in
1028 **Figure 7b**). Upon first examination, this suggests that climate/SMB models overestimated
1029 meltwater production M and hence R .

1030 However, an alternate, better-supported hypothesis is that the models estimated M correctly
1031 (or more precisely, the amount of energy allocated to M) but the ablation stakes and KAN_M
1032 surface lowering data underestimated it. A known process for this is shortwave radiation
1033 penetration and subsurface melting of bare ice (29), creating a porous, low density, ice matrix-
1034 supported "weathering crust" (72, 73). Because energy is expended to melt ice beneath the
1035 surface, but an ice matrix remains intact, this can produce less surface lowering than would
1036 occur from surface melting alone (3, 74, 75). Water saturated weathering crust was observed
1037 in abundance in our Rio Behar base camp in 2015, and again in 2016 when its depth exceeded
1038 1.1 m, the maximum length it could be cored (3) (**Figure S10**). Subsurface melting was not
1039 considered in the climate/SMB model simulations. If so, it is possible that our estimates of melt
1040 M derived from ablation stakes and at the KAN_M station may underestimate true melt
1041 production at the site.

1042 A separate bit of evidence supporting this comes from comparison of lagged ADCP discharge
1043 and ablation stake measurements for a 37.5 hour overlap period (**Table S5**), which suggest a
1044 seeming *surplus* of runoff (31.4 mm vs 16.2-26.9 mm). A surplus would signify $R > M$, which is
1045 nonsensical from an energy balance perspective. Again, it's hard to take this comparison too
1046 far because the ablation measurements are highly local, whereas our ADCP discharges integrate
1047 runoff over the entire catchment, but the data cannot rule out the possibility that the surface
1048 lowering data from our ablation stakes and the KAN_M station do not fully reflect the net
1049 surface energy balance that occurred during our field experiment. If so, the observed mismatch
1050 between modeled and measured R was likely caused by meltwater delay, retention, and/or

1051 refreezing within the weathering crust itself. Weathering crust delays meltwater from reaching
1052 supraglacial channels (73, 76, 77) and is known to store and possibly refreeze meltwater at our
1053 field site (3). It is often accompanied with surface expression of water-filled cryoconite holes,
1054 which were ubiquitous around our base camp and the field area more generally, as observed
1055 visually from helicopter transit flights. Any refreezing of this meltwater, which we observed
1056 nightly in cryoconite holes, requires re-melting thus consuming a commensurate fraction of M
1057 the following day (or the following week, or the following year - the residency time of
1058 meltwater found in Rio Behar weathering crust is currently unknown). Small discrepancies in
1059 model-calculated versus measured ablation rates on the Haut Glacier d’Arolla, Switzerland, for
1060 example, likely result from the refreezing of surface water at night, its re-melting the next
1061 morning, and subsurface melting during the afternoon (78). In a model that does not simulate
1062 this process but otherwise correctly quantifies surface melt energy, both ice surface lowering
1063 and runoff would be overestimated.



1064
1065 **Figure S10: (a) The exposed, bare-ice ablation surface at Rio Behar base camp is characterized by**
1066 **weathering crust, a porous, water saturated, low density, ice matrix-supported crust >1 m deep (see**
1067 **ice axe and footprint for scale). (b) Solid, high-density ice that was protected from shortwave**
1068 **penetration and subsurface melting by a remnant cap of seasonal snow. Photos by (a) Laurence C.**
1069 **Smith and (b) Matthew G. Cooper.**

1070

1071 Another, less likely possibility is additional missed leakage in Rio Behar catchment even beyond
1072 the internally drained areas and crevasse fields manually identified and removed from the
1073 WorldView satellite imagery. While crevasse fields were visually excluded from our lower
1074 bound catchment map, some may have been missed, and it is possible that variable water
1075 storage occurs within crevasses which grow and/or fluctuate in volume with changing ice
1076 velocities. Field observations and repeat satellite/UAV imaging of solitary cracks/lineaments
1077 running through our ADCP river reach and elsewhere strongly suggests that these features are
1078 sealed: none developed into moulins and remotely sensed wetted flow widths were
1079 indistinguishable immediately upstream and downstream of these lineaments, indicating no
1080 reductions in discharge.

1081

1082 **Supplementary discussion II: Scale issue and comparison with GRACE studies**

1083 Size of the study area vs. SMB model domain: As noted in the main text, Behar catchment has
1084 an area between 51.4 and 69.1 km² (with a best estimate 63.1 km²). Other IDCs on the GrIS
1085 surface typically have areas of 10s of km² (e.g. ranging from 0.4 – 244.9 km² for 799 IDCs(7)).
1086 The described procedure for directly measuring runoff R integrates over these scales. As such,
1087 the measurements, coefficients, and fluvial processes described in this paper are broader in
1088 scale than a point-based AWS and are intrinsic to the horizontal scale of a single climate model
1089 grid cell or perhaps several grid cells. While a significant improvement over point
1090 measurements, this scale is still small relative to the spatial domain over which climate/SMB
1091 models are typically run. This cautions the extent to which conclusions and interpretations
1092 drawn from a small subarea may be generalized. For example, local model outputs may differ
1093 from observations by tens of percent, but increasing the domain area improves model results
1094 (79). Also, there are known local variations in model performance, for example at the southern
1095 tip of the GrIS, melt and runoff are likely both underestimated due to sensible heat flux
1096 underestimation (80). The RACMO2.3 1-km downscaled product suggests underestimation in
1097 melt and runoff at the ice sheet margins for the original output at 11-km resolution owing to
1098 too low bare ice albedo and a relatively coarse topography in the low ablation zone. Viewed
1099 from this perspective, even the quite large (from an *in situ* perspective) Rio Behar catchment is
1100 too small to make generalized statements about model performance at the pan-Greenland
1101 scale.

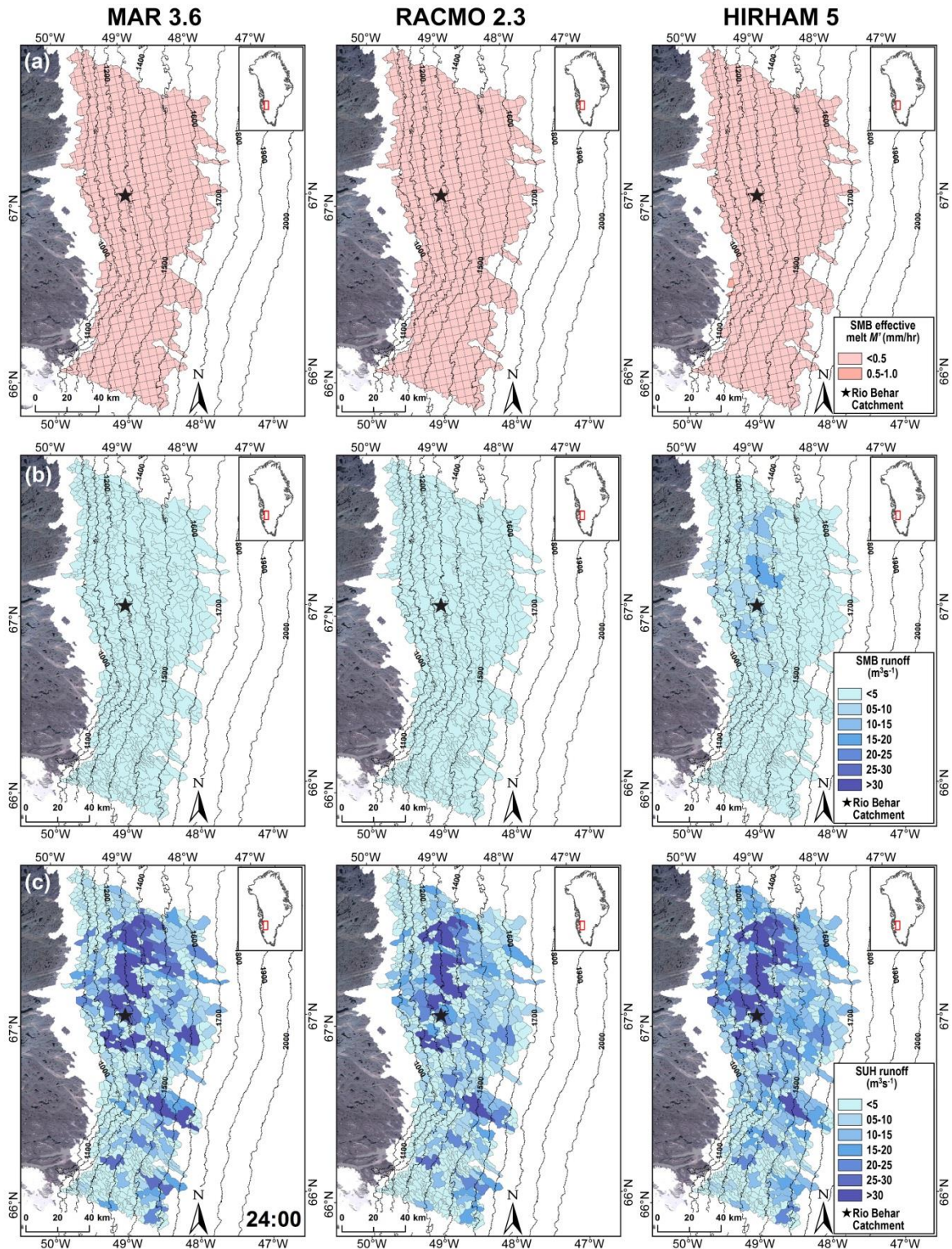
1102 Comparison with GRACE: The second way in which our findings are supported across a broader
1103 geographic scale is through comparison of GRACE (Gravity Recovery and Climate Experiment)
1104 satellite retrievals across melt-intensive sectors of the GrIS ablation zone. In particular, we

1105 examine the important intercomparison studies of GRACE vs. SMB mass loss (or more precisely,
1106 SMB minus ice discharge SMB-D) of Sasgen *et al.* (81) and Xu *et al.* (82). Behar catchment and
1107 its surrounding IDCs (covering of 13,563 km², see above) are contained within Sector F of
1108 Sasgen *et al.* (81) (covering 417,000 km², the second-largest sector in the study) and Sector DS6
1109 of Xu *et al.* (82) (area not provided but similar to Sasgen *et al.* (81)). From Sasgen *et al.* (81),
1110 climate model predictions significantly overestimate mass loss relative to GRACE in this melt-
1111 intensive sector (-66 Gt/yr SMB-D vs. -45 ±8 Gt/yr for GRACE, Table 2). A similar result is found
1112 by Xu *et al.* (82) using the input-output method (IOM), which quantifies the difference between
1113 mass input and output by studying SMB-D. They find IOM mass losses of -14 ±8 Gt/yr (vs. -6 ±9
1114 Gt/yr for GRACE), -32 ±12 Gt/yr (vs. -24 ±8 Gt/yr) and -46 ±14 Gt/yr (vs. -38 ±8 Gt/yr) for time
1115 periods 2003-2007, 2003-2010, and 2003-2012, respectively (Xu *et al.*, Table 1, Sector DS6) (82).
1116 In all cases, surface mass balance over-predicts mass loss relative to GRACE in
1117 western/southwestern Greenland; it is only through model under-prediction of mass loss in
1118 other sectors (notably Sector G in Sasgen *et al.*, and Sector DS8 in Xu *et al.* (82), both northwest
1119 Greenland) that these large differences cancel fortuitously, lending the conclusion of
1120 Greenland-wide agreement between GRACE and SMB-D models. Despite the large
1121 uncertainties associated with these estimates and the much larger geographic areas (mascons)
1122 studied by GRACE, we determine from these studies that SMB-modeled mass losses exceed
1123 GRACE derived mass losses over melt-intensive west/southwest Greenland, consistent with the
1124 findings of this study.

1125

1126 **Supplementary Figures (see following pages)**

1127

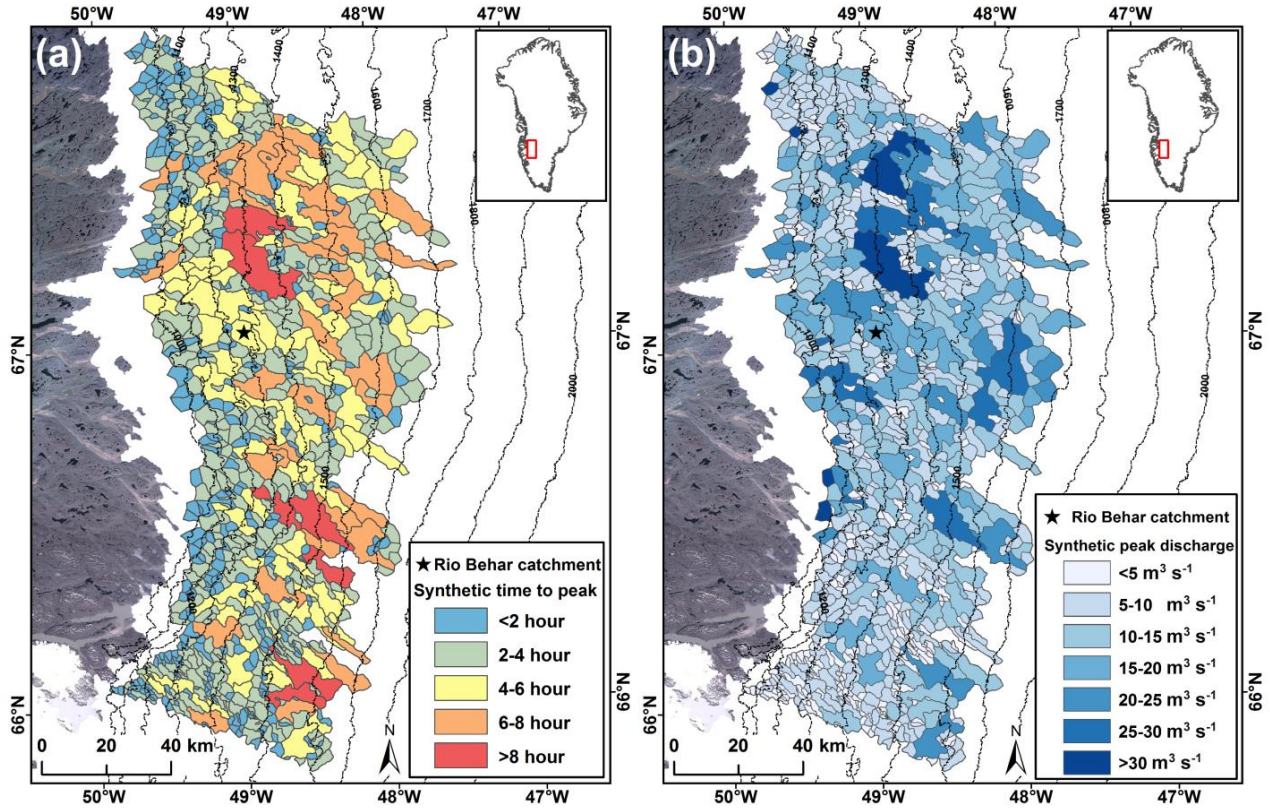


1128

1129 **Figure S11: Companion to Figure 5, showing nighttime runoff ten hours later (0000 on 22 July**
 1130 **2015) for (a) MAR3.6, RACMO2.3, and HIRHAM5 climate/SMB model outputs of corrected**
 1131 **meltwater production (M'); (b) instantaneous area-integrated runoff; and (c) SUH-attenuated**

1132 runoff. Shutdowns of (a) melt production, and (b) runoff are not present in (c), owing to
 1133 continued supraglacial river discharge entering moulines at night. MERRA-2 is not shown
 1134 because it does not output M ; point SEB is not shown because its output is not gridded. Note that
 1135 output (a) has units of water depth equivalent (mm hr^{-1}) and units of discharge ($\text{m}^3 \text{s}^{-1}$)
 1136 following intersection with supraglacial catchment boundaries (b), (c). Black star at
 1137 approximately 67N, 49W denotes Rio Behar catchment.

1138



1139

1140 **Figure S12: Recolored version of Figure 4 for readers having color vision deficiency (for**
 1141 **caption see Figure 4 main text)**

1142

1143

1144

1145

1146 **Supplementary References**

- 1147 1. SonTek (2016) RiverSurveyor S5/M9 System Manual Firmware Version 3.96.
 1148 2. Braithwaite RJ, Konzelmann T, Marty C, & Olesen OB (1998) Errors in daily ablation
 1149 measurements in northern Greenland, 1993-94, and their implications for glacier climate
 1150 studies. *J. Glaciol.* 44(148):583-588.
 1151 3. Cooper MG, *et al.* (2017) Near-surface meltwater storage in low density bare ice of the
 1152 Greenland ice sheet ablation zone. *Cryosph. Discuss.*
 1153 4. Ryan JC, *et al.* (2015) UAV photogrammetry and structure from motion to assess calving
 1154 dynamics at Store Glacier, a large outlet draining the Greenland ice sheet. *Cryosph.* 9(1):1-11.
 1155 5. Chandler DM, *et al.* (2013) Evolution of the subglacial drainage system beneath the Greenland
 1156 Ice Sheet revealed by tracers. *Nature Geosci.* 6(3):195-198.
 1157 6. McGrath D, Colgan W, Steffen K, Lauffenburger P, & Balog J (2011) Assessing the summer water
 1158 budget of a moulin basin in the Sermeq Avannarleq ablation region, Greenland ice sheet. *J.*
 1159 *Glaciol.* 57(205):954-964.
 1160 7. Yang K & Smith LC (2016) Internally drained catchments dominate supraglacial hydrology of the
 1161 southwest Greenland Ice Sheet. *J. Geophys. Res. Earth Surf.* 121:1891-1910.
 1162 8. AgiSoft (2013) AgiSoft PhotoScan.
 1163 9. Shean DE, *et al.* (2016) An automated, open-source pipeline for mass production of digital
 1164 elevation models (DEMs) from very-high-resolution commercial stereo satellite imagery. *ISPRS J.*
 1165 *Photogramm. Remote Sens.* 116:101-117.
 1166 10. Willis MJ, Herried BG, Bevis MG, & Bell RE (2015) Recharge of a subglacial lake by surface
 1167 meltwater in northeast Greenland. *Nature* 518(7538):223-227.
 1168 11. Karlstrom L & Yang K (2016) Fluvial supraglacial landscape evolution on the Greenland Ice Sheet.
 1169 *Geophys. Res. Lett.* 43:2683–2692.
 1170 12. Yang K, Karlstrom L, Smith LC, & Li M (2017) Automated high resolution satellite image
 1171 registration using supraglacial rivers on the Greenland Ice Sheet. *IEEE J. Sel. Topics Appl. Earth*
 1172 *Observ. Remote Sens.* 10(3):845-856.
 1173 13. Smith LC, *et al.* (2015) Efficient meltwater drainage through supraglacial streams and rivers on
 1174 the southwest Greenland ice sheet. *Proc. Natl. Acad. Sci. U.S.A.* 112(4):1001-1006.
 1175 14. Pope A, *et al.* (2016) Estimating supraglacial lake depth in West Greenland using Landsat 8 and
 1176 comparison with other multispectral methods. *Cryosph.* 10(1):15-27.
 1177 15. Pedregosa F, *et al.* (2011) Scikit-learn: Machine learning in Python. *J. Mach. Learn. Res.* 12:2825-
 1178 2830.
 1179 16. Chow VT (1964) *Handbook of Applied Hydrology: A Compendium of Water-resources Technology*
 1180 (McGraw-Hill Company) 1st Ed.
 1181 17. Yates P & Snyder WM (1975) Predicting recessions through convolution. *Water Resour. Res.*
 1182 11(3):418-422.
 1183 18. Tallaksen LM (1995) A review of baseflow recession analysis. *J. Hydrol.* 165(1):349-370.
 1184 19. Dingman SL (2015) *Physical hydrology (3rd edition)* (Waveland press).
 1185 20. Collins WT (1939) Runoff distribution graphs from precipitation occurring in more than one time
 1186 unit. *Civil Eng.* 9(9):559-561.
 1187 21. Snyder FF (1938) Synthetic unit-graphs. *Eos, Trans. Amer. Geophys. Union* 19(1):447-454.
 1188 22. Singh PK, Mishra SK, & Jain MK (2014) A review of the synthetic unit hydrograph: from the
 1189 empirical UH to advanced geomorphological methods. *Hydrolog. Sci. J.* 59(2):239-261.
 1190 23. Yang K, Smith LC, Chu VW, Gleason CJ, & Li M (2015) A Caution on the Use of Surface Digital
 1191 Elevation Models to Simulate Supraglacial Hydrology of the Greenland Ice Sheet. *IEEE J. Sel.*
 1192 *Topics Appl. Earth Observ. Remote Sens.* 8(11):5212-5224.

- 1193 24. Banwell AF, Arnold NS, Willis IC, Tedesco M, & Ahlstrøm AP (2012) Modeling supraglacial water
1194 routing and lake filling on the Greenland Ice Sheet. *J. Geophys. Res.* 117(F4):F04012.
- 1195 25. Linsley RK (1943) Application of the synthetic unit-graph in the western mountain states. *Eos,*
1196 *Trans. Amer. Geophys. Union* 24(2):580-587.
- 1197 26. Cordery I (1968) Synthetic unit hydrographs for small catchments in Eastern New South Wales.
1198 *Civil Engineering Transactions, Institution of Engineers (Australia)* 10:47-58.
- 1199 27. Wyatt FR & Sharp MJ (2015) Linking surface hydrology to flow regimes and patterns of velocity
1200 variability on Devon Ice Cap, Nunavut. *J. Glaciol.* 61(226):387.
- 1201 28. Andrews LC, *et al.* (2014) Direct observations of evolving subglacial drainage beneath the
1202 Greenland Ice Sheet. *Nature* 514(7520):80-83.
- 1203 29. van den Broeke M, *et al.* (2008) Partitioning of melt energy and meltwater fluxes in the ablation
1204 zone of the west Greenland ice sheet. *Cryosph.* 2(2):179-189.
- 1205 30. Christensen OB, *et al.* (2006) The HIRHAM5 Regional Climate Model. Version 5. in *Danish*
1206 *Meteorological Institute Technical Report.*
- 1207 31. Lucas-Picher P, *et al.* (2012) Very high resolution regional climate model simulations over
1208 Greenland: Identifying added value. *J. Geophys. Res. Atmos.* 117:D02108.
- 1209 32. Undén P, *et al.* (2002) HIRLAM-5 Scientific Documentation. Scientific Report.
- 1210 33. Undén P, *et al.* (2002) HIRLAM-5 Scientific Documentation. Technical Report.
- 1211 34. Roeckner E, *et al.* (2003) The atmospheric general circulation model ECHAM 5. PART I: Model
1212 description. (Max-Planck-Institut für Meteorologie (MPI-M)).
- 1213 35. Dee DP, *et al.* (2011) The ERA-Interim reanalysis: configuration and performance of the data
1214 assimilation system. *Q. J. R. Meteorol. Soc.* 137(656):553-597.
- 1215 36. Langen PL, *et al.* (2015) Quantifying Energy and Mass Fluxes Controlling Godthåbsfjord
1216 Freshwater Input in a 5-km Simulation (1991–2012). *J. Clim.* 28(9):3694-3713.
- 1217 37. Box JE, *et al.* (2012) Greenland ice sheet albedo feedback: thermodynamics and atmospheric
1218 drivers. *Cryosph.* 6(4):821-839.
- 1219 38. Vionnet V, *et al.* (2012) The detailed snowpack scheme Crocus and its implementation in SURFEX
1220 v7.2. *Geosci. Model Dev.* 5(3):773-791.
- 1221 39. Lefebvre F, Gallée H, van Ypersele J-P, & Greuell W (2003) Modeling of snow and ice melt at ETH
1222 Camp (West Greenland): A study of surface albedo. *J. Geophys. Res. Atmos.* 108(D8):4231.
- 1223 40. Zuo Z & Oerlemans J (1996) Modelling albedo and specific balance of the Greenland ice sheet:
1224 calculations for the Sendre Stromørd transect. *J. Glaciol.* 42(141):305-317.
- 1225 41. Fettweis X, Gallée H, Lefebvre F, & Ypersele J-P (2005) Greenland surface mass balance simulated
1226 by a regional climate model and comparison with satellite-derived data in 1990–1991. *Climate*
1227 *Dynamics* 24(6):623-640.
- 1228 42. Fettweis X, *et al.* (2013) Estimating the Greenland ice sheet surface mass balance contribution to
1229 future sea level rise using the regional atmospheric climate model MAR. *Cryosph.* 7(2):469-489.
- 1230 43. Ridder KD & Gallée H (1998) Land Surface–Induced Regional Climate Change in Southern Israel. *J.*
1231 *Appl. Meteorol.* 37(11):1470-1485.
- 1232 44. Gallée H & Schayes G (1994) Development of a three-dimensional meso- γ primitive equation
1233 model: katabatic winds simulation in the area of Terra Nova Bay, Antarctica. *Mon. Weather Rev.*
1234 122(4):671-685.
- 1235 45. Brun E, David P, Sudul M, & Brunot G (1992) A numerical model to simulate snow-cover
1236 stratigraphy for operational avalanche forecasting. *J. Glaciol.* 38(128):13-22.
- 1237 46. Gallée H, Guyomarc'h G, & Brun E (2001) Impact Of Snow Drift On The Antarctic Ice Sheet
1238 Surface Mass Balance: Possible Sensitivity To Snow-Surface Properties. *Bound.-Layer Meteor.*
1239 99(1):1-19.

- 1240 47. Fettweis X, *et al.* (2017) Reconstructions of the 1900–2015 Greenland ice sheet surface mass
1241 balance using the regional climate MAR model. *Cryosph.* 11(2):1015-1033.
- 1242 48. Bamber JL, Ekholm S, & Krabill WB (2001) A new, high-resolution digital elevation model of
1243 Greenland fully validated with airborne laser altimeter data. *J. Geophys. Res. Solid Earth*
1244 106(B4):6733-6745.
- 1245 49. Bamber JL, Layberry RL, & Gogineni SP (2001) A new ice thickness and bed data set for the
1246 Greenland ice sheet 1. Measurement, data reduction, and errors. *J. Geophys. Res. Atmos.*
1247 106(D24):33773-33780.
- 1248 50. Van Meijgaard E, *et al.* (2008) Technical Report: The KNMI regional atmospheric climate model
1249 RACMO version 2.1. (Royal Netherlands Meteorological Institute, De Bilt).
- 1250 51. Ettema J, van den Broeke MR, van Meijgaard E, & van de Berg WJ (2010) Climate of the
1251 Greenland ice sheet using a high-resolution climate model – Part 2: Near-surface climate and
1252 energy balance. *Cryosph.* 4(4):529-544.
- 1253 52. Kuipers Munneke P, *et al.* (2011) A new albedo parameterization for use in climate models over
1254 the Antarctic ice sheet. *J. Geophys. Res. Atmos.* 116:D05114.
- 1255 53. Kuipers Munneke P, *et al.* (2015) Elevation change of the Greenland Ice Sheet due to surface
1256 mass balance and firn processes, 1960-2014. *Cryosph.* 9(6):2009-2025.
- 1257 54. Lenaerts JTM, van den Broeke MR, van Angelen JH, van Meijgaard E, & Déry SJ (2012) Drifting
1258 snow climate of the Greenland ice sheet: a study with a regional climate model. *Cryosph.*
1259 6(4):891-899.
- 1260 55. Noël B, *et al.* (2016) A daily, 1-km resolution dataset of downscaled Greenland ice sheet surface
1261 mass balance (1958-2015). *Cryosph.* 2016:1-29.
- 1262 56. Van Wessem J, *et al.* (2014) Improved representation of East Antarctic surface mass balance in a
1263 regional atmospheric climate model. *J. Glaciol.* 60(222):761-770.
- 1264 57. Forster RR, *et al.* (2014) Extensive liquid meltwater storage in firn within the Greenland ice sheet.
1265 *Nature Geosci.* 7(2):95-98.
- 1266 58. Bosilovich MG, *et al.* (2016) MERRA-2. Initial evaluation of the climate. in *Technical Report Series*
1267 *on Global Modeling and Data Assimilation*, ed Koster RD (National Aeronautics and Space
1268 Administration, Greenbelt, Maryland).
- 1269 59. Rienecker MM, *et al.* (2011) MERRA: NASA's modern-era retrospective analysis for research and
1270 applications. *J. Clim.* 24(14):3624-3648.
- 1271 60. Lin S-J (2004) A “vertically Lagrangian” finite-volume dynamical core for global models. *Mon.*
1272 *Weather Rev.* 132(10):2293-2307.
- 1273 61. Molod A, Takacs L, Suarez M, & Bacmeister J (2015) Development of the GEOS-5 atmospheric
1274 general circulation model: evolution from MERRA to MERRA2. *Geosci. Model Dev.* 8(5):1339-
1275 1356.
- 1276 62. Takacs LL, Suárez MJ, & Todling R (2016) Maintaining atmospheric mass and water balance in
1277 reanalyses. *Q. J. R. Meteorol. Soc.* 142(697):1565-1573.
- 1278 63. Cullather RI, Nowicki SMJ, Zhao B, & Suarez MJ (2014) Evaluation of the Surface Representation
1279 of the Greenland Ice Sheet in a General Circulation Model. *J. Clim.* 27(13):4835-4856.
- 1280 64. Stieglitz M, Ducharne A, Koster R, & Suarez M (2001) The impact of detailed snow physics on the
1281 simulation of snow cover and subsurface thermodynamics at continental scales. *J.*
1282 *Hydrometeorol.* 2(3):228-242.
- 1283 65. Lynch-Stieglitz M (1994) The Development and Validation of a Simple Snow Model for the GISS
1284 GCM. *J. Clim.* 7(12):1842-1855.
- 1285 66. Greuell W & Konzelmann T (1994) Greenland ice margin experiment (GIMEx) Numerical
1286 modelling of the energy balance and the englacial temperature of the Greenland Ice Sheet.

- 1287 Calculations for the ETH-Camp location (West Greenland, 1155 m a.s.l.). *Glob. Planet. Change*
1288 9(1):91-114.
- 1289 67. Jordan R (1991) A one-dimensional temperature model for a snow cover: Technical
1290 documentation for SNTHERM.89. (U.S. Army Corps of Engineers, Cold Regions Research and
1291 Engineering Laboratory).
- 1292 68. Van As D (2011) Warming, glacier melt and surface energy budget from weather station
1293 observations in the Melville Bay region of northwest Greenland. *J. Glaciol.* 57(202):208-220.
- 1294 69. Smeets CJPP & van den Broeke MR (2008) Temporal and Spatial Variations of the Aerodynamic
1295 Roughness Length in the Ablation Zone of the Greenland Ice Sheet. *Bound.-Layer Meteor.*
1296 128(3):315-338.
- 1297 70. Snyder JP (1987) Map projections: A working manual. in *USGS Professional Paper* (Washington,
1298 D.C.).
- 1299 71. Pitcher LH, Smith LC, & Gleason CJ (2016) CryoSheds: a GIS modeling framework for delineating
1300 land-ice watersheds for the Greenland Ice Sheet. *Glsci. Remote Sens.* 53(6):707-722.
- 1301 72. Irvine-Fynn TDL, Hodson AJ, Moorman BJ, Vatne G, & Hubbard AL (2011) Polythermal glacier
1302 hydrology: a review. *Rev. Geophys.* 49(4):RG4002.
- 1303 73. Cook JM, Hodson AJ, & Irvine-Fynn TDL (2016) Supraglacial weathering crust dynamics inferred
1304 from cryoconite hole hydrology. *Hydrol. Process.* 30(3):433-446.
- 1305 74. Hoffman MJ, Fountain AG, & Liston GE (2014) Near-surface internal melting: a substantial mass
1306 loss on Antarctic Dry Valley glaciers. *J. Glaciol.* 60(220):361-374.
- 1307 75. Müller F & Keeler C (1969) Errors in Short-Term Ablation Measurements on Melting Ice Surfaces.
1308 *J. Glaciol.* 8(52):91-105.
- 1309 76. Karlstrom L, Zok A, & Manga M (2014) Near-surface permeability in a supraglacial drainage basin
1310 on the Llewellyn Glacier, Juneau Icefield, British Columbia. *Cryosph.* 8(2):537-546.
- 1311 77. Fountain AG & Walder JS (1998) Water flow through temperate glaciers. *Rev. Geophys.*
1312 36(3):299-328.
- 1313 78. Willis IC, Arnold NS, & Brock BW (2002) Effect of snowpack removal on energy balance, melt and
1314 runoff in a small supraglacial catchment. *Hydrol. Process.* 16(14):2721-2749.
- 1315 79. Van As D, *et al.* (2014) Increasing meltwater discharge from the Nuuk region of the Greenland
1316 ice sheet and implications for mass balance (1960–2012). *J. Glaciol.* 60(220):314-322.
- 1317 80. Fausto RS, *et al.* (2016) The implication of nonradiative energy fluxes dominating Greenland ice
1318 sheet exceptional ablation area surface melt in 2012. *Geophys. Res. Lett.* 43(6):2649-2658.
- 1319 81. Sasgen I, *et al.* (2012) Timing and origin of recent regional ice-mass loss in Greenland. *Earth*
1320 *Planet. Sci. Lett.* 333–334:293-303.
- 1321 82. Xu Z, Schrama EJO, van der Wal W, van den Broeke M, & Enderlin EM (2016) Improved GRACE
1322 regional mass balance estimates of the Greenland ice sheet cross-validated with the input–
1323 output method. *Cryosph.* 10(2):895-912.

1324